Energy Conversion and Management 349 (2026) 120805

Contents lists available at ScienceDirect

Energy Conversion and Management

journal homepage: www.elsevier.com/locate/enconman

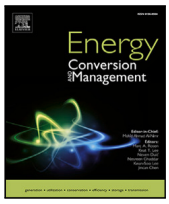

Investigation of synergies between solar energy and high-temperature heat pumps for process heat applications in Germany using nonlinear techno-economic optimization

Matthias Loevenich [a,c,*], Martin Bähr [b], Rushit Kansara [b], Jürgen Dersch [a], Robert Pitz-Paal [a,c]

[a] German Aerospace Center (DLR), Institute of Solar Research, Linder Höhe, Cologne, 51147, Germany
[b] German Aerospace Center (DLR), Institute of Low-Carbon Industrial Processes, Walther-Pauer-Straße 5, Cottbus, 03046, Germany
[c] RWTH Aachen University, Chair of Solar Technology, Linder Höhe, Cologne, 51147, Germany

ARTICLE INFO

Keywords:
Renewable process heat
Hybrid solar energy system
Concentrated solar technologies
High-temperature heat pump
Techno-economic optimization
Nonlinear design and operation optimization

ABSTRACT

The combination of solar energy and high-temperature heat pumps shows promising potential for supplying low to medium temperature process heat, even in countries with moderate available irradiation. To date, combinations of solar thermal collectors, high-temperature heat pumps, and thermal energy storage have been investigated for process heat applications. This study additionally considers hybridization with solar power from photovoltaics and battery energy storage, enabling the continuous supply of a representative process heat demand at 200 °C in Germany. To assess the synergies in various complex system configurations combining solar thermal, solar power, heat pump, and storage, a novel optimization algorithm is introduced. The optimization considers design and operational aspects by utilizing nonlinear component models to capture the complex dependencies between temperatures, mass flows, and power flows with the aim to minimize costs and emissions. Because the techno-economic optimization leads to a large-scale nonlinear multi-objective optimization problem that is computationally intensive, the algorithm applies different decomposition techniques while maintaining a high level of model detail. The results show that the investigated systems can reduce operating emissions by 48% on average while remaining cost-competitive with fossil burners. A configuration with parabolic trough collectors and heat pump in parallel, coupled with thermal energy storage in series and supported by photovoltaics, performs best at all three German sites investigated. Additionally, the results highlight the importance of nonlinear models for optimizing system design and operational strategies to identify non-obvious synergies.

1. Introduction

The European Union has committed to becoming climate-neutral by 2050 and is aiming for net-zero greenhouse gas emissions to ensure a sustainable future. This objective is central to the European Green Deal and legally binding under the European Climate Law [1]. Achieving this ambitious target requires the defossilization of industrial processes that contribute significantly to greenhouse gas emissions [2]. A crucial aspect of this transition is the decarbonization of the supply systems that provide these processes with energy [3]. Many industrial processes primarily require thermal energy, for example, 67% of the industrial energy demand in Germany is process heat, of which 72% is provided by fossil fuels [4].

Consequently, there is an urgent need to implement sustainable heating solutions for industrial processes. However, implementing sustainable heating solutions remains a major challenge. One challenge arises from the temperature levels required for these processes, which vary widely across industries [5]. Some examples are:

- Food Industry: mainly up to 200 °C
- Chemical Industry: mainly 200 – 1000 °C
- Metal Production: mainly over 1000 °C

Unlike heating solutions based on fossil fuels, renewable technologies must be selected based on the required temperature level. Another challenge is imposed by the volatile nature of renewable energy sources

* Corresponding author at: German Aerospace Center (DLR), Institute of Solar Research, Linder Höhe, Cologne, 51147, Germany.
E-mail addresses: matthias.loevenich@dlr.de (M. Loevenich), martin.baehr@dlr.de (M. Bähr), rushit.kansara@dlr.de (R. Kansara), juergen.dersch@dlr.de (J. Dersch), robert.pitz-paal@dlr.de (R. Pitz-Paal).

https://doi.org/10.1016/j.enconman.2025.120805
Received 23 July 2025; Received in revised form 7 November 2025; Accepted 20 November 2025
Available online 29 November 2025
0196-8904/© 2025 The Authors. Published by Elsevier Ltd. This is an open access article under the CC BY license (http://creativecommons.org/licenses/by/4.0/).

Nomenclature

Abbreviations

AC	Alternating Current
AOE	Annual operating emissions
BESS	Battery energy storage system
BP	Bypass
CAPEX	Capital expenditures
COP	Coefficient of performance
CRF	Capital recovery factor
DC	Direct Current
DLR	German Aerospace Center
DNI	Direct normal irradiance
DoD	Depth of discharge
DR	Dryer
DTI	Diffuse titled irradiance
EG	Electricity grid
FPC	Flat-plate collector field
GB	Gas Burner
GHI	Global horizontal irradiance
GTI	Global tilted irradiance
gwp	Specific global warming potential
HP	Heat pump
HTF	Heat transfer fluid
HX	Heat exchanger
IPOPT	Interior Point Optimizer
KPI	Key performance indicator
LCC	Life cycle cost
NSGA	Non-dominated sorting genetic algorithm
NTU	Number of transfer units
OPEX	Operational expenditures
PTC	Parabolic trough collector field
PV	Photovoltaics
REPEX	Replacement expenditures
SHS	Sustainable heating system
SOC	State of charge
STC	Solar thermal collector field
TAC	Total annualized cost
TES	Thermal energy storage
TMY	Typical meteorological year
TOY	Typical operational year
TOY	Typical operational year
TP	Thermal producers

Subscript

ac	Alternating Current
add	Additional
air	Air
amb	Ambient
ch	Charge
cold	Cold side
cur	Curtailment
d	Days
dc	Direct Current
dis	Discharge
es	Energy specific
fix	Fixed
gen	Generation
hot	Hot side
in	Inlet
ind	Indirect
inv	Investment
inver	Inverter
loss	Losses
max	Maximum
min	Minimum
mod	Module
nom	Nominal
oil	Thermal oil
op	Operation
out	Outlet
p	Periods
pop	Population
proj	Project
ps	Power specific
rec	Receiver
ref	Reference value
s	Starting points
th	Thermal
var	Variable

Latin Symbols

A	Area
C	Absolute costs
c	Relative costs
c_p	Specific heat capacity
d	Discount rate
E	Energy
f	Relative flow
$\boldsymbol{g}$	Inequality constraints
h	Hours
$\boldsymbol{h}$	Equality constraints
I	Irradiation
i, j, k	Counting variables
$\dot{m}$	Mass flow
m	Mass
N	Total number
n	Project year
P	Power flow
$\dot{Q}$	Heat flow
$\dot{q}\varepsilon$	Specific heat flow
R	Ratio
r	Proportional cost rate
s	Scaling exponent
T	Temperature
t	Time
U	Heat transfer coefficient
$\boldsymbol{x}$	Design decision variables
$\boldsymbol{y}$	Operational decision variables

Greek Symbols

α, β	Function coefficients
ΔT	Temperature difference
Δt	Time step size
ε	Effectiveness
η	Efficiency
θ	Incidence Angle

such as solar and wind, which usually do not match the process demand profile. Therefore, selecting appropriate components and designing a cost-competitive and low-carbon sustainable heating system is a complex task that depends on the process and site-specific conditions. In this study, we investigate sustainable heating solutions to provide low-carbon process heat for temperatures up to 200 °C in Germany. In addition to deep geothermal energy, the most promising technologies for this temperature range and geographical region are high-temperature heat pumps and solar thermal collectors [4].

High-temperature heat pumps are emerging as promising technologies for industrial decarbonization and energy efficiency [6]. They can generate heat of up to 250 °C using an available heat source and electricity [7]. However, heat pumps that can provide such high temperatures are still in the early stages of market launch, and are not yet commercially available. The heat pump performance mainly depends on the temperature lift from the source to the sink side; therefore, higher-quality heat sources, such as waste heat, are preferable to using the ambient environment. Techno-economic analyses reveal that high-temperature heat pumps can achieve payback periods of less than 1.5 years under favorable conditions, outperforming other technologies such as electric boilers [7]. Economic viability is influenced by factors such as electricity-to-gas price ratios, carbon taxes, and availability of heat sources [8]. High-temperature heat pumps combined with thermal energy storage can increase system flexibility and significantly reduce emissions [9]. However, challenges remain in optimizing the integration of heat pumps into existing industrial processes [10] and in reducing capital costs [11].

Solar thermal technologies offer significant potential for industrial process heating applications and provide environmentally friendly alternatives to fossil fuels [12]. Depending on the collector type, solar thermal collectors can generate heat at temperatures ranging from 50 to 100 °C for flat-plate collectors [12], 50 to 200 °C for evacuated tube collectors [12], 100 to 550 °C for parabolic trough collectors [13] and up to 1500 °C for solar towers [14]. Techno-economic analyses reveal that solar thermal collectors can be economically viable [15] and cost-competitive compared with fossil fuels [16] in high-irradiation regions. However, in regions with lower irradiation, such as Germany, solar thermal collectors can also contribute to the defossilization of process heat [17]. Nevertheless, widespread adoption faces challenges such as design complexities, limitations in land use, and economic factors such as collector costs [18]. In particular, the strong dependence on site-specific irradiation conditions and the technological differences of the collector types, which are applicable for different temperature levels, pose major challenges to system designers. Additionally, because of the intermittent nature of the available solar irradiation, thermal energy storage is crucial for ensuring high solar fractions [12]; however, the levelized cost of heat increases with the solar fraction owing to the time lag between the available solar radiation and process demand during the day, as well as the seasonality of the solar resource [18].

In [19] a comparative techno-economic analysis of high-temperature heat pumps and solar parabolic trough collectors using dynamic annual energy simulations to model energy performance is presented. For the analysis, three distinct industrial load profiles for steam at 140 °C were considered. The study shows that in high irradiation regions, such as Spain, parabolic trough systems are highly competitive, whereas in lower irradiation regions, such as Germany, heat pumps are often more cost-effective. Based on their findings, the authors propose a combination of solar thermal collectors with thermal storage and high-temperature heat pumps, with a solar collector field sized to economic parity in levelized cost compared to the heat pump system, and the heat pump sized to meet the rest of the demand.

For the building sector, the hybridization of solar producers, storage, and heat pumps has been investigated in several studies (e.g. [20, 21]). For the industrial sector targeted in this study, literature also reveals that hybrid systems consisting of solar thermal collectors, thermal storage and heat pump can economically substitute conventional fossil burners for low to medium temperature process heat demands. The following paragraphs provide an overview of recent studies on solar thermal and heat pump hybrids for industrial heat demand.

[22] presents a method to enhance the efficiency and cost-effectiveness of solar thermal facilities for industrial batch processes by integrating a heat pump. The research focuses on a case study of a batch process for milk pasteurization in Mexico, providing heat at 100 °C. The configuration is fixed, using low temperature solar collectors as a heat source for the heat pump and an integrated storage tank that is charged using higher temperature heat from the heat pump and discharged to increase the solar field outlet and therefore heat pump evaporator inlet temperature. This approach significantly lowers the capital cost associated with the storage system, using the heat pump as a core component for system downsizing. The study concludes that the system is not only technically feasible but also economically competitive compared to natural gas costs.

In [23] the authors propose a design methodology for heat pumps assisted by solar thermal collectors and thermal storage to supply heat and electric power for industrial applications, specifically focusing on a second-generation bioethanol production case study in Mexico. For both, heat supply and power production using an organic Rankine cycle, the maximum supply temperature is set to 100 °C. The configurations are fixed with solar thermal collectors and storage supplying the source sides of the heat pumps. The system design is evaluated using lower-than-winter irradiance levels for the solar thermal collector fields and nominal design points for the other components. Using this conservative approach, the study shows that adding heat pumps to a solar thermal supply solution can significantly reduce costs and land use and that a year-round operation can be guaranteed with energy costs comparable to those of fossil fuel based supply solutions.

In [24] a comprehensive performance and economic analysis of a novel system combining solar thermal collectors, a storage tank and a high-temperature heat pump to supply a typical industrial steam demand at 120 °C in South Korea is presented. The methodology involves designing the system using annual performance simulations in Simulink and varying solar thermal collector area and storage tank volume to identify an optimal design. The configuration of solar thermal collectors, storage tank and heat pump is fixed, with the solar thermal collectors used as heat source for the heat pump. The results indicate that the proposed system is a technically and economically viable alternative to conventional LPG boilers and that the STC area has a more significant impact on both performance and economic feasibility than the ST volume. An interesting insight from the analysis is the non-linear relationship between system size and economic viability. While larger systems offer better performance and higher carbon reductions, the economic benefits do not scale proportionally.

[25] proposes standardized integration concepts for combining solar thermal and heat pump systems in industrial applications for demand temperatures up to 125 °C. The concepts include a parallel configuration of solar collectors and heat pump as well as three serial integration concepts with varying order and storage concept. Instead of comparing the different integration concepts, the paper introduces a tool enabling users to apply the different integration concepts to specific use cases and identify optimal solutions.

Finally, [26] presents a simulation-based development of globally applicable design guidelines for hybrid solar thermal and heat pump systems with thermal storage in industrial applications. The primary objective is to provide transferable findings on optimal system design to maximize greenhouse gas, energy, and cost savings. The research compares three different hydraulic concepts of solar collectors and heat pump, one parallel and two serial, across a wide range of applications and economic frameworks, totaling 30,240 parameter combinations. Key parameters varied include location, heat sink temperatures, heat source temperatures, load profiles, and economic factors, such as energy prices and interest rates. The analysis highlights that at the energy price levels of early 2022, the investigated systems become economically competitive with natural gas boilers for many applications up to 150 °C. Technical findings also reveal that the choice of hydraulic concept (parallel vs. serial) has a limited impact on system performance compared to the available heat source temperature when the goal is to achieve a renewable fraction near 100%.

In this study we investigate the synergies of a hybrid system with solar collectors, thermal energy storage and high-temperature heat pump for a representative use case with available waste heat at 80 °C

and a demand temperature of 200 °C in Germany. Therefore, we increase the demand temperature compared to recent studies, where a maximum temperature of 150 °C is considered. Furthermore, [26] has already shown that different system configurations can influence the performance of such a sustainable heating system, but also that other parameters, such as heat source temperatures, can have a more significant impact when aiming at a renewable fraction near 100%. We investigate higher temperature levels and have fixed heat source parameters given by the use case considered in this study. Additionally, we investigate the system costs depending on the operating emissions and also allowing renewable fractions lower than 100%. Therefore, the configuration can have a significant impact on costs and emissions and we compare various system configurations with both concentrated and non-concentrated solar thermal collectors and vary the parallel and serial connections of solar thermal collectors, heat pump and thermal energy storage. Moreover, because our study focuses on Germany where the available solar radiation is limited, we consider further solar hybridization options. As shown in [21] for an application from the building sector and in [27] also for the industrial sector, heat pumps can additionally benefit from a combination with low-cost photovoltaic power compared to electricity drawn from the grid. Therefore, we add on-site photovoltaics and battery energy storage to the sustainable heating system as a possible low-cost, low-carbon and flexible power source for the heat pump in addition to the electric grid connection. Finally, the techno-economic performance of hybrid sustainable heating systems with solar thermal collectors and high-temperature heat pumps strongly depends on the operation and design of the system. Therefore, many studies focus on developing standardized operating strategies and design methods [22,25,26]. We increase the system complexity by adding photovoltaics and battery energy storage to the sustainable heating system. To address the complexity of designing and operating a system that contains two intermittent solar producers that provide heat and electricity, power-to-heat conversion possibilities, and different types of storage, we apply optimization techniques to determine optimal system designs and operating strategies. This enables us to find both low-cost and low-emission solutions as well as trade-offs in terms of system design. We present an optimization algorithm that can solve the nonlinear coupled optimization problem of design and operation for a certain system configuration at a given site. The algorithm uses different decomposition techniques to reduce computational effort while maintaining a high level of detail in the component models.

In summary, this work relies on existing studies to investigate the synergies of solar energy and high-temperature heat pumps to provide low-carbon process heat in Germany. It differs from the existing studies in three key aspects:

1. The sustainable heating system supplies the process heat demand at a higher temperature level of 200 °C.
2. We investigate more complex hybridization options for systems with solar thermal collectors, high temperature heat pump and thermal energy storage by adding on-site photovoltaics and battery energy storage.
3. A novel optimization algorithm handling mass flow based nonlinear component models is presented and applied to determine optimal designs and operating strategies depending on the configuration and site-specific conditions.

The remainder of this paper is organized as follows. In Section 2, we present a representative use case, design different configurations by interconnecting the system components, and define meteorological data and market conditions for three representative sites in Germany. Furthermore, we define the techno-economic optimization problem and introduce a solution algorithm. In Section 3, we present the results of the techno-economic optimization for each configuration at each site. Section 4 focuses on interpreting the results and discussing the resulting synergies between the components. We conclude the study by summarizing the key findings and outlining aspects of further investigation in Section 5.

2. Materials and methods

To investigate the coupling effects between solar energy and high-temperature heat pumps, we assess and compare the techno-economic performance of six sustainable heating systems (SHS) that include photovoltaics, battery energy storage and an electricity grid connection combined with solar thermal collectors, high-temperature heat pump and thermal energy storage in different parallel and serial configurations. For the investigation, we firstly identify a representative use case in Section 2.1, which specifies the heat demand profile that the SHS need to cover. Next, we define key performance indicators in Section 2.2 to describe and compare the techno-economic performance of different SHS configurations for the investigated use case. In Section 2.3, SHS components and modeling approaches are introduced. Subsequently, we design six SHS configurations by connecting the components in different ways, as explained in Section 2.4. To incorporate the effects of site-specific meteorological conditions into the investigation, we consider three representative sites in Germany, introduced in Section 2.5. For each configuration at each site, optimization techniques are used to determine the designs and corresponding operating strategies that minimize the KPIs. The optimization problem and the solution algorithm are explained in Section 2.6. Based on the optimization results, we are then able to compare the different configurations and investigate their performance under different ambient conditions.

2.1. Use case

The use case considered in this study is a food industry application. This industrial site produces milk concentrate, milk powder, cheese, and butter. We focus on the powder plant in which a spray dryer (DR) is used to remove moisture from milk concentrate. The process parameters are documented in [28]. In the existing drying process, the incoming ambient air is first heated by a steam boiler and then by an oil burner to reach 200 °C before it enters the DR, whereas the DR exhaust air at 80 °C is dissipated into the ambient environment. In this study, the existing fossil-based heating system is replaced by an SHS. The SHS uses a thermal oil cycle to supply heat to the incoming ambient air via an oil-to-air heat exchanger (HX), which is then sent to the DR. The resulting use case including SHS, HX and DR is shown in Fig. 1. According to [28], a constant DR heat demand of approximately 1.84 MW is assumed, which must be covered over the entire year such that the annual DR heat demand is 16 100 MWh. On this basis, the SHS oil cycle heats up an incoming ambient air flow of 14.85 kg/s to 200 °C to cover the continuous heat demand of the DR, while a return air flow of 14.85 kg/s at 80 °C is available as heat source.

2.2. Key performance indicators

To evaluate the techno-economic performance of an SHS configuration, various key performance indicators (KPI), such as costs and emissions, can be used. In the techno-economic assessment of an SHS configuration, the degrees of freedom are the design, which describes the component capacities, and the operating strategy, which describes the heat and power flows between the components at each time point. The question now arises as to which combination of design and operating strategy leads to the most economical configuration, and thus to the lowest system costs, including investment and operational expenses. Therefore, we define the total annualized cost (TAC) as the first KPI. However, cost-optimal SHS solutions do not guarantee low-carbon operations, which is often contrary to system costs. Accordingly, the annual operating emissions (AOE) are defined as the second KPI.

For the TAC, we consider capital costs and fixed operational expenditures for all SHS components and the heat exchanger. Additionally, we include variable operating costs arising from grid power consumption. For the AOE we only consider emissions arising from grid power consumption. It should be noted that we use a typical operational year

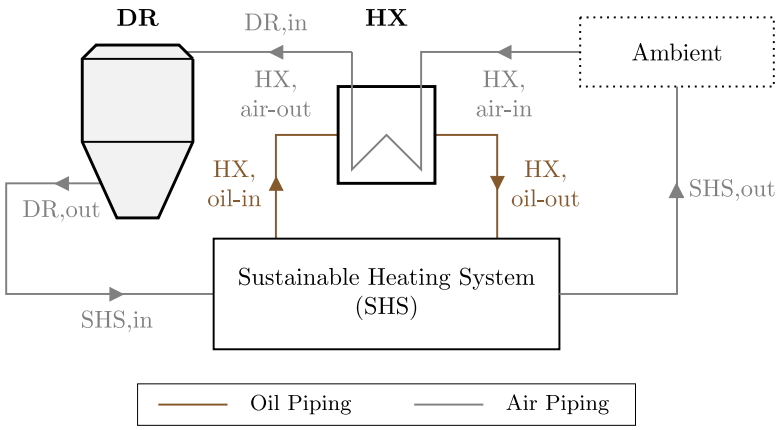

Fig. 1. Schematic representation of the implementation of the sustainable heating system (SHS) and heat exchanger (HX) into the considered use case to supply the dryer (DR) with hot air.

(TOY) for the techno-economic assessment and assume that the SHS perform in accordance with the TOY for each year of their operational life. Therefore, the annual operational expenditures and annual operating emissions are assumed to be identical in each year of the SHS lifetime of 25 years, in accordance with the TOY. Detailed definitions of the KPIs are provided in Appendix A.1.

2.3. Components

We use the following components to build SHS configurations combining solar energy, heat pump and storage:

- photovoltaic field (PV)
- battery energy storage system (BESS)
- electricity grid (EG)
- solar thermal collector field (STC)
- high-temperature heat pump (HP)
- thermal energy storage (TES)

To evaluate the KPIs introduced in Section 2.2, component costs and annual operational performance need to be evaluated depending on the SHS configuration and design. All SHS configurations consist of the same SHS components (PV, BESS, EG, STC, HP and TES), where the electric components (PV, BESS and EG) are always connected identically and used to power the HP, and the thermal producers (STC and HP) are connected in parallel or series with the TES. Additionally, we compare two different STC types, where non-concentrating collectors are only investigated in series and concentrating collectors in parallel or in series with the HP, resulting in a total of six configurations (see Section 2.4). The component models can be defined independently of the specific SHS configuration, since the configurations only differ in the connection of the components. Nevertheless, the component performance always depends on the current design, which represents the capacities of all components independent of the connection. Therefore, for each component, both costs and operational performance are defined depending on component specific capacity variables.

Based on these capacity variables, investment and fixed operating costs can be described as follows. The investment costs are defined using exponential cost curves to represent economy of scale, and fixed annual operating costs are evaluated as a percentage of the investment costs, as proposed in [29]. The equations and parameters used to define the component specific investment and fixed operating costs are presented in Appendix A.2. All investment costs are, if necessary, converted to euros using the conversion rate of the cost reference year and then projected to the year 2023 using CEPCI [30]. Notably, we add a surcharge of 30% on the investment costs of the thermal components (STC, HP, TES, and HX) for indirect costs that are not included in the cost functions and a replacement of the BESS every 10 years.

To describe the operational performance of the components, we introduce scalable performance models for each component, again depending on the component specific capacity variables. As stated in Section 2.2, we use a TOY to evaluate the operational variables for the KPIs. Specifically, we consider a discrete setting with hourly time steps, which means that the year is discretized hourly. In other words, the TOY originally represented as a continuous time axis is replaced by a discrete domain by $N_t + 1$ uniformly spaced discrete time points t_i with an hourly time-step size $\Delta t := t_i - t_{i-1}$. Consequently, continuous-time functions are considered only at these points at time t_i for $i = 1, \dots, N_t$. Based on this assumption the component performance is evaluated using a quasi-static mass flow based modeling approach. This means that for each component, conservation laws in the form of energy and mass balances are applied to relate the inlet and outlet energy flows to the change in energy available within the component. Techno-economic optimization of comparable SHS is usually performed using highly simplified energy based performance models considering heat and power flows at fixed temperature levels (e.g. [31–33]). In this study, we introduce higher-detail optimization models to define the energy balances using thermal energy and heat flows described by mass flows, specific heat capacities and continuous temperatures, as well as electric energy and power flows. Depending on the component, the energy and mass balances are supported by empirical equations to describe certain efficiencies or temperature relations, but the conservation laws are always fulfilled. Therefore, inlet and outlet mass flows, temperatures and power flows of all SHS components (PV, BESS, STC, HP, TES) and the HX are evaluated in each discrete time point. For the storage components (BESS, TES), the energy state is also updated in each discrete time point. Using a quasi-static modeling approach, we assume stationary processes for the other components (PV, BESS, STC, HP, HX), neglecting transient effects such as start up, shut down or load variation ramps, and thermal inertia. Therefore, the change in energy state is always set to zero in the energy balances for these components and no additional ramp constraints are considered. These simplifications are common in techno-economic optimization (e.g. [31–33]), but also critically reviewed for the methodology and SHS investigated in this study. Furthermore, pressure losses and corresponding auxiliary power demands are assumed to be small compared to HP power consumption and therefore neglected in this study. The detailed equations used to describe the operational performance of the components are presented in Appendix A.2. A full set of parameter values is provided in Appendix B. In the following paragraphs the components and their capacity variables are briefly introduced.

The PV system serves as a renewable power source for the HP in all SHS configurations. It consists of south-facing Si-mono-type PV modules [34] with a fixed tilt angle of 32 ° that are connected in arrays and

strings, and a set of DC-AC inverters that provide AC power for the HP. We use the total module area A_{PV} to define the PV capacity. Based on the module area, we can also calculate the nominal DC power $P_{PV,dc\text{-}nom}$ for cost calculations and comparison with other component capacities. The maximum AC power $P_{PV,ac\text{-}nom}$ that functions as an upper bound for the PV power production is also defined depending on $P_{PV,dc\text{-}nom}$ and therefore A_{PV} using a fixed DC-AC ratio of 1.3 [35]. The operational performance is modeled using a three-parameter model to describe the module efficiency [36] and a constant inverter efficiency [37].

To store excess PV power or utilize low-price periods of the EG, the SHS contain a BESS in form of lithium-ion storage with integrated inverters. BESS costs are defined depending on the nominal energy capacity $E_{BESS,nom}$ and the nominal power capacity $P_{BESS,nom}$. The performance also depends on these values, which function as boundaries for energy content and charge and discharge power flows. Therefore, both variables are used to describe the BESS capacities. The BESS is modeled using an energy balance considering a constant round trip efficiency of 86% and a maximum depth of discharge of 80% [38].

To guarantee a year-round supply of the DR heat demand, the SHS additionally include a connection to the EG. The EG capacity is defined by $P_{EG,max}$ and limits the power that can be drawn from the grid. We neglect investment costs for the EG but apply an annual fixed operating cost depending on $P_{EG,max}$ in addition to the variable operating costs arising from power consumption.

In addition to the solar power production via PV, the SHS also contain an STC field that heats thermal oil in the SHS oil-cycle. The solar thermal conversion efficiency strongly depends on the temperature inside the solar field and the type of collector used. For this purpose, we include two different collector types into our investigation:

- flat-plate collectors (FPC) south-facing with a fixed tilt angle of 32° and
- parabolic trough collectors (PTC) oriented north–south with one axis tracking in east–west direction.

While FPCs utilize direct and diffuse irradiation to heat a fluid inside the receivers, PTCs concentrate direct irradiation onto the receiver to increase the flux density and available outlet temperature. Therefore, for FPCs we assume a maximum outlet temperature of 230 °C [39] while for PTCs we assume a maximum outlet temperature of 400 °C [40]. The component costs and operational performance of both collector types are defined depending on the collector area A_{STC}, which is therefore used as the STC capacity variable. Additionally, we introduce a nominal heat output $\dot{Q}_{STC,nom}$ at nominal operating and ambient conditions for the comparison with other component capacities. The operational performance, including temperature-dependent heat losses, is calculated following [29].

The HP is used to convert power from PV, BESS and EG into heat. We consider a HP based on the reverse Brayton cycle, that supplies heat up to 250 °C on the sink side [41]. The HP uses a compressible fluid, such as air, as the working medium and mainly consists of four components [42]: a low-temperature heat exchanger, compressor, high-temperature heat exchanger, and turbine. The working fluid is heated by the heat source via the low-temperature heat exchanger and its temperature is increased at constant pressure. The heated working fluid is then isentropically compressed to increase the pressure and, in turn, the temperature. It then passes through the high-temperature heat exchanger and transfers heat to the sink, reducing the temperature again at constant pressure. Finally, the turbine expands the working fluid at constant entropy to lower the temperature and complete the cycle. For the investigated SHS, the HP uses waste heat in form of an air flow on the source side and inputs heat into the thermal oil-cycle of the SHS on the sink side. HP costs are defined depending on the nominal heat output on the sink side $\dot{Q}_{HP,nom}$, which also functions as an upper bound in the operational performance evaluation. Therefore $\dot{Q}_{HP,nom}$ is used to define the HP capacity. We use a model based on the Carnot efficiency to describe the operational performance of the HP [43].

Several TES technologies are available in the present temperature range [44]. Owing to the high specific heat capacity, easy availability of the technology, and lower investment costs, we use a concrete-based sensible TES that is flown through by thermal oil from the SHS oil-cycle. The TES costs and operational performance are defined depending on the storage material mass m_{TES}, functioning as the TES capacity variable. The available temperature range (160–360 °C) and material properties are set according to [45]. The TES performance is modeled using a lumped capacitance approach following [42].

Finally, the HX is used to heat ambient air to then supply the DR demand using heat provided by the oil-cycle of the SHS. In contrast to the other components, the HX has a fixed design for all configurations and is therefore not listed in the SHS components but introduced alongside the use case. Nevertheless, it is included in the cost evaluations and performance calculations. It is designed using a nominal coarseness of 20 °C and a nominal heat flow matching the DR heat demand. The corresponding costs and operational performance are evaluated based on the resulting heat transfer area A_{HX} using the effectiveness-NTU method [46].

2.4. Configurations

Based on the components introduced in Section 2.3, we define different SHS configurations that utilize solar energy, power-to-heat technology, and storage to supply the heat demand described in Section 2.1. The investigated SHS configurations are defined by the different interconnections of the components. Each SHS configuration includes PV, BESS, STC, HP, TES, EG and additionally HX and DR from the use case to consider all relevant interfaces to the ambient environment. To describe the interconnection of the SHS components, each configuration can be divided into the air cycle (gray lines), oil cycle (brown lines), and electric supply (black lines).

The air cycle is identical for each SHS configuration and takes ambient air, which is then heated in the HX by the oil cycle. The heated air enters the DR and is cooled by a constantly working drying process. When the HP is in operation, the DR return flow is routed to the HP cold side as source heat before returning to the ambient environment. In contrast, when the HP is not in operation, the DR return flow is routed directly to the ambient environment.

The electric supply is identical for each SHS configuration and consists of EG, PV, and BESS. It is used to power the HP compressor, whereas all additional electric auxiliary units, such as fans and pumps in the air and oil cycle, are neglected here. The power drawn from the EG can be used to supply the HP with electricity and charge the BESS in low-price periods. The available PV power can also be used to supply the HP directly or charge the BESS. Finally, the HP can be supplied by BESS discharge. We only allow drawing electricity from the EG, so it is not possible to feed in excess PV power or use the BESS to gain revenue from electricity price fluctuations.

The oil cycle consists of STC, HP, TES, and HX. STC and HP together are also referred to as thermal producers (TP). The oil cycle is used to supply the HX with sufficient heat to cover the heat demand defined by the DR and ambient conditions. STC can produce solar heat when the sun is shining. The HP hot side can provide heat to the oil cycle at any time by taking excess DR heat on the cold side and pumping it to a higher temperature level using electricity from the electric supply. The available heat can then be used either to charge the TES or directly supply the HX. Therefore, the HX is supplied by a combination of STC and HP heat, as well as TES discharge. Additionally, a bypass (BP) can be used to regulate the HX inlet temperature by mixing the flows of STC, HP, and TES with the HX outlet flow.

While these general definitions apply to all SHS configurations, we investigate different parallel and serial interconnections of STC, which can be either non-concentrating FPC or concentrating PTC, and HP to

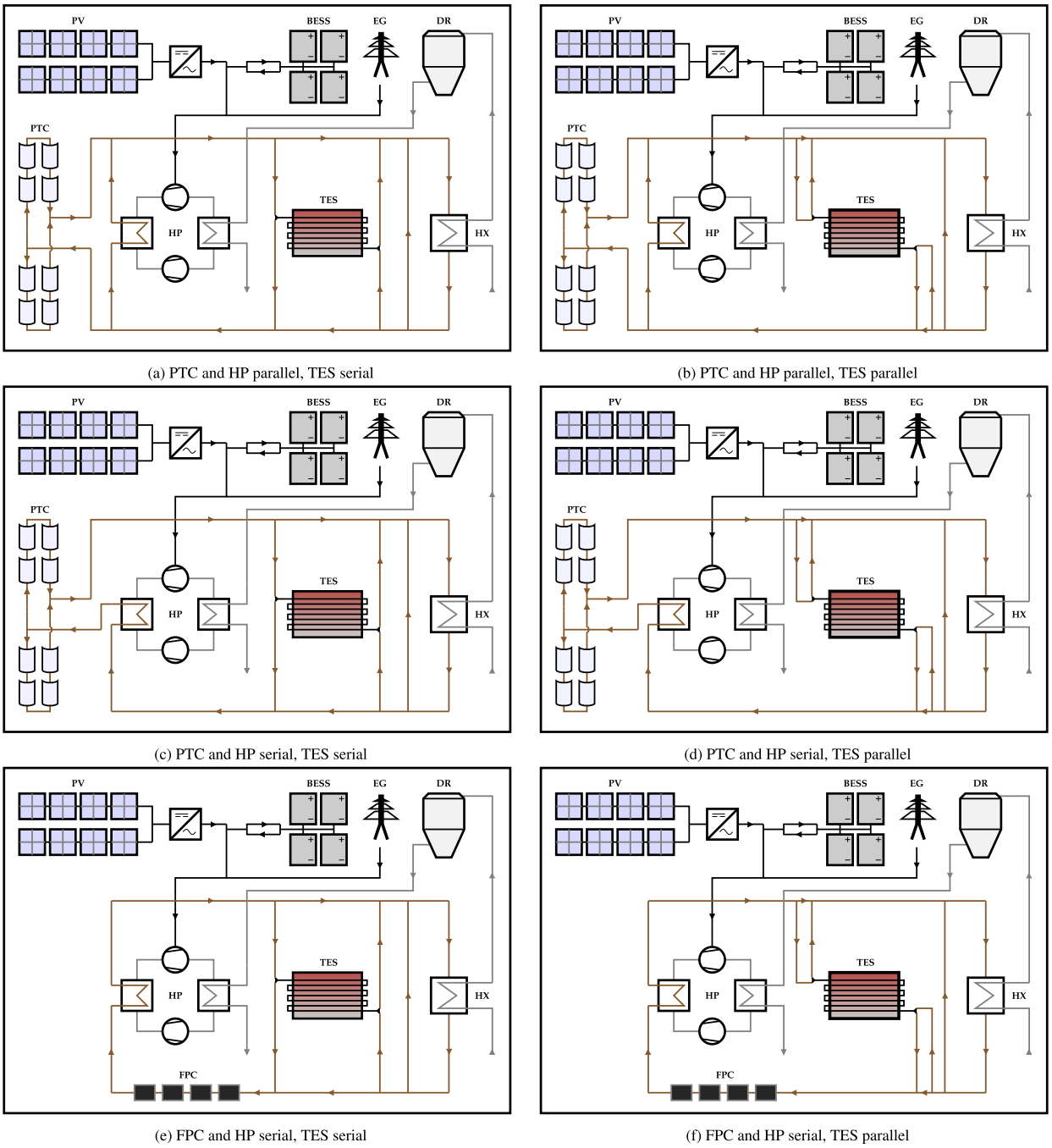

(a) PTC and HP parallel, TES serial

(b) PTC and HP parallel, TES parallel

(c) PTC and HP serial, TES serial

(d) PTC and HP serial, TES parallel

(e) FPC and HP serial, TES serial

(f) FPC and HP serial, TES parallel

Fig. 2. Investigated SHS configurations including photovoltaics (PV), battery energy storage (BESS), electricity grid (EG), parabolic trough collectors (PTC), high-temperature heat pump (HP), thermal energy storage (TES) and heat exchanger (HX) to supply the dryer (DR).

elaborate which SHS configuration benefits hybridization the most for the given use case. Additionally, the TES is also embedded in series and parallel for each different interconnection of STC and HP, resulting in six different configurations (a)–(f) shown in Fig. 2. From top to bottom, the interconnection of the STC and HP changes; from left to right, either a serial or parallel TES connection is considered.

In configurations (a) and (b), the STC and HP hot sides are connected in parallel. This enables both components to operate with independent mass flows and outlet temperatures. The outlet flows of both components are mixed to a TP hot flow before being routed to the TES or HX. Because non-concentrating FPC cannot provide an outlet temperature high enough to supply the HX demand alone, we only use concentrating PTC for the parallel connection of the TPs. Configurations (a) and (b) differ in the connection of TES. In configuration (a), the TES charge outlet flow is mixed with the remaining TP hot flow. The discharge outlet flow is mixed with the TP cold flow, which is then split and routed to the STC and HP. Therefore, the TES is connected serially to the TPs to allow the preheating of the HX outlet flow before entering HP and PTC. This TES connection is typical for systems with HP and TES because the HP performance benefits from high inlet temperatures and, therefore, preheating with TES discharge. For systems with STC and TES, a parallel TES connection is usually chosen to enable TES discharge without simultaneous operation of STC, which always depends on the available irradiation. To investigate the performance of a parallel TES for a system with a combination of STC and HP, we integrated it into configuration (b). This means that the TP hot flow is used for the

TES charge and then mixed with the HX outlet flow on the cold side of the oil cycle. For the TES discharge, the HX outlet flow is heated and directly mixed with the TP hot flow on the hot side of the oil cycle before reentering the HX. Configurations (c) and (d) study the HP and concentrating PTC connected in series, whereby in (c) TES is connected in series and in (d) TES is connected in parallel. A serial connection of STC and HP leads to lower temperature differences over the single TPs, which can benefit HP performance. We decided to place HP first and PTC second in the flow direction in these configurations because the maximum HP outlet temperature is lower than that for PTC. This means that all TP cold side flows coming from HX and TES are routed to the HP first, the HP outlet flow is directly routed to the PTC inlet, and the PTC outlet flow is identical to the TP hot flow, which is then routed back to TES and HX. In configurations (e) and (f), non-concentrating FPC and HP are investigated connected in series, where again (e) has TES connected in series, and (f) has TES connected in parallel. In this case, FPC has a lower maximum outlet temperature than HP, so FPC comes first in the direction of the oil flow, and HP comes second. As a result, the entire TP cold-side flow coming from HX and TES is routed to FPC, the FPC outlet flow is directly routed to the HP inlet, and the HP outlet flow is identical to the TP hot flow that is directed back to TES and HX. It should be noted that PTC and FPC can function as bypasses for themselves in all configurations, which is specifically relevant for the configurations with STC and HP in series. In times where no solar irradiation is available, the curtailment factor can be set to one, such that STC thermal losses are not incurred, as if the collector field would be bypassed.

To determine the operational behavior of the SHS configurations, in addition to the standalone component models, further system variables and constraints are required, which describe the interconnections and interactions of the components. These constraints are formulated based on steady-state energy and mass balances. Appendix A.3 introduces the additional constraints used to connect the components for configuration (a). The same procedure is carried out for the other configurations (b)–(f) in order to form the overall models for system operation required to evaluate the techno-economic performance. In this way the EG power consumption in each time point is described using the scalable component models and configuration specific additional constraints, and the variable operating costs and operating emissions can be evaluated depending on the SHS configuration and design.

Finally, to compare the SHS configurations with a fossil burner system, we additionally calculate the costs and emissions of a gas burner (GB) that heats thermal oil to supply the HX instead of the SHS. The assumptions and modeling equations used to evaluate TAC and AOE for the GB are given in Appendix A.4.

2.5. Meteorological data and market conditions

The SHS configurations defined in Section 2.4 are analyzed at different sites in Germany to elaborate on the differences in their performance depending on site-specific conditions. Obviously, there is only one price zone for the electricity market in Germany; therefore, the EG price and global warming impact values do not differ depending on the site. However, the ambient conditions at these locations change significantly. Because the SHS use solar energy to produce heat and electricity, we investigate three sites that are representative of low (Hamburg), medium (Würzburg), and high (Munich) irradiation conditions in Germany. The key aspects describing the three sites are summarized in Table 1.

We perform a techno-economic assessment based on a TOY with hourly time resolution; therefore, we use typical meteorological years (TMY) to define the meteorological conditions. The TMY data are generated with the Photovoltaic Geographical Information System [47]. For electricity market prices and emission factors, data from Agorameter [48] are used. In our study, market data from 2023 are applied as a representative data set. Fig. 3 shows the annual duration curves of irradiation and ambient temperature for the three sites investigated (top) as well as the annual duration curves of global warming potential and electricity prices (bottom). The differences between the three representative sites are clearly visible in the irradiation curves, whereas the ambient temperature only shows site-specific variations at the lower end. These differences influence the component efficiencies as well as the heat demand at the HX, where the ambient air is heated to supply DR demand. The global warming potential indicates a rather linear behavior, while the electricity prices show a dominant range between 60–120 €/MWh for more than 4800 h, but also extreme values of over 200 €/MWh at the upper end and negative prices under -45 €/MWh at the lower end, which only occur for a few hours per year. It should be noted that the annual duration curves do not show differences in the hourly dynamics, which also influence the operational behavior of the SHS. These influences are presented and discussed in Sections 3 and 4.

2.6. Optimization problem and solution algorithm

As mentioned above, the aim of this study is to evaluate the techno-economic performance of each SHS configuration based on TAC and AOE for the considered use case. However, a design with the lowest TAC does not necessarily have the lowest AOE, and vice versa, resulting in a Pareto front that reflects a trade-off between system costs and environmental impact. To adequately solve this problem, that is, to find Pareto-optimal SHS designs with minimal TAC and AOE, an optimization approach is used. We first describe the optimization problem in Section 2.6.1 and then present how it is solved using the proposed solution algorithm in Section 2.6.2.

2.6.1. Optimization problem

The techno-economic optimization of the SHS can be formulated as a multi-objective optimization problem, enabling a holistic approach that optimizes both TAC and AOE simultaneously, given by

$$\begin{aligned} \min_{\boldsymbol{x},\boldsymbol{y}(t_1),\dots,\boldsymbol{y}(t_{N_\mathrm{t}})} \quad & \Big[\, TAC\left(\boldsymbol{x}, P_\mathrm{EG}(t_1), \dots, P_\mathrm{EG}(t_{N_\mathrm{t}})\right), \\ & AOE\left(P_\mathrm{EG}(t_1), \dots, P_\mathrm{EG}(t_{N_\mathrm{t}})\right) \Big] \\ \text{s.t.} \quad & \boldsymbol{h}\left(\boldsymbol{x}, \boldsymbol{y}(t_1), \dots, \boldsymbol{y}(t_{N_\mathrm{t}})\right) = \boldsymbol{0}, \\ & \boldsymbol{g}\left(\boldsymbol{x}, \boldsymbol{y}(t_1), \dots, \boldsymbol{y}(t_{N_\mathrm{t}})\right) \leq \boldsymbol{0}, \end{aligned} \tag{1}$$

where $\boldsymbol{x} = [x_1, \dots, x_7] = [P_\mathrm{EG,nom}, A_\mathrm{PV}, E_\mathrm{BESS,nom}, P_\mathrm{BESS,nom}, \dot{Q}_\mathrm{HP,nom}, A_\mathrm{STC}, m_\mathrm{TES}]$ is a vector of time-independent continuous design variables representing the capacity of each component, $P_\mathrm{EG}(t_i)$ is the time dependent power drawn from the EG and $\boldsymbol{y}(t_i)$ is a vector of time-dependent continuous operational variables defined at hours t_i for $i = 1, \dots, N_\mathrm{t}$. Note that AOE depends only indirectly on the design variables $\boldsymbol{x}$. For example, a direct influence would be associated with the emissions caused during the manufacture of the components, which were not considered in this study. Moreover, only the electric power $P_\mathrm{EG}(t_i)$ drawn from the grid has a direct influence on AOE and TAC. Nevertheless, there is an indirect influence of the remaining $\boldsymbol{y}(t_i)$ and $\boldsymbol{x}$ on both objectives, as the component capacities and the operating strategy always influence each other. In other words, the equality and inequality constraints ($\boldsymbol{h}$ and $\boldsymbol{g}$) that affect the operating strategy determining variables such as energy flows, mass flows, and temperatures at any time point, include both design variables and operational variables. Additionally, the set of constraints always depends on the configuration. Certain constraints, in particular (A.10), (A.13)–(A.16), (A.24)–(A.26), (A.29)–(A.33), (A.36)–(A.39), and (A.44)–(A.47) described in Appendix A.2, must be fulfilled for all SHS configurations. Depending on the interconnection of the specific configurations (a)–(f), further constraints must be maintained; for example, the constraints (A.50)–(A.68) described in Appendix A.3 for configuration (a).

Considering the objective functions, the TAC is nonlinear owing to the nonlinear equipment cost functions, whereas the AOE is linear.

Table 1
Coordinates, annual irradiation sums and mean ambient temperature for the investigated sites with low (Hamburg), medium (Würzburg) and high (Munich) irradiation.

Site	Coordinates	Direct normal irradiation MWh/a	Global horizontal irradiation MWh/a	Mean ambient temperature °C
Hamburg	53.53 N, 10.21 E	963.52	1036.67	10.9
Würzburg	49.79 N, 9.93 E	1154.30	1191.54	9.99
Munich	48.31 N, 11.88 E	1301.77	1257.15	10.33

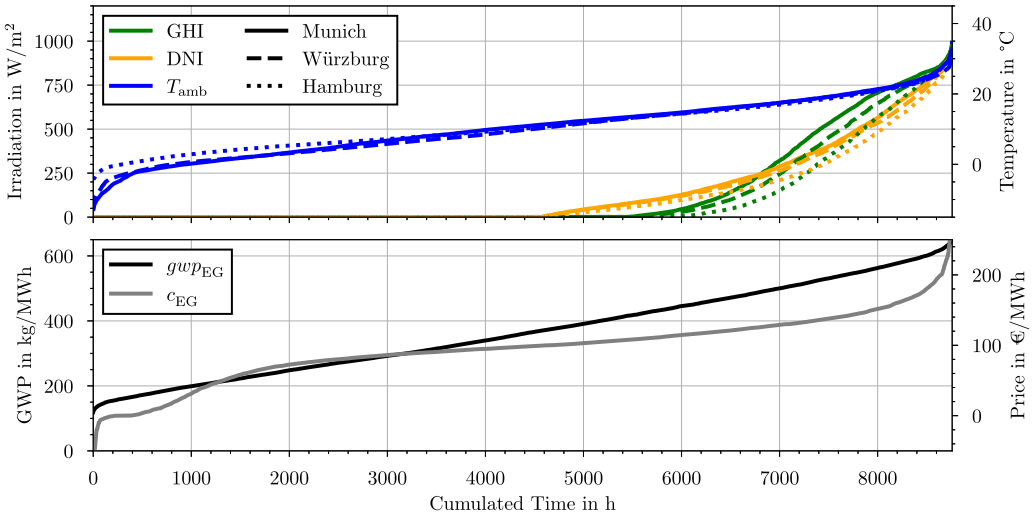

Fig. 3. Duration curves of meteorological data (top) and electricity market data (bottom) for the investigated sites with low (Hamburg), medium (Würzburg) and high (Munich) irradiation.

Nevertheless, most of the constraints are nonlinear with respect to the operational variables, leading to a large-scale nonlinear nonconvex multi-objective optimization problem with seven design variables as well as approximately 27 operational variables and multiple constraints (depending on the configuration) for each 8760 h of the year, summing up to over 236 000 variables and hundreds of thousands of constraints. Compared to (mixed-integer) linear problems, nonlinear nonconvex optimization problems of this size are generally very difficult to solve for global (but also local) optimality. Formulations based on mass and energy balances using both temperature and mass flow lead to nonconvex nonlinearities. Because we are particularly interested in the behavior of these variables when it comes to finding the optimal operating strategy, no linearization techniques are used here. Instead, the underlying single-stage problem (1) is split into a two-stage optimization problem by decoupling the design and operation, which enables the application of temporal decomposition techniques for the operational variables and constraints (see Section 2.6.2).

In the first stage (design), the capacity of each system component involved in the SHS is optimized to obtain Pareto-optimal solutions for TAC and AOE:

$$\begin{aligned} \min_{\boldsymbol{x}} \quad & \Big[TAC\left(\boldsymbol{x}, P^{\star}_{\mathrm{EG}}(t_1), \dots, P^{\star}_{\mathrm{EG}}(t_{N_\mathrm{t}})\right), \\ & AOE\left(P^{\star}_{\mathrm{EG}}(t_1), \dots, P^{\star}_{\mathrm{EG}}(t_{N_\mathrm{t}})\right) \Big] \\ \text{s.t.} \quad & 0 \le x_j \le x_{j,\max} \quad j = 1, \dots, 7. \end{aligned} \tag{2}$$

For each design evaluation of TAC and AOE as a function of $\boldsymbol{x}$, the optimized power drawn from the grid calculated in the second-stage operational optimization is inserted and denoted as $P^{\star}_{\mathrm{EG}}(t_i)$. The design variables are limited because of various economic, environmental, and technical aspects. Therefore, the linear inequality design constraints must hold for the capacity of the components with a lower bound of zero and component-specific upper bound of $x_{j,\max}$ for each component j.

In the second stage (operation), the operating strategy is optimized to determine the energy flows, mass flows and temperatures that minimize the KPIs, based on a fixed set of component capacities $\boldsymbol{x}^{\star}$. To simplify the evaluation of the optimized operating strategy, we focus on the optimization of operational costs and neglect the environmental impact. Thus, a single-objective optimization problem can be formulated by minimizing the annual variable $OPEX_{\mathrm{var}}$ (A.6) of the SHS for a given design $\boldsymbol{x}^{\star}$ as follows:

$$\begin{aligned} \min_{\boldsymbol{y}_{t_1}, \dots, \boldsymbol{y}_{t_{N_\mathrm{t}}}} \quad & OPEX_{\mathrm{var}}\left(P_{\mathrm{EG}}(t_1), \dots, P_{\mathrm{EG}}(t_{N_\mathrm{t}})\right) \\ \text{s.t.} \quad & \boldsymbol{h}\left(\boldsymbol{x}^{\star}, \boldsymbol{y}(t_1), \dots, \boldsymbol{y}(t_{N_\mathrm{t}})\right) = \boldsymbol{0}, \\ & \boldsymbol{g}\left(\boldsymbol{x}^{\star}, \boldsymbol{y}(t_1), \dots, \boldsymbol{y}(t_{N_\mathrm{t}})\right) \le \boldsymbol{0}. \end{aligned} \tag{3}$$

Briefly, the two-stage optimization problem consists of two optimization problems with separate objectives and decision variables. The first stage can be solved by iteratively evaluating the second stage with a given set of design variables $\boldsymbol{x}^{\star}$ to obtain the optimal operational variables $\boldsymbol{y}^{\star}(t_i)$ and with those the optimal EG power flows $P^{\star}_{\mathrm{EG}}(t_i)$. The iterative nature of the two-stage problem is illustrated in Fig. 4.

2.6.2. Solution algorithm

Multi-objective optimization problems in the field of techno-economic analysis of energy supply systems are often solved by transformation into several single-objective optimization problems. A popular technique for this class of methods is the (augmented) ε-constraint method [49], in which only one objective function (e.g. TAC) is considered and the other (e.g. AOE) is integrated into the constraints bounded by ε. Thus, the multi-objective optimization problem is transformed into a series of single-objective optimization problems with a set of ε-constraints. This technique is well-suited for single-stage problems that can be solved effectively and is therefore often applied to (mixed-integer) linear problems (e.g. [31–33,50]). However, in our case, a two-stage problem is formulated to handle the large set of variables and constraints along with nonlinearities, making such transformative approaches no longer practical. Instead, an iterative approach is applied, which is well-suited to the two-stage formulation of our optimization

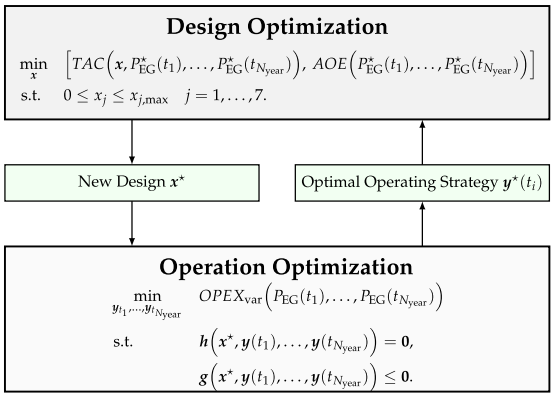

Fig. 4. Schematic representation of the iterative approach to solving the multi-objective design and operation optimization problem based on decoupling the original problem into two stages.

problem (see Fig. 4). This means that two different optimization methods are iteratively used: one for the design stage and one for the operational stage. Such approaches for solving multi-objective optimization problems with multiple stages are also very common in the area of energy supply systems (e.g. [51–54]). In the iterative approach, we can apply blackbox optimization methods in the first stage (2), which handle the trade-off between the multiple objectives directly without transforming them into single-objective problems, whereas derivative-based optimizers can be used in the second stage (3), which allows us to further decompose the operation optimization problem to handle the problem size and nonlinearities. The proposed algorithm to solve the two-stage optimization problem introduced in Section 2.6.1 is shown in detail in Fig. 5.

To solve the multi-objective design optimization problem in the first stage (2), the non-dominated sorting genetic algorithm (NSGA-II) [55] is used, which is a popular method for multi-objective blackbox optimization (e.g. [56–59]). NSGA-II is a blackbox algorithm that iteratively evaluates the objectives for a population of N_{pop} different designs and applies non-dominated sorting, selection, crossover, and mutation operations to build a new population; with the aim of finding promising new designs while exploring the design variable space. Therefore, in each generation of the algorithm, a new population is built and evaluated until a certain termination criterion is reached. In our case, the algorithm terminates after N_{gen} generations. Because NSGA-II treats the evaluation of the objectives as blackboxes, it imposes no restrictions on the formulation and solver used for the operation optimization in the second stage. Fortunately, all designs in a population can be evaluated independently, and thus, in parallel, so that the computational time can be drastically reduced by parallel computing. In our case, a design corresponds to a set of design variables $\boldsymbol{x}^{\star}$, or, more specifically, a set of component capacities.

For each set of component capacities proposed by NSGA-II, we solve the operation optimization problem in the second stage (3) in parallel. For this purpose, the corresponding constraints defining the configuration (see Sections 2.3 and 2.4) as well as meteorological and market data (see Section 2.5) are used. The resulting large-scale multiperiod optimization problem is nonlinear and nonconvex and can generally be solved using global or local methods. Because global solvers are computationally expensive for this class of problems, we use a local nonlinear programming solver. In particular, the popular, open-source, and very efficient IPOPT [60] solver is applied. Although IPOPT is a powerful method for solving large-scale nonlinear nonconvex constrained optimization problems, it is impractical to solve the underlying problem for a TOY without decomposing the year. The entire year would result in an extremely large-scale nonlinear nonconvex problem with hundreds of thousands of operational variables and constraints that cannot be solved efficiently. To address this problem, two decomposition steps are applied to (3). First, we use representative time periods by time series aggregation [61], a common method in energy system analysis, to reduce the total number of time grid points and, thus, the number of variables and constraints involved. In doing so, annual meteorological and market data are clustered using the k-medoids algorithm to derive N_{p} representative periods, where each period has a length of N_{d} days. On this basis, time-dependent values that are independent of the optimization are calculated by preprocessing, for example, the available irradiance on the STC and PV modules. With these inputs, the optimization problems are built for each representative period i. To optimize the representative periods independently of each other, we apply identical circular conditions at the beginning and end of each period, which define the SOC of the BESS and the TES temperature. As a result, when recomposing the entire year from the representative periods, each period can be followed by all other representative periods without harming the annual energy balance. Because the operation optimization problem formulated over one period can still consist of several thousand variables (depending on N_{d}), a second decomposition step is applied, and a 24 h rolling horizon with a 48 h look-ahead is introduced. This means that we successively calculate the optimal operating strategy for the entire period by running an optimization for each day j. More specifically, we start with an optimization over the first 48 h using the circular conditions as the initial values, but we fix only the first 24 h of the optimal operating strategy as the result. Then, the horizon is shifted by 24 h, using the last values of the fixed result as initial conditions, and the operation optimization is solved again over 48 h to fix the next 24 h as a result. This procedure is performed successively until the last day of the period is reached, where we only solve a 24 h optimization problem and impose the circular conditions on the last time point. Then the optimal operating strategy for the period is available as a sequence of the fixed results and the next period can be optimized accordingly. Owing to the rolling horizon approach the decomposed optimization problem has to be solved multiple times, but with a significantly smaller number of variables and constraints (less than 1300), which can be performed very efficiently with IPOPT. The larger optimization horizon of 48 h serves to incorporate the following day into the optimal operating strategy, particularly for optimized storage utilization to dispatch around the volatility of solar irradiation and grid prices. Another aspect associated with the use of local methods such as the IPOPT solver is the quality of the optimization results. Local methods naturally compute fast solutions (depending on the starting point) but typically get stuck in local minima, which can have a much larger objective function value than the global minimum. Consequently, suboptimal solutions at the operational stage may lead to poor evaluations of the given designs. To reduce the probability of IPOPT getting stuck in local minima, multi-start algorithms are often used in practice (e.g. [62–64]). This implies that the local search is performed from N_{s} random starting points and the local solution with the best objective function value is selected. With this methodology, it is possible to compute near-optimal operating strategies for each of the representative periods, which are then recomposed into an entire year and yield the optimal operating strategy $\boldsymbol{y}^{\star}(t_i)$ or more specifically, the TOY. Post-processing of the TOY is then performed to calculate the KPI values required by NSGA-II to create the next population of designs. By using the clustering, rolling horizon, and multi-start approaches, it is not possible to guarantee that the global optimum of the optimal operating strategy will be found, but the computational effort can be significantly reduced and near-optimal solutions can still be achieved, which is sufficient for our purpose. This allows us to analyze the SHS, including all relevant nonlinear dependencies in mass flow and temperature, while evaluating a sufficient number of designs to find a well-established Pareto front for the KPIs. The entire algorithm is implemented in *Python*, and we use the *tsam* package [65] for time series aggregation, the *pymoo* package [66] for design optimization with NSGA-II, and the *pyomo* package [67] for operation optimization with IPOPT.

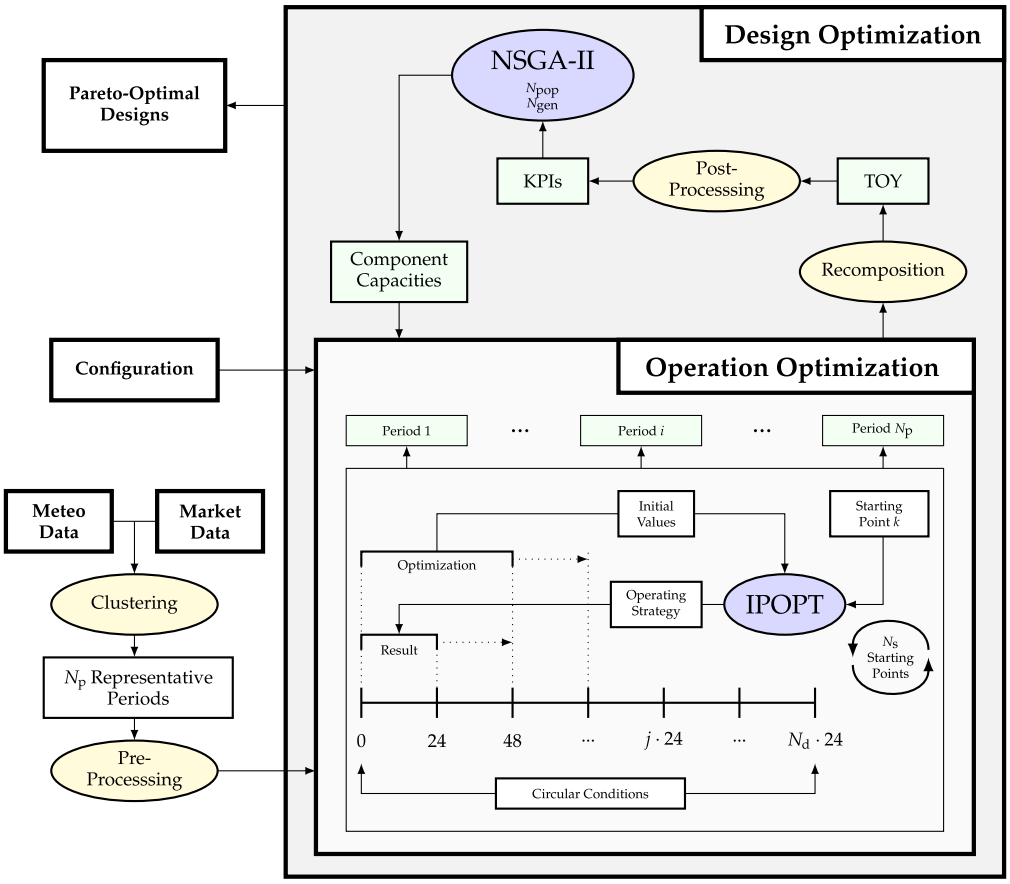

Fig. 5. Schematic visualization of the proposed optimization algorithm.

3. Results

In this section, we present the results of 18 techno-economic optimization runs we performed, one for each combination of the six SHS configurations defined in Section 2.4 and the three representative sites introduced in Section 2.5. In Section 3.1 we describe how we set up the optimization algorithm and in Section 3.2 we present the corresponding results.

3.1. Optimization setup

The algorithm presented in Section 2.6.2 still contains some user-defined parameters to be selected such as the number of generations and the population size for NSGA-II, N_{gen} and N_{pop}; the size and number of cluster periods, N_d and N_p; and the number of multi-starts per IPOPT run N_s.

We performed the optimizations on a workstation with 96 GB of RAM and an Intel(R) Xeon(R) Gold 6240R CPU with 48 cores. For NSGA-II, we set a population size $N_{pop} = 72$ and use 36 cores for the parallelization of the TOY evaluations. Furthermore, we also found (in undocumented tests) that $N_{gen} = 40$ generations lead to well-established Pareto fronts for our study, meaning that 2880 different designs were evaluated for each SHS configuration at each site. All other parameters within NSGA-II such as the mutation and crossover probabilities were set to *pymoo* defaults.

For time-series aggregation, we use a period size of $N_d = 7$ days and a total of $N_p = 4$ periods. We use a relatively large period size to reduce the total number of periods and thus the influence of the circular conditions applied at each start and end of each representative period. We set these values to the minimum storage capacity for TES and BESS to avoid unnecessary charging, but it is not known whether this is the optimal value for each optimization run. Nevertheless, we show in Appendix C that the solutions obtained by clustering do not deviate significantly from those calculated over an entire year.

The multi-start approach for finding near-optimal solutions for each 48 h horizon in the operation optimization enables the use of efficient local solvers such as IPOPT, but it is not known in advance how many multi-starts N_s are necessary to compute near-optimal solutions. The higher N_s, the higher the probability of finding the global optimum, while at the same time the computational effort increases. For this reason, we have investigated the optimization problems in more detail with regard to determining a good value for the number of required starts N_s. In Appendix C, we show that for our application, a partially well-chosen starting point leads to a good and robust solution so that the reduced nonlinear optimization problems are solved with these in a single-shot ($N_s = 1$) instead of using multiple starting points. For all optimizations, IPOPT is run with the default convergence tolerance of 10^{-8}. The algorithm validation can be found in Appendix C.

In addition, the variable bounds for the operational and design variables must be defined. For the design variables, we set the following bounds with regard to the maximum HX heat of approximately 3 MW.

$$
\begin{aligned}
0 &\leq P_{\mathrm{EG,max}} \leq 6\,\mathrm{MW} \\
0 &\leq A_{\mathrm{PV}} \leq 30\,000\,\mathrm{m}^2 \\
0 &\leq E_{\mathrm{BESS,nom}} \leq 20\,\mathrm{MWh} \\
0 &\leq P_{\mathrm{BESS,nom}} \leq 3\,\mathrm{MW} \\
0 &\leq \dot{Q}_{\mathrm{HP,nom}} \leq 6\,\mathrm{MW} \\
0 &\leq A_{\mathrm{STC}} \leq 30\,000\,\mathrm{m}^2 \\
0 &\leq m_{\mathrm{TES}} \leq 1\,000\,\mathrm{t}
\end{aligned}
\tag{4}
$$

The maximum PV area corresponds to a nominal DC power of 6.3 MW and therefore a nominal AC power of 4.9 MW for a global tilted

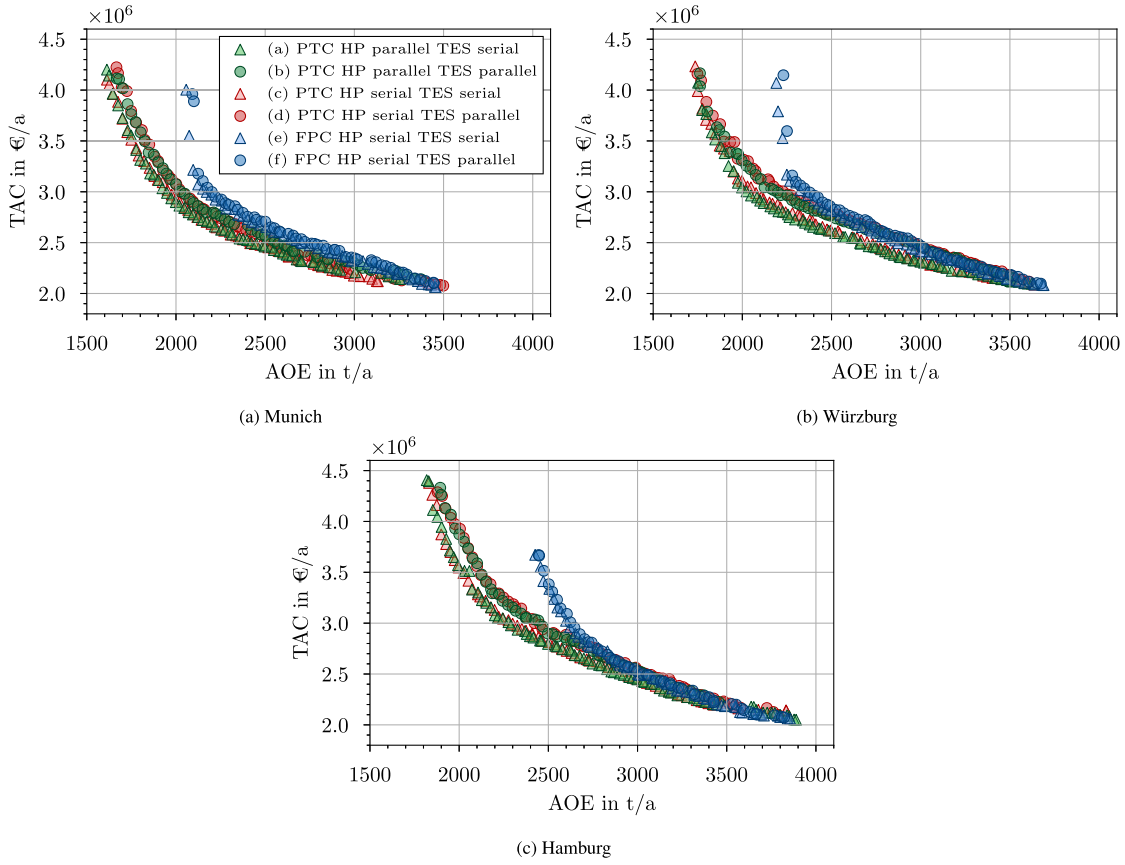

Fig. 6. Pareto-optimal results of TAC over AOE for all investigated SHS configurations at (a) Munich, (b) Würzburg and (c) Hamburg.

irradiance (GTI) of 1000 W/m^2, the maximum PTC area corresponds to a nominal heat output of 15.5 MW at 800 W/m^2 and the maximum TES mass corresponds to an energy capacity of 60.5 MWh for a nominal temperature difference of 200 °C. The operation optimization decision variables include all:

- power flows,
- mass flows,
- temperatures,
- and other state variables

describing the performance of the SHS components as presented in Appendix A. For the operational variables we allow oil mass flows between 0–45 kg/s and oil temperatures between 50–400 °C. For some components, such as the HP and TES, we use component-specific bounds, e.g. the maximum HP hot side temperature or the maximum TES concrete temperature. A complete set of parameter values, including operational bounds, is given in Appendix B. Using this setup, the optimization algorithm can be applied to each configuration presented in Section 2.4 to find optimal designs and operating strategies.

3.2. Optimization results

In this section, we present the optimization results, including the Pareto fronts of TAC over AOE for all SHS configurations and sites, as well as exemplary optimal design points and optimal operating strategies.

3.2.1. Comparison of configurations

Fig. 6 shows the Pareto-optimal results of TAC plotted over AOE for all SHS configurations at Munich, Würzburg and Hamburg. SHS configurations with an identical connection of STC and HP are marked in the same color; for TES, we use a triangle to indicate a serial connection and a circle to indicate a parallel connection.

For each SHS configuration at each site, we observe well-established Pareto fronts, indicating that the number of generations used in NSGA-II is sufficient. In addition, the Pareto fronts show the expected behavior of increasing costs for decreasing emissions. For all sites, we find SHS solutions with a minimum TAC of approximately 2.0 M€/a for an AOE between 3500–4000 t/a, and a minimum AOE of 1100–1300 t/a for a TAC between 4.1–4.4 M€/a. Notably, the higher the AOE, the closer the Pareto fronts of the different SHS configurations become, particularly for the Würzburg and Hamburg sites. Nevertheless, for each site, the SHS configurations with FPC (blue) show higher TAC than the SHS configurations with PTC (green and red), especially for low AOE solutions. For SHS configurations with PTC, the serial TES connection (triangle) shows a lower TAC than the parallel TES connection (circle) over the entire AOE range at all sites. For the parallel (green) and serial (red) connections of the PTC and HP, no clear deviation is observed.

To enable a proper comparison of the SHS performance depending on configuration and site, in Fig. 7 we plotted only the minimal TAC points for each AOE value over all SHS configurations, extracting the best performing SHS configurations for each site. It is clear that a combination of PTC and HP in serial or parallel with a TES in serial (red and blue triangles) shows the lowest TAC over the largest share of the AOE range, and only towards maximal AOE do the SHS configurations with FPC (blue) become cost comparable to those with PTC. In these Pareto fronts showing only the SHS configurations with minimal TAC, both PTC and HP in parallel (green) and series (red) are represented, with a slight dominance of the SHS configuration with PTC and HP in parallel (green). Hence, we can state that an SHS configuration with PTC and HP in parallel and TES in series performs best over the entire AOE range for all sites.

Comparing the optimal SHS solutions over the three different sites, we can see that the Pareto fronts move to lower TAC and AOE values

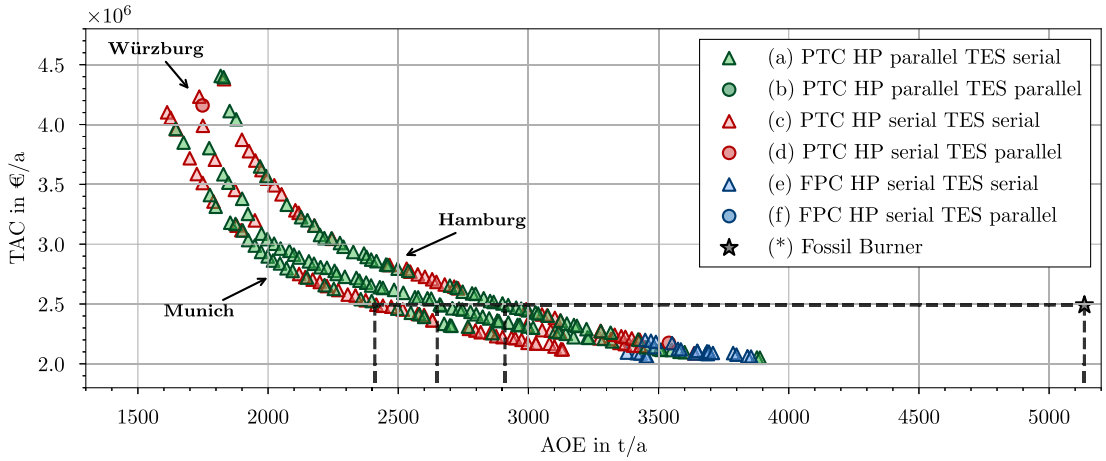

Fig. 7. Pareto-optimal results of TAC over AOE for the SHS configurations with minimal TAC at the sites Munich, Würzburg and Hamburg compared to the gas burner (GB) solution.

with higher annual irradiation. This indicates a dependence of the SHS performance on the available solar irradiation utilized by STC and PV. Notably, this dependence decreases with increasing AOE as the Pareto fronts move closer in this direction. To place the results in a broader context, we calculated and added the TAC and AOE of a gas burner system that provides heat to the HX instead of the SHS. The assumptions used for this reference solution are provided in Appendix A.4. The GB solution has a TAC of 2.48 M€/a and AOE of 5111.84 t/a. The dotted lines show the TAC intersections of the fossil GB solution with the SHS Pareto fronts, leading to SHS solutions that are cost-competitive to the fossil GB solution but have significantly lower AOE of 2412 t/a in Munich, 2651 t/a in Würzburg, and 2909 t/a in Hamburg. This means that SHS can reduce the AOE by 48% on average.

3.2.2. Optimal design points

To investigate the reasons why SHS configuration (a) with PTC and HP in parallel and TES in series performs best, Fig. 8 shows the design points and corresponding minimal TAC plotted over the AOE for this SHS configuration at Munich, Würzburg, and Hamburg. For each site, the upper graph shows the component capacities of different design points over the AOE, where each design point contains the capacities of all SHS components (EG, PV, BESS, STC, HP, and TES). For this SHS configuration, STC corresponds to concentrating PTC; therefore, we refer to PTC instead of STC in the following analysis. The left y-axis shows the thermal or electric nominal power capacities of EG, PV, PTC, and HP, whereas the right y-axis shows the electric or thermal energy capacities of BESS and TES. The lower graph shows the corresponding minimal TAC values for each design point plotted over the AOE such that the KPIs and their corresponding design points align vertically.

The design points show qualitatively comparable behaviors of the changes in the optimal component capacities depending on the AOE for all sites. The EG capacity shows a rather constant behavior over the AOE, with a mean value of 1.57 MW, except for minimal AOE values, where a slight increase can be observed. The HP capacity also shows constant behavior over the AOE range, with a mean capacity of 3.3 MW. The PTC capacity is close to its upper bound of 15.5 MW nominal heat output (equivalent to 30 000 m^2 collector area) for minimal AOE and decreases rapidly with increasing AOE until a plateau is reached for medium AOE. Towards minimal TAC, the PTC capacity decreases again until it reaches zero. The value and width of the plateau region vary depending on the site, whereas the qualitative behavior of PTC capacity is similar for all sites. PV shows a similar trend of decreasing capacity with increasing AOE but reaches its upper bound of 6.3 MW nominal DC power (equivalent to 30 000 m^2 module area) for medium AOE values and does not reach zero for the minimal TAC points. At minimal TAC, the PV capacity is the highest for Munich with the highest irradiation and the lowest for Hamburg with the lowest irradiation. For all sites, the TES capacity shows a plateau with a value near its upper bound of 60.5 MWh energy capacity (equivalent to 1000 t concrete mass), and then a decrease in capacity with increasing AOE. Again, the AOE range of the plateau and TES capacity at minimal TAC differ depending on the site, with the highest capacity in Munich and the lowest in Hamburg. The BESS shows a similar behavior for all sites as well, with a maximal capacity of 12.3 MWh for minimal AOE and a capacity decrease to zero, which is already reached for medium AOE values and remains towards minimal TAC. Interestingly, the BESS capacity does not reach its upper bound of 20 MWh at minimal AOE. Some capacity variables, such as the TES capacity curves, show minor fluctuations over the AOE, which can be attributed to the use of NSGA-II. The algorithm does not guarantee global optimality, and such minor fluctuations in the design space can often be observed for some variables, even if the solution space is well-converged. Therefore, we do not elaborate on these fluctuations. Observing the change in the component capacities over the AOE, we can see that, in general, the component capacities increase with decreasing AOE, and vice versa. Therefore, TAC increases with decreasing AOE owing to the higher CAPEX for larger PV, PTC, TES, and BESS capacities. These capacities enable the system to collect and store more solar energy, thereby minimizing the EG power consumption and operating emissions. The EG and HP capacities do not change significantly over the AOE because the HP needs to meet the peak demand when no solar irradiation is available and TES is fully discharged, enabling the SHS to provide a 100% supply solution. An SHS solution without HP and EG would only be possible if PTC and TES would reach capacities large enough to collect and store sufficient energy to fulfill the demand at any time, which often leads to unreasonably high CAPEX for the investigated geographical region. A zero-emission SHS solution with HP but without EG could be obtained with large PV, BESS, PTC, and TES capacities, but is not present in the optimization results at hand. Here, the SHS reaches minimal AOE values between 1700 t/a and 1900 t/a, depending on the site. This can be attributed to the upper bounds set for the PV, PTC, and TES capacities. The TES and PV capacities already reach their upper bounds for medium AOE values, and the PTC capacity reaches its upper bound for the minimal AOE point. Therefore, the minimal AOE points that can be found are limited by the bounds set for design optimization. In contrast, the minimal TAC points indicate designs with only PV, HP, and TES. All other component capacities are set to zero by the optimizer. This shows that the optimizer trades high CAPEX, which depends on the component capacities, for increasing AOE, which depends on the EG power consumption, to achieve low TAC solutions. The PV and TES capacities at minimal TAC depend on the site and, therefore, the available irradiation. For Munich (high irradiation) we have a PV

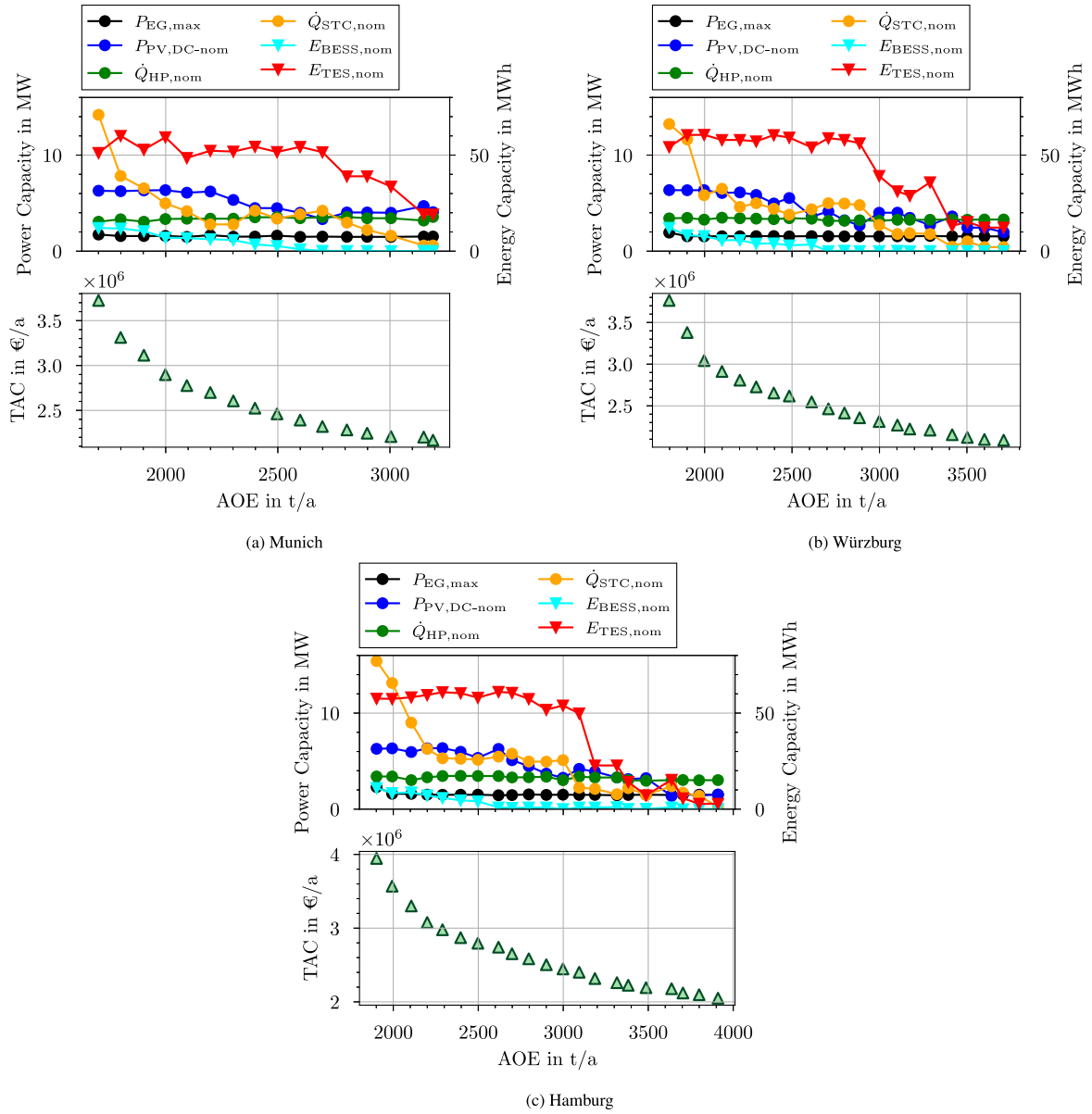

Fig. 8. Optimal component capacities and corresponding Pareto-optimal TAC over AOE for SHS configuration (a) with PTC and HP in parallel and TES in series at the sites (a) Munich, (b) Würzburg and (c) Hamburg.

capacity of 4.05 MW (19 100 m^2 module area) and a TES capacity of 19.4 MWh (318 t concrete mass) while for Hamburg (low irradiation) we have a lower PV capacity of 1.5 MW (7100 m^2 module area) and a significantly lower TES capacity of 2.8 MWh (45.5 t concrete mass). For Würzburg (medium irradiation), we have values in between, showing a trend of decreasing PV and TES capacity with decreasing available irradiation at minimal TAC. These trends can be explained by the optimizer attempting to reduce component capacities, trading CAPEX for increasing variable OPEX. The less irradiation is available, the lower the financial benefit of building a large PV field and TES (to use PV power for running the HP and storing the heat in the TES) becomes compared to buying electricity from the EG. Therefore, PV and TES capacities decrease with available irradiation. At the same time, AOE increases because with less renewable PV power available, the EG power consumption increases, which leads to AOE values of 3900 t/a at minimal TAC for Hamburg (low irradiation) followed by 3700 t/a for Würzburg (medium irradiation), and 3400 t/a for Munich (high irradiation). The minimal TAC values for all sites are close to 2.0 M€/a. This can be explained by the increasing EG power consumption, thereby increasing the importance of EG power prices, which are, other than the available irradiation, independent of the site. With regard to these relations, we can also explain why the Pareto fronts for the different sites in Fig. 7 move closer together towards higher AOE values. For low AOE values, we have large PV, PTC, and TES capacities to minimize the EG power consumption; therefore, CAPEX increases at all sites. At the same time, at sites with higher irradiation, the available PV power and PTC heat increase more significantly with increasing PV and PTC capacities than at sites with lower irradiation. This leads to lower CAPEX for similar AOE at sites with higher available irradiation. Additionally, the capacities of PV and TES already reach their upper bounds for medium AOE values; therefore, the CAPEX for these components is similar for all sites towards minimal AOE. However, the available PV power is higher for higher available irradiation, leading to lower variable OPEX, and therefore, lower TAC values. Towards minimal TAC, the Pareto fronts for the different sites move closer together because the dependency on the available irradiation decreases with decreasing PV and PTC capacity. Therefore, the driving cost component is the variable OPEX, which depends on EG prices, and those are identical for all

sites. Furthermore, at medium TAC values of 2.48 M€/a, we have optimal design points that are cost-competitive with the fossil burner solution. For all sites, these design points contain PV at medium to high capacity, PTC at medium capacity, TES at high capacity, and BESS at low to zero capacity. For PV and PTC, we can see varying component capacities for the medium AOE range. Both capacities are lower than their upper bounds, which means that the optimizer finds trade-off solutions between the PTC capacity, providing heat from direct irradiation with high efficiencies but also higher CAPEX, and PV capacity, providing power from direct and diffuse irradiation with low efficiencies but also lower CAPEX. Additionally, PV power can only be used to supply the HX after a conversion into heat via the HP, therefore we need to compare PTC with PV and HP together. For the design points considered the HP has a COP between 1.85 and 3.45 with a mean of 2.05; the PV efficiency after inverters has a maximum value of 20.4% and a mean value of 12.6% excluding zero. By multiplying the PV AC power with the COP and relating the result to the available solar power on the PV modules, we can calculate the efficiency of heat provided by PV and HP, which shows a maximum of 37.6% and a mean of 22.7%. Compared to this, the efficiency for heat provided by PTC has a maximum of 61.3% and a mean value of 39.4%. Therefore, PTC utilizes the available irradiation more efficiently than PV and HP to provide heat. However, PV utilizes direct and diffuse irradiation, in particular the GTI, while PTC is bounded to direct irradiation, more specifically the DNI, whose annual sum is lower than that for the GTI at the sites investigated. Additionally, in our case the HP is required independent of PV to supply the demand in periods with no irradiation. Therefore, the investment decision compares PTC directly to PV and not to PV and HP together, favoring low-cost PV. Nevertheless, a combination of both PTC and PV leads to the lowest TAC for solutions that are cost-competitive to a fossil burner, reducing the operating emissions by 48% on average.

3.2.3. Optimal operating strategies

Fig. 9 shows the optimal operating strategy for an optimal design point with a TAC of 2.48 M€/a for the SHS configuration with PTC and HP in parallel and TES in series at site Würzburg. The component capacities of the design point are as follows: $P_{\mathrm{EG,max}} = 1.54\,\mathrm{MW}$, $P_{\mathrm{PV,dc\text{-}nom}} = 4.86\,\mathrm{MW}$, $E_{\mathrm{BESS,nom}} = 0\,\mathrm{MWh}$, $P_{\mathrm{BESS,nom}} = 0\,\mathrm{MW}$, $\dot{Q}_{\mathrm{HP,nom}} = 3.29\,\mathrm{MW}$, $\dot{Q}_{\mathrm{PTC,nom}} = 4.53\,\mathrm{MW}$, $E_{\mathrm{TES,nom}} = 58.7\,\mathrm{MWh}$. From top to bottom, the figure shows the stacked electric power balance, including the power sent to the HP and the EG power price; the stacked heat balance, including the demand in form of the HX heat; the operating temperatures of PTC, HP, TES, and HX; and the mass flows through PTC, HP, and HX. For the power balance, the area between $\dot{P}_{\mathrm{BESS,ch}}$ and $\dot{P}_{\mathrm{HP}}$ shows the energy used to charge the BESS and for the heat balance, the area between $\dot{Q}_{\mathrm{TES,ch}}$ and $\dot{Q}_{\mathrm{HX}}$ shows the energy used to charge the TES. The flows and temperatures are plotted over the same time axis, such that a vertical line through all four plots from top to bottom represents all values at the same time grid point. The left-hand side of Fig. 9 shows the flows and temperatures for a typical summer week, and the right-hand side for a typical winter week. It should be noted that the selected representation of the stacked heat flows should not be interpreted such that the bars between $\dot{Q}_{\mathrm{TES,ch}}$ and $\dot{Q}_{\mathrm{HX}}$ represent the share of HP and PTC heat used for charging. Because of this SHS configuration, PTC and HP heat are mixed before the oil can be sent to the TES; therefore, the charge heat flow is always a share of the total heat provided by PTC and HP together at the corresponding temperature level of the mixture.

For the summer week (left), we can clearly see the trade-off between the available PV power and PTC heat already indicated by the design results. Both, PV power and PTC heat, follow the available solar irradiation. Therefore, when the TES is charged, it is always charged simultaneously with PTC heat and HP heat powered by PV. For this SHS configuration with PTC and HP in parallel, the TES charge inlet temperature is calculated as a mixture of PTC and HP heat. During TES charging, the HP typically operates at its maximum outlet temperature of 250 °C. The PTC temperature shows peaks at the beginning and end of the charging process. When the TES is connected in series, the charging process reduces the temperature of the heat flow before it is sent to the HX. The HX oil inlet temperature cannot drop below a certain value owing to the HX coarseness, and the air outlet temperature is fixed at 200 °C. For low TES concrete temperatures at the beginning of the charging process, high charge inlet temperatures and, therefore, high PTC outlet temperatures are needed to maintain the charge outlet temperature and, therefore, the HX oil inlet temperature at a convenient level. At the end of the charging process, a high PTC outlet temperature is required because the TES concrete temperature approaches the maximum HP outlet temperature, and higher temperatures are required at the charge inlet to further increase the concrete temperature. The maximum TES concrete temperature corresponds to the maximum HP outlet temperature in this SHS configuration because the TES feeds the HP hot side during discharge, and is therefore limited by the HP performance bounds. When the TES is fully charged and solar energy is still available, the PTC and HP inlet and outlet temperatures decrease because the HX demand can be met at a lower temperature than that required for TES charging. When no solar energy is available, the TES is discharged, and the HP provides heat to the HX using power drawn from the EG. In the power and heat balances, we can see that during these times of EG power use, the TES discharge flows dispatch well around the fluctuating EG prices, meaning that for high EG prices, the EG power is minimized and the TES discharge is maximized, whereas for low EG prices, the EG power is maximized and the TES discharge is minimized. During TES discharge, the HP inlet temperature follows the TES discharge outlet temperature, and the HP outlet temperature is set slightly above the inlet temperature to maintain the minimum temperature lift of 10 °C on the HP hot side. If the TES outlet temperature falls below the HX inlet temperature, the HP hot side provides the temperature lift to meet the required HX oil inlet temperature. The necessary HX oil inlet temperature depends on the fixed air outlet temperature and HX mass flow. High mass flows lead to lower coarseness and, therefore, lower oil inlet temperatures, which can be beneficial for HP operation. For all scenarios in which the HP provides the HX demand and TES is not available, the HX mass flow is high to enable a minimal HX oil inlet and HP outlet temperature, which maximizes the COP. If higher oil temperatures are available by PTC or during TES discharge, the mass flow drops to increase the HX hot-side temperature difference. However, high mass flows can also be necessary if large PTC and HP heat flows are available, particularly during TES charging. The PTC and HP outlet mass flows add up and must pass the HX to return to the component inlets. Therefore, the optimizer sets the mass flows depending not only on the optimal outlet temperatures but also on the optimal heat flows. For the winter week (right), the heat balance shows that the demand is primarily supplied by the HP. On the one hand, there is low direct irradiation and, therefore, only a low amount of PTC heat is available. On the other hand, the power balance shows that PV, which can utilize direct and diffuse irradiation, provides a significant amount of power to the HP at four of the seven days. Again, the TES is charged when PV, low-cost EG power, or PTC heat is available and discharged when the EG prices show peak values, but only with small heat flows compared to the summer week, resulting in only minor changes in the TES concrete temperature. The HP outlet temperature either corresponds to the HX inlet temperature or lies slightly above it, mainly when the TES is charged. Mass flows are again set depending on the optimal outlet temperatures and heat flows.

By understanding these operational decisions, we can now elaborate on why the optimizer finds a trade-off between PTC and PV. PTC provides high efficiencies and high outlet temperatures, enabling better land usage and TES utilization; however, it shows higher CAPEX and is mainly operated in high irradiation periods, since it only utilizes direct irradiation. PV has a low CAPEX and can utilize direct and

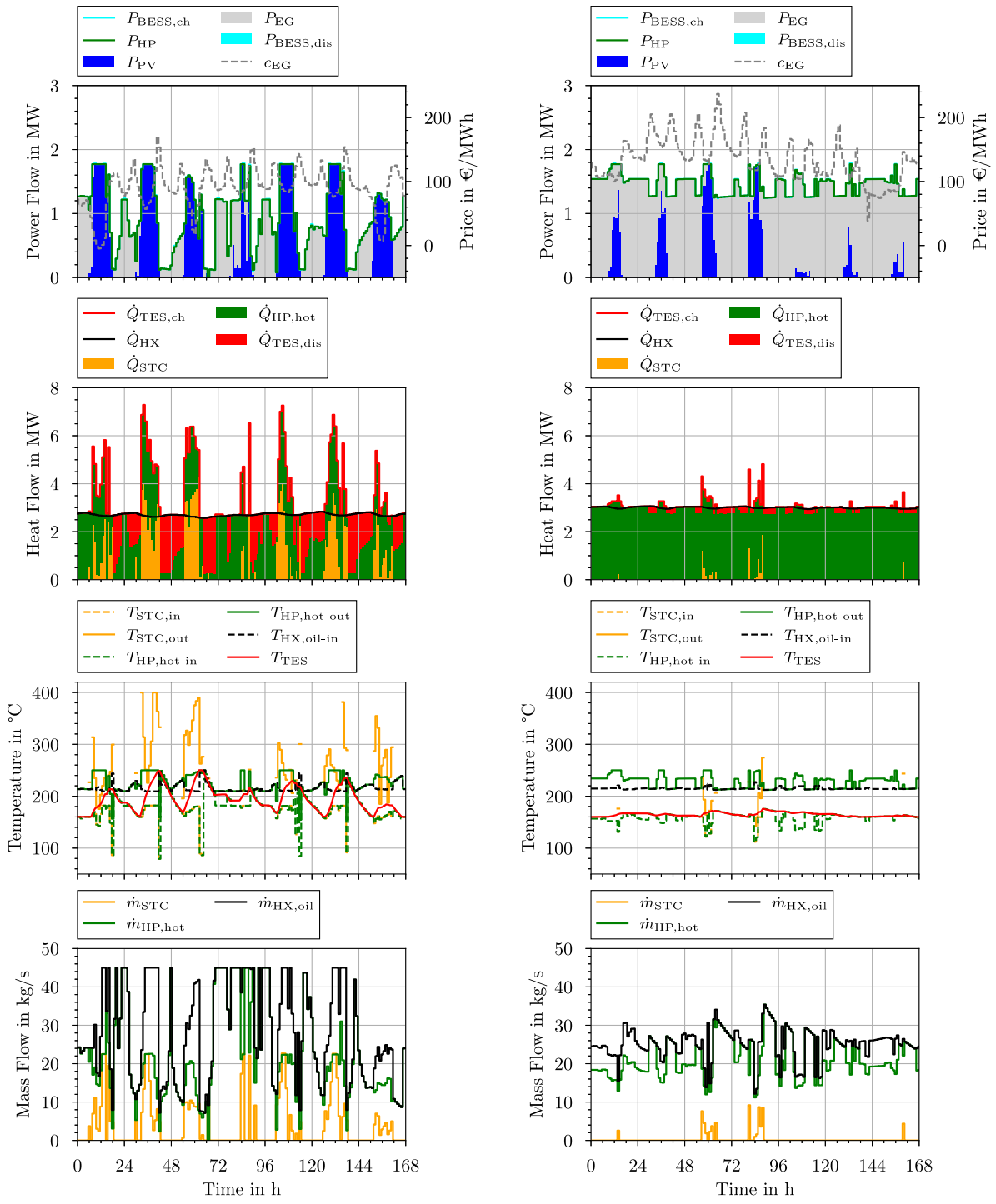

(a) Summer

(b) Winter

Fig. 9. Optimal operating strategy of SHS configuration (a) with PTC and HP in parallel and TES in series with an optimal design point at TAC of 2.48 M€/a at site Würzburg for a typical summer week (left) and a typical winter week (right).

diffuse irradiation, enabling it to also provide power during low direct irradiation periods; however, PV-HP heat has lower efficiencies than PTC heat and is bound to the lower outlet temperature limit of the HP. Therefore, the combination of both shows the best results in terms of minimizing TAC and AOE. The detailed operational results also enable us to understand why SHS configurations with TES in series are more beneficial than those with TES in parallel. In Appendix D, we provide the design and operational results for an SHS configuration with PTC and HP in parallel and TES in parallel. In theory, parallel TES enables higher concrete temperatures because the TES discharge outlet temperature is not bound to the HP hot-outlet temperature. However, the design results show that, for our use case and boundary conditions, the system still includes a large amount of low-cost PV, which can only provide heat via the HP at a maximum temperature of 250 °C. PV-HP heat is combined with high-temperature PTC heat, increasing the available TES charge temperature; however, the optimal ratio of PV and PTC capacities leads to maximum TES concrete temperatures that lie only slightly above 250 °C. Therefore, higher TES concrete

temperatures are possible with parallel TES, but are not provided because of the trade-off between PV and PTC. Additionally, during TES discharge, the HP needs to provide higher outlet temperatures to meet the demand temperatures in the HX with a parallel TES than with a serial TES. This leads to lower COP values and, therefore, higher EG power consumption. Consequently, the overall TES performance with TES in parallel is worse than that with TES in series. For Optimal SHS solutions with parallel TES and design points that are cost-competitive to a fossil burner solution, the optimizer even trades low-cost TES energy for high-cost BESS energy. In contrast, cost-competitive SHS solutions with TES in series do not include high-cost BESS because of better TES utilization. Finally, we can use the detailed operational results to explain why PTC and HP in series and parallel show similar results but why a configuration with PTC and HP in parallel shows slightly lower TAC. We provide the design and operational results for the SHS configuration with PTC and HP in series and TES in series in Appendix D. Compared to the configuration with PTC and HP in parallel, the serial solar producers lead to very similar results, except for the PTC inlet temperature. Higher PTC inlet temperatures in the serial connection lead to lower temperature gradients over the PTC and, therefore, higher mass flows and, more importantly, higher mean temperatures. This leads to higher thermal losses and, therefore, slightly higher OPEX compared to PTC and HP in parallel.

Notably, there are some significant jumps in the mass flows and temperatures of PTC, HP, and HX, especially during the summer period with high irradiation.

4. Discussion

Our study showcases that a combination of PV, PTC, HP and TES can efficiently cover a heat demand with a supply temperature of 200 °C for sites in Germany and reduce emissions by 48% on average, while still being cost-competitive to a fossil burner solution. However, the results must be interpreted with regard to the assumptions made in this investigation.

We investigated all configurations for a representative use case at 200 °C with a heat demand of 1.84 MW. Owing to economies of scale effects, the optimization results and thus the optimal designs for lower and higher demand values may differ. Considering the different scaling exponents of the components, a larger demand could favor PTC and TES capacity. Additionally, we assume a continuous and constant heat demand, while many processes are operated in batch mode. Such batch processes impose other challenges to the system, because the components need to cope with additional dynamics in the demand profile as well as possible mismatches between the times of available solar energy and heat demand. This could lead to larger TES and BESS or lower PV and PTC capacities. We also neglect the process cooling available on the HP air-side. In our study, the cold air at the HP source side is dissipated into the ambient environment. If the available cooling is remunerated, the TAC may be reduced and the HP could be preferred in the optimization. If a use case with additional process cooling demand is considered, the SHS design and operation would be adapted drastically, focusing on the HP providing the process cooling and dispatching the other components around it to fulfill the heat demand. Then, an additional cooling unit could also be included in the design optimization, as the HP is generally used to provide process heat, while process cooling can be considered more as a secondary supply.

To compare the configurations, the study is based on a green-field approach, i.e. no existing components or infrastructure for the energy supply are already available. In this way, we are able to assess the possibilities of fully sustainable heating solutions independent of fossil fuels that are needed onsite. In real-world scenarios, SHS are not only used for newly built processes or to completely replace existing fossil supply solutions, but also to supply existing fossil solutions and to enable a gradual transition towards a fully renewable supply. If the existing supply system and infrastructure (here the existing conventional fuel-based heating system) are included in the techno-economic assessment, which is referred to as the brown-field approach, the SHS would not need to supply 100% of the demand at all times and would therefore be able to dispatch around solar irradiation and EG prices with greater flexibility. Such calculations would lead to different design and operational solutions, which are not taken into account in our comparison.

When interpreting the optimal designs presented in this study, one should always bear in mind that the configurations are predefined, meaning that the placement of the components is not included in the design optimization process. We attempt to design the most common interconnections of the components at hand, but other configurations not considered here could lead to different optimization results. By comparing the optimization results, we found that a serial TES connection leads to the lowest TAC and AOE. A sophisticated TES connection enabling both serial and parallel discharge could lead to even higher TES usage and thus larger PTC and TES capacities, but this is not further investigated here. Moreover, in our setup, where DR return heat is available and connected to the HP cold side, FPC is not an attractive option compared to PTC due to the lower maximum outlet temperature it can provide inside the thermal oil cycle. For a use case without available return heat, FPC could be an attractive option to preheat the ambient air before being fed into the HP. This could reduce the temperature lift and thus increase the COP, which minimizes the EG power consumption.

The optimization results for the different configurations and sites are limited by the specified variable bounds, e.g. the operational bound for the maximum HP hot-side outlet temperature or the design bound for the TES capacity. Currently, Brayton-cycle high-temperature HPs can provide outlet temperatures up to 250 °C, which makes PTC an attractive option for hybridization as it can provide temperatures up to 400 °C using thermal oil as heat transfer fluid. Our investigation shows that the higher PTC outlet temperatures are significantly beneficial to the TES charge process. When HPs also reach higher outlet temperatures in the future, a system solution with only low-cost PV, HP, and TES could be more cost-effective for process demands of approximately 200 °C in Germany, especially for sites with lower irradiation. Furthermore, the Pareto-optimal results strongly depend on the design variable bounds, as PV, STC and TES, for example, reach their upper capacity bounds at minimum AOE values. Lower AOE solutions can be achieved with larger upper bounds for these components. We set these bounds with regard to reasonable limitations in the available land area for PV and STC and with a maximum storage capacity that covers the demand for over 20 h. Because the PV capacity already reaches its upper bound for medium AOE values, it would be interesting to set a constraint limiting the total land area and adapt the PV and PTC capacities such that both individually can cover the total land area. By doing so, the trade-off between PV and PTC towards minimal AOE could result in higher PV and lower PTC capacities. Nevertheless, for the design points that are cost-competitive to the fossil burner solution, both capacities do not reach their upper bounds; therefore, such an adaptation would not affect these results. Regarding the TES upper bounds, we observed in our study that the TES does not reach its upper temperature limit of 360 °C owing to the trade-off between PV and PTC, which limits the maximal charge temperature. Consequently, the temperature gradient between the fully charged and discharged states is 100 °C, which is only half of the expected nominal value of 200 °C. This leads to an energy capacity that is also half of the expected nominal value. Based on this, the actual TES capacity only covers approximately 10 h of heat demand and a larger TES capacity bound could lead to even lower AOE solutions.

The limitations in the minimal AOE also strongly depend on the global warming potential of the EG. With our assumption that these are identical for each year over the entire lifetime of the SHS, the future development of the renewable share in the EG is underestimated. We

have already identified SHS solutions that are cost-competitive with a fossil burner solution, assuming that today's EG emissions apply for the next 25 years. If decreasing EG emissions were taken into account in the future, a lower AOE than zero could be achieved in the calculations. To realistically interpret the global warming potential of the SHS, we could also consider the life-cycle emissions of all components, including their production, installation, and deconstruction. We did not include these factors here, because reliable values were not available for all components. However, we expect that the inclusion of life-cycle emissions could lead to slightly different results in favor of PTC and TES.

Moreover, the presented study focuses on Germany, limiting the results to meteorological and market conditions for this country. Germany has only medium to low available irradiation compared with other countries, such as Spain and Italy. With higher available irradiation, the authors expect a shift towards lower AOE and TAC values with increasing TES capacities. With increasing irradiation, PV and STC yield higher annual energy outputs at identical capacities and, therefore, identical investment costs, leading to an additional decrease in power demand but also an increase in storage capacity demand. However, the methodology presented in this study can easily be applied considering other meteorological and market conditions to investigate the techno-economic performance of the proposed SHS configurations in other countries. Owing to the coupled optimization algorithm introduced in this study, optimal designs and operating strategies can be identified depending on the meteorological and market conditions and thereby used to identify country-specific synergies between solar energy and high-temperature heat pumps.

Despite these limitations, our study reveals that synergies of PTC, PV, HP and TES enable the provision of cost-competitive and low-emission process heat at temperatures of approximately 200 °C in Germany. The HP offers a solution to cover the heat demand with low EG power consumption as long as an appropriate waste heat source for the cold side is available. It is dimensioned such that it can fulfill the demand independently of the other components, enabling a 100% supply of process heat. PV is used to power the HP when solar energy is available, which leads to a reduction in EG power consumption and therefore operational expenses and emissions. To enable the system to dispatch for fluctuations in EG prices, the TES can be charged by the HP during high irradiation periods. A BESS is less attractive than a TES due to its significantly higher investment costs. In times of available direct solar irradiation, PTC supports the TES charge process by enabling lower minimum and higher maximum temperatures with high-efficiency solar heat at high outlet temperatures. Owing to the trade-off between available PV power and PTC heat during high irradiation periods, a serial TES connection that limits the maximal TES temperature to the HP outlet temperature is still advantageous as it allows lower HP outlet temperatures during discharge and thus higher COP. Exploiting these synergies between PTC, PV, HP and TES, the SHS is able to effectively dispatch the fluctuating solar irradiation and EG prices, leading to low-cost and low-emission solutions.

We were able to identify these synergies due to the detailed nonlinear component models used in our optimization process, showing complex dependencies between temperatures, mass flows, heat flows and power flows. To solve this nonlinear optimization problem efficiently, computational simplifications are applied that influence the solution quality.

We reformulated the problem into two stages, including only costs and not emissions in the operational objective to apply derivative-based solvers for the operation optimization and blackbox solvers for the design optimization. Although the emission curves often follow the EG prices, the inclusion of AOE into the operation optimization could lead to lower minimal AOE values, but this results in a multi-objective optimization problem on the operational stage and would therefore require methods to incorporate both objectives into the optimization algorithm. We also used time series aggregation, including circular conditions, to reduce the problem size of the operation optimization. By doing so, errors are induced in the meteorological and market data as well as restricted storage use at the start and end of each representative period. The optimization over an entire year leads to slightly deviating results towards minimal AOE, where the influence of meteorological and market data as well as TES usage is the highest. However, the results with clustering generally represent the Pareto fronts well, especially for medium and high AOE.

Another important aspect is the level of model detail used for techno-economic optimization. We were able to include nonlinear effects in the operation and design stages, making it possible to analyze temperature levels and mass flows at any time point. Nevertheless, the model depth could be further increased to reflect other relevant effects. The optimization results show temperatures and mass flows with partially high fluctuations, especially during times of high irradiation. These fluctuating load point changes can appear due to the assumption of steady-state energy balances for STC, HP and HX, neglecting transient effects such as thermal inertia and ramp conditions. Transient effects can strongly influence the operational behavior, especially for thermal components (STC, HP, TES, and HX). Therefore, it is unclear whether the fluctuating load point changes given in the optimal operating strategies can be implemented in real industrial applications. By incorporating transient effects into the operation optimization, these uncertainties could be reduced to bring the operating strategies closer to reality, but it would probably require further algorithm development to handle the increasing model complexity. Furthermore, the authors assume that neglecting transient effects does not strongly influence the optimal designs and synergies presented in this study, as the assumption of using stationary energy balances goes along with hourly time steps, which are large compared to the duration of many transient processes occurring in the investigated SHS. Nevertheless, including longer duration transient effects into the operation optimization, such as start up and shut down of thermal components, could lead to an increase in TAC and AOE values and increase the storage capacity requirements, as fluctuations in the available irradiation or the EG prices need to be buffered accordingly. Furthermore, in this study, auxiliary electric power requirements of the thermal components are neglected. Including them would lead to slightly higher EG power consumption and thus to higher OPEX and AOE. While many auxiliary power demands are modeled as constants, they also include pumping power and pressure losses that could penalize high mass flows and therefore influence optimal operation. Finally, a higher level of detail can be used in the component models, e.g. a spatially discretized TES model or temperature-dependent fluid properties. Although these additions would improve the solution quality and bring the optimal designs and operations closer to reality, it is unclear whether the additional model complexity still allows these problems to be solved efficiently.

5. Conclusions

In this study, we analyzed the synergies of PV, STC, HP, BESS and TES to supply process heat demands at 200 °C in Germany. To this end, we selected a representative use case and defined six sustainable heating system configurations with different component interconnections. We then performed techno-economic optimizations for all configurations at three representative sites in Germany with low, medium, and high irradiation. The techno-economic optimizations output Pareto-optimal values for costs and emissions, particularly TAC and AOE, as well as the corresponding optimal component capacities and optimal operating strategies. The multi-objective optimization problems are formulated with nonlinear cost and performance models and solved using a newly proposed optimization algorithm that applies different decomposition techniques to handle model complexity. Our main conclusions based on the optimization results are as follows:

- The best-performing SHS configuration can reduce the AOE by 48% on average over all representative sites in Germany, while being cost-competitive to a fossil burner solution for the given use case. The solutions show a dependency on the available irradiation with decreasing TAC and AOE for sites with higher irradiation; however, even for low-irradiation sites in Germany, a cost-competitive AOE reduction of 43% is possible; for high-irradiation sites in Germany, we found a cost-competitive AOE reduction of 53%.
- The SHS configuration with PTC and HP in parallel and TES in series performs best for all sites. The most synergistic effects result from a system consisting of PV, PTC, HP, and TES, where HP supplies the base, PV powers the HP with low-cost and emission-free electricity, TES enables dispatching depending on EG prices and solar irradiation, and PTC provides high-temperature solar heat to support the TES charging process. FPC cannot reach sufficiently high outlet temperatures compared to PTC, and the BESS investment costs are higher than those of TES. Therefore, FPC and BESS are not included in the cost-effective optimal systems.
- The application of an optimization algorithm to determine optimal designs and operating strategies enables a well-founded comparison of the different SHS configurations and a detailed investigation of the synergies between the components. Without optimization, the complexity of the systems can lead to sub-optimal designs and operations, neglecting non-obvious synergies and effects.
- The incorporation of nonlinear models in the design and operational optimization is relevant for the respective SHS and the use case. Many synergies and operational effects arise from the nonlinear temperature-dependent behavior of the thermal components. Additionally, the detailed models allow a thorough investigation of the SHS, enabling us to clarify why certain component connections are advantageous and to derive sophisticated configurations for real-world applications.

Based on our findings, future studies should focus on the following points:

- The derivation and investigation of sophisticated SHS configurations for various use cases, e.g. industrial batch processes with varying heat demands and temperatures using optimization-based techno-economic assessment.
- The inclusion of life cycle emissions and future changes in emissions of the EG electricity mix into the techno-economic assessment.
- Further development of the proposed optimization algorithm to include AOE directly into the operational objective, to allow the use of higher model detail levels (e.g. transient effects in load point changes, pressure losses, auxiliary power demand) and to perform the optimization over a full year instead of representative periods.

CRediT authorship contribution statement

Matthias Loevenich: Writing – review & editing, Writing – original draft, Visualization, Validation, Software, Methodology, Investigation, Data curation, Conceptualization. **Martin Bähr:** Writing – review & editing, Writing – original draft, Methodology, Conceptualization. **Rushit Kansara:** Writing – review & editing, Writing – original draft, Software, Methodology, Investigation, Conceptualization. **Jürgen Dersch:** Writing – review & editing, Supervision, Conceptualization. **Robert Pitz-Paal:** Supervision.

Declaration of competing interest

The authors declare that they have no known competing financial interests or personal relationships that could have appeared to influence the work reported in this paper.

Acknowledgments

We would like to thank Diana Wenzke from DLR's Institute of Low-Carbon Industrial Processes for her continuous support and the fruitful discussions on the conceptualization of the study, optimization approach and results.

Appendix A. Model equations

This section contains the modeling equations describing the KPIs in Appendix A.1, the component's costs and operational performance in Appendix A.2, the system connections in Appendix A.3 and the reference system in Appendix A.4.

A.1. Key performance indicators

The following sections state the equations used to calculate the KPIs (TAC and AOE) that are for the design optimization of the SHS configurations.

Total annualized cost

The following cost calculations are defined based on [29]. TAC is the life cycle cost (LCC) of a project annualized with the capital recovery factor (CRF), which depends on the project lifetime N_{proj} and discount rate d_{proj}. The LCC includes capital expenditures ($CAPEX$), operational expenditures ($OPEX$), and replacement expenditures ($REPEX$) discounted with d_{proj} for each year of the project n_k. The latter relationship can be written as follows:

$$TAC = CRF \cdot LCC, \tag{A.1}$$

$$CRF = \frac{(1 + d_{\text{proj}})^{N_{\text{proj}}} \cdot d_{\text{proj}}}{(1 + d_{\text{proj}})^{N_{\text{proj}}} - 1}, \tag{A.2}$$

$$LCC = CAPEX + \sum_{k=1}^{N_{\text{proj}}} \frac{OPEX(n_k) + REPEX(n_k)}{(1 + d_{\text{proj}})^{n_k}}. \tag{A.3}$$

The $CAPEX$ contains all investment costs, including direct costs for the components themselves and indirect costs for additional equipment, engineering, procurement, construction services and contingencies, and is given as

$$\begin{aligned} CAPEX =& C_{\text{PV,inv}} + C_{\text{BESS,inv}} + (1 + r_{\text{ind,th}}) \cdot \\ & (C_{\text{STC,inv}} + C_{\text{HP,inv}} + C_{\text{TES,inv}} + C_{\text{HX,inv}}). \end{aligned} \tag{A.4}$$

Component cost items are defined in Appendix A.2. Cost items $C_{\text{PV,inv}}$ and $C_{\text{BESS,inv}}$ already include direct and indirect costs. By contrast, the costs for the thermal components STC, HP, TES, and HX cover only direct costs; therefore, we assume a surcharge of 30% for indirect costs with $r_{\text{ind,th}}$.

$OPEX$ describes annual operating expenses and is usually divided into a variable $OPEX_{\text{var}}$ and a fixed $OPEX_{\text{fix}}$ part. As only a single TOY is used for the techno-economic assessment, the $OPEX$ is identical in each year n_k and is thus defined by

$$OPEX(n_k) = OPEX_{\text{var}} + OPEX_{\text{fix}}. \tag{A.5}$$

Based on the operation of the SHS and the fact that the variable operating costs here only depend on the grid power consumed, $OPEX_{var}$ is a function of the power P_{EG} drawn from the EG and the corresponding time-dependent hourly electricity price $c_{\text{EG,var}}$ in each time grid point t_i of the TOY and is defined as

$$OPEX_{\text{var}} = \sum_{i=1}^{N_{\text{t}}} \Delta t \cdot P_{\text{EG}}(t_i) \cdot c_{\text{EG,var}}(t_i), \tag{A.6}$$

where N_{t} denotes the total number of time steps per TOY. The electricity price curve for the TOY is presented in Section 2.5. In contrast,

$OPEX_{fix}$ is defined as the sum of component-specific fixed operation and maintenance costs:

$$OPEX_{\text{fix}} = C_{\text{EG,fix}} + C_{\text{PV,op}} + C_{\text{BESS,op}} + C_{\text{STC,op}} + C_{\text{HP,op}} + C_{\text{TES,op}} + C_{\text{HX,op}}. \quad \text{(A.7)}$$

Component-specific fixed operating costs are given in Appendix A.2.

For $REPEX$ only the replacement of the BESS is considered because the lifetime of the other components meets or exceeds the project lifetime of 25 years selected in this study. We assume a BESS lifetime N_{BESS} of 10 years and replacement costs identical to the energy-specific BESS investments defined in (A.19), which must be included as $REPEX$ in (A.3) in the form

$$REPEX(n_k) = \begin{cases} C_{\text{BESS,es}} & \text{if } n_k \in \{j \cdot N_{\text{BESS}} \mid j \in \mathbb{N}\} \\ 0 & \text{else} \end{cases} \quad \text{(A.8)}$$

every N_{BESS} years.

Annual operating emissions

For the AOE, the only operating emissions that occur in the SHS investigated in this study are those related to the power P_{EG} drawn from the EG. These emissions depend on the electricity mix and are defined as an energy-specific global warming potential gwp_{EG}. Analogous to $OPEX_{\text{var}}$, the AOE of the SHS can therefore be formulated via

$$AOE = \sum_{i=1}^{N_t} \Delta t \cdot P_{\text{EG}}(t_i) \cdot gwp_{\text{EG}}(t_i). \quad \text{(A.9)}$$

Because we use a single TOY for the techno-economic assessment, it is assumed that the AOE are identical in each year n_k of the plant's operational life. The energy-specific electricity emission curve for the TOY is presented in Section 2.5.

A.2. Components

This section introduces the equations used to describe the operational performance of the components as well as the investment and operational costs depending on the component capacity.

Photovoltaic field

The PV field is scaled according to the total module area A_{PV}. To describe the capacity of the PV field, the nominal DC power output $P_{\text{PV,dc-nom}}$ is used. Under standard test conditions with an irradiation $I_{\text{PV,nom}}$ of 1000 W/m^2 and a nominal efficiency of the modules $\eta_{\text{PV,nom}}$ of 21.2% [68], it is defined as

$$P_{\text{PV,dc-nom}} = I_{\text{PV,nom}} \cdot A_{\text{PV}} \cdot \eta_{\text{PV,nom}}. \quad \text{(A.10)}$$

To determine the module efficiency, a parameter set for Si-Mono-type modules is used, as these dominate the market for utility-scale applications [34]. Depending on the nominal DC power, we define the investment costs $C_{\text{PV,inv}}$ and, relative to those, the annual operational expenditures $C_{\text{PV,op}}$ as follows:

$$C_{\text{PV,inv}} = P_{\text{PV,ref}} \cdot c_{\text{PV}} \cdot \left(\frac{P_{\text{PV,dc-nom}}}{P_{\text{PV,ref}}} \right)^{s_{\text{PV}}}, \quad \text{(A.11)}$$

$$C_{\text{PV,op}} = C_{\text{PV,inv}} \cdot r_{\text{PV,op}}. \quad \text{(A.12)}$$

To calculate the investment costs [69], the relative cost c_{PV} of 872.75 €/kW for a reference DC power $P_{\text{PV,ref}}$ of 100 000 kW and a scaling exponent s_{PV} of 0.91 are used. Operational expenditures are set in relation to the investment costs with an operational cost rate $r_{\text{PV,op}}$ of 2.5% [70].

Next, the nominal AC power $P_{\text{PV,ac-nom}}$ is defined, which depends on $P_{\text{PV,dc-nom}}$ and serves as an upper bound for the time-dependent AC power output of the field P_{PV} including the inverters. $P_{\text{PV,ac-nom}}$ depends on the number of inverters installed, and is usually lower than $P_{\text{PV,dc-nom}}$ calculated under standard test conditions. We use a DC-AC ratio $R_{\text{PV,dc-ac}}$ of 1.3, which is in the cost-optimal range for the sites investigated in this study [35], resulting in

$$P_{\text{PV,ac-nom}} = \frac{P_{\text{PV,dc-nom}}}{R_{\text{PV,dc-ac}}}. \quad \text{(A.13)}$$

The time-dependent AC power output P_{PV} is calculated as a function of the module area A_{PV}, the global tilted irradiance normal to the module surface I_{PV} and the module and inverter efficiencies $\eta_{\text{PV,mod}}$ and $\eta_{\text{PV,inver}}$ via

$$P_{\text{PV}}(t_i) = (1 - f_{\text{PV,cur}}(t_i)) \cdot A_{\text{PV}} \cdot I_{\text{PV}}(t_i) \cdot \eta_{\text{PV,mod}}(t_i) \cdot \eta_{\text{PV,inver}}. \quad \text{(A.14)}$$

At each time point, P_{PV} must be less than $P_{\text{PV,ac-nom}}$. Therefore, the available PV power can be curtailed by the curtailment factor $f_{\text{PV,cur}}$. The time-dependent solar irradiation I_{PV} is calculated for modules with a southern orientation and site-specific optimal tilt angle of 32° [71]. The irradiation I_{PV} used to calculate the PV power is the GTI on the module normal. The calculation depends on the current sun position, global horizontal irradiation (GHI), direct normal irradiation (DNI) and the module azimuth and tilt angles. I_{PV} is calculated for modules south-facing with a tilt angle of 32° and an albedo of 0.2 for a grass underground using the Perez method, as presented in [72]. Field availability, shading, and soiling effects are neglected. We assume a constant inverter efficiency $\eta_{\text{PV,inver}}$ of 95% [37]. The time-dependent module efficiency $\eta_{\text{PV,mod}}$ is calculated using a three-parameter model to capture the part-load behavior for different irradiation conditions I_{PV} and different ambient temperatures T_{amb} [36] using

$$\eta_{\text{PV,mod}}(t_i) = \left[\eta_{\text{PV,nom}} + \alpha_{\text{PV,1}} \cdot \ln\left(\frac{I_{\text{PV}}(t_i)}{I_{\text{PV,nom}}} \right) \right] \cdot \left[1 + \alpha_{\text{PV,2}} \cdot \left(T_{\text{amb}}(t_i) + \alpha_{\text{PV,3}} \cdot I_{\text{PV}}(t_i) - T_{\text{PV,nom}} \right) \right]. \quad \text{(A.15)}$$

The parameters $\alpha_{\text{PV,1}}, \alpha_{\text{PV,2}}, \alpha_{\text{PV,3}}$ and the nominal cell temperature $T_{\text{PV,nom}}$ are set to represent a Si-mono-type module [68].

Battery energy storage system

For the BESS we use a simple energy-based model with a round-trip efficiency η_{BESS} of 86%, representing lithium-ion storage with integrated inverters [38]. The state of charge (SOC) represents the energy content relative to the nominal energy capacity $E_{\text{BESS,nom}}$ with a minimum of 10% and a maximum of 90% for operating the BESS at a typical depth of discharge (DoD) of 80%. The charge and discharge powers at each time point $P_{\text{BESS,ch}}$ and $P_{\text{BESS,dis}}$ can be operated between zero and the nominal power capacity $P_{\text{BESS,nom}}$. The energy balance describing the SOC change for the BESS can therefore be written as

$$\frac{SOC(t_{i+1}) - SOC(t_i)}{\Delta t} \cdot E_{\text{BESS,nom}} = P_{\text{BESS,ch}}(t_i) \cdot \eta_{\text{BESS}} - P_{\text{BESS,dis}}(t_i). \quad \text{(A.16)}$$

Because the investment costs for BESS usually depend on $E_{\text{BESS,nom}}$ and $P_{\text{BESS,nom}}$, we define the investment cost C_{BESS} as the sum of the energy capacity-dependent cost item $C_{\text{BESS,es}}$ and power capacity-dependent cost item $C_{\text{BESS,ps}}$. The power-specific cost is calculated using the relative cost $c_{\text{BESS,ps}}$ of 297.35 €/kW for a reference power $P_{\text{BESS,ref}}$ of 100 000 kW and a scaling exponent $s_{\text{BESS,ps}}$ of 0.974 [70]. For the energy-specific cost, relative costs $c_{\text{BESS,es}}$ of 320.22 €/kWh for a reference capacity of 10 full load hours $h_{\text{BESS,ref}}$ at nominal power $P_{\text{BESS,nom}}$ and a scaling exponent $s_{\text{BESS,es}}$ of 0.9 [70] are used. Therefore, the investment costs are given by

$$C_{\text{BESS,inv}} = C_{\text{BESS,ps}} + C_{\text{BESS,es}}, \quad \text{(A.17)}$$

$$C_{\text{BESS,ps}} = P_{\text{BESS,ref}} \cdot c_{\text{BESS,ps}} \cdot \left(\frac{P_{\text{BESS,nom}}}{P_{\text{BESS,ref}}} \right)^{s_{\text{BESS,ps}}}, \quad \text{(A.18)}$$

$$C_{\text{BESS,es}} = h_{\text{BESS,ref}} \cdot P_{\text{BESS,nom}} \cdot c_{\text{BESS,es}} \cdot \left(\frac{E_{\text{BESS,nom}}}{h_{\text{BESS,ref}} \cdot P_{\text{BESS,nom}}} \right)^{s_{\text{BESS,es}}}. \quad \text{(A.19)}$$

The operational expenditures are set relative to the investment costs $C_{\mathrm{BESS,inv}}$ using an operational rate $r_{\mathrm{BESS,op}}$ of 2.5% [73]; that is,

$$C_{\mathrm{BESS,op}} = C_{\mathrm{BESS,inv}} \cdot r_{\mathrm{BESS,op}}. \tag{A.20}$$

Solar thermal collector field

In this study we investigate FPC and PTC collectors in different SHS configurations. The operational performance and costs for both collector types can be calculated using the following equations, but with different nominal values, loss coefficients, and cost parameters. The corresponding values for FPC and PTC are listed in Table B.7 and Table B.8, respectively.

The STC field is scaled according to the collector area A_{STC}. To obtain an estimation of the available solar heat as a function of A_{STC}, we define the nominal heat output $\dot{Q}_{\mathrm{STC,nom}}$ using a nominal irradiance $I_{\mathrm{STC,nom}}$ and a nominal efficiency $\eta_{\mathrm{STC,nom}}$

$$\dot{Q}_{\mathrm{STC,nom}} = A_{\mathrm{STC}} \cdot I_{\mathrm{STC,nom}} \cdot \eta_{\mathrm{STC,nom}}. \tag{A.21}$$

We model the STC performance following [29]. The calculation of the available irradiance on the receivers $\dot{q}\varepsilon_{\mathrm{STC,rec}}$ differs depending on the collector type:

The available irradiance on the FPC receiver pipes $\dot{q}\varepsilon_{\mathrm{FPC,rec}}$ depends on the direct and diffuse irradiance and is calculated according to [74]. The diffuse tilted irradiance (DTI) and incidence angle θ_{FPC} are calculated for south-facing collectors with a fixed tilt angle of 32°. For DTI, we use the Perez method [72] with an albedo of 0.2. The incidence angle modification is calculated to represent the collector defined in [39] with $\alpha_{\mathrm{FPC},1}$. The work [39] also defines the DTI influence, which is involved in $\alpha_{\mathrm{FPC},2}$. Again, we neglect the influences of field availability, soiling and shading, leading to the following definition for the available irradiation on the FPC receivers:

$$\begin{aligned}\dot{q}\varepsilon_{\mathrm{FPC,rec}}(t) = \eta_{\mathrm{FPC,opt}} \cdot \Bigg(& \mathrm{DNI}(t) \cdot \cos\left(\theta_{\mathrm{FPC}}(t)\right) \cdot \\ & \left[1 - \frac{(1-\alpha_{\mathrm{FPC},1})}{0.5557} \cdot \left(\frac{1}{\cos\left(\theta_{\mathrm{FPC}}(t)\right)} - 1\right)\right] \\ & + \mathrm{DTI}(t) \cdot \alpha_{\mathrm{FPC},2} \Bigg).\end{aligned} \tag{A.22}$$

Because PTCs concentrate the sunlight, only DNI can be used to produce heat. In addition to PV and FPC, the PTCs follow the position of the sun on one axis. We assume that the collectors are oriented north–south and therefore track in east–west direction. The corresponding incidence and tracking angles are calculated based on [29]. Neglecting the influences of field availability, soiling and shading, we calculate the available irradiance on the receiver pipes as a function of the DNI, the optical collector efficiency $\eta_{\mathrm{PTC,opt}}$ and the incidence angle θ_{PTC} as

$$\begin{aligned}\dot{q}\varepsilon_{\mathrm{PTC,rec}}(t) = \eta_{\mathrm{PTC,opt}} \cdot \mathrm{DNI}(t) \cdot \Big[& \cos\left(\theta_{\mathrm{PTC}}(t)\right) - \\ & \left(\alpha_{\mathrm{PTC},1} \cdot \theta_{\mathrm{PTC}}(t) + \alpha_{\mathrm{PTC},2} \cdot \theta^2_{\mathrm{PTC}}(t)\right) \Big].\end{aligned} \tag{A.23}$$

The factors $\alpha_{\mathrm{PTC},1}$ and $\alpha_{\mathrm{PTC},2}$ used to calculate the modification depending on the incidence angle are defined to represent the collector given in [40]. Independent of the collector type, the heat transferred from the receivers to the heat transfer fluid (HTF) is then defined as

$$\begin{aligned}\dot{m}_{\mathrm{STC}}(t_i) \cdot c_{\mathrm{p,oil}} \cdot \left(T_{\mathrm{STC,out}}(t_i) - T_{\mathrm{STC,in}}(t_i)\right) = A_{\mathrm{STC}} \cdot \\ \left(1 - f_{\mathrm{STC,cur}}(t_i)\right) \cdot \left(\dot{q}\varepsilon_{\mathrm{STC,rec}}(t_i) - \dot{q}\varepsilon_{\mathrm{STC,loss}}(t_i)\right).\end{aligned} \tag{A.24}$$

The heat input into the HTF, given on the left-hand side of (A.24), is defined by the mass flow through the STC field $\dot{m}_{\mathrm{STC}}$, specific heat capacity $c_{\mathrm{p,oil}}$ and temperature difference from the field inlet $T_{\mathrm{STC,in}}$ to field outlet $T_{\mathrm{STC,out}}$. The right-hand side of (A.24) describes the balance of the available irradiation on the receivers $\dot{q}\varepsilon_{\mathrm{STC,rec}}$ and the thermal losses $\dot{q}\varepsilon_{\mathrm{STC,loss}}$. Both are specific with respect to the collector area A_{STC} and depend on the curtailment factor $f_{\mathrm{STC,cur}}$, assuming that excess heat can be curtailed.

The thermal losses of the receivers $\dot{q}\varepsilon_{\mathrm{STC,loss}}$ are calculated depending on the temperature difference between the receivers and the ambient $\Delta T_{\mathrm{STC,amb}}$ using a polynomial fit function with the coefficients $\{\beta_{\mathrm{STC},0}, \ldots, \beta_{\mathrm{STC},4}\}$ via

$$\begin{aligned}\dot{q}\varepsilon_{\mathrm{STC,loss}} = \beta_{\mathrm{STC},0} \cdot \big(& \beta_{\mathrm{STC},1} \cdot \Delta T_{\mathrm{STC,amb}}(t_i) + \\ & \beta_{\mathrm{STC},2} \cdot \Delta T^2_{\mathrm{STC,amb}}(t_i) + \\ & \beta_{\mathrm{STC},3} \cdot \Delta T^3_{\mathrm{STC,amb}}(t_i) + \\ & \beta_{\mathrm{STC},4} \cdot \Delta T^4_{\mathrm{STC,amb}}(t_i) \big).\end{aligned} \tag{A.25}$$

Here, the temperature difference $\Delta T_{\mathrm{STC,amb}}$ between the receivers and the ambient is based on the arithmetic mean of the field temperature between inlet and outlet, given as

$$\Delta T_{\mathrm{STC,amb}}(t_i) = \frac{T_{\mathrm{STC,out}}(t_i) + T_{\mathrm{STC,in}}(t_i)}{2} - T_{\mathrm{amb}}(t_i). \tag{A.26}$$

The FPC and PTC investment costs $C_{\mathrm{STC,inv}}$ rely on the collector area A_{STC}, a reference collector area $A_{\mathrm{STC,ref}}$ and the corresponding relative costs c_{STC} as well as the cost exponent s_{STC} and are given in the form

$$C_{\mathrm{STC,inv}} = A_{\mathrm{STC,ref}} \cdot c_{\mathrm{STC}} \cdot \left(\frac{A_{\mathrm{STC}}}{A_{\mathrm{STC,ref}}}\right)^{s_{\mathrm{STC}}}. \tag{A.27}$$

Again, the operational expenditures $C_{\mathrm{STC,op}}$ are calculated relative to $C_{\mathrm{STC,inv}}$ with $r_{\mathrm{STC,op}}$ by

$$C_{\mathrm{STC,op}} = C_{\mathrm{STC,inv}} \cdot r_{\mathrm{STC,op}}. \tag{A.28}$$

Heat pump

To describe the HP performance, we use a model based on the Carnot efficiency [43]. The coefficient of performance (COP) for the heat supply on the sink side is defined as

$$COP_{\mathrm{HP,hot}}(t_i) = \eta_{\mathrm{HP}} \cdot \frac{T_{\mathrm{HP,hot\text{-}out}}(t_i)}{T_{\mathrm{HP,hot\text{-}out}}(t_i) - T_{\mathrm{HP,cold\text{-}in}}(t_i)}, \tag{A.29}$$

where $T_{\mathrm{HP,hot\text{-}out}}$ is the outlet temperature of the thermal oil heated via the high-temperature heat exchanger and $T_{\mathrm{HP,cold\text{-}in}}$ is the incoming heat source temperature on the air side of the low-temperature heat exchanger. The parameter η_{HP} represents the 2nd Law efficiency, which is used to relate the COP of the HP to the Carnot efficiency of the reverse Brayton cycle [43]. Here, η_{HP} is assumed to be 0.6, because this value is within the average range of commercially available HPs [75].

The HP thermal output on the sink side reads as

$$\begin{aligned}\dot{m}_{\mathrm{HP,hot}}(t_i) \cdot c_{\mathrm{p,oil}} \cdot \left(T_{\mathrm{HP,hot\text{-}out}}(t_i) - T_{\mathrm{HP,hot\text{-}in}}(t_i)\right) = \\ COP_{\mathrm{HP,hot}}(t_i) \cdot P_{\mathrm{HP}}(t_i),\end{aligned} \tag{A.30}$$

where P_{HP} denotes the electrical power input to the HP compressor. The maximum thermal output of the HP is limited by its nominal capacity $\dot{Q}_{\mathrm{HP,nom}}$:

$$\begin{aligned}\dot{m}_{\mathrm{HP,hot}}(t_i) \cdot c_{\mathrm{p,oil}} \cdot \left(T_{\mathrm{HP,hot\text{-}out}}(t_i) - T_{\mathrm{HP,hot\text{-}in}}(t_i)\right) \leq \\ \dot{Q}_{\mathrm{HP,nom}}.\end{aligned} \tag{A.31}$$

The HP thermal input on the source side is given by

$$\begin{aligned}\dot{m}_{\mathrm{HP,cold}}(t_i) \cdot c_{\mathrm{p,air}} \cdot \left(T_{\mathrm{HP,cold\text{-}in}}(t_i) - T_{\mathrm{HP,cold\text{-}out}}(t_i)\right) = \\ COP_{\mathrm{HP,cold}} \cdot P_{\mathrm{HP}}(t_i),\end{aligned} \tag{A.32}$$

$$COP_{\mathrm{HP,cold}} = COP_{\mathrm{HP,hot}} - 1 \tag{A.33}$$

The airflow of the heat source $\dot{m}_{\mathrm{HP,cold}}$ is cooled from $T_{\mathrm{HP,cold\text{-}in}}$ to $T_{\mathrm{HP,cold\text{-}out}}$ providing heat to the Brayton cycle. The COP on the heat source side, $COP_{\mathrm{HP,cold}}$, is one unit lower than $COP_{\mathrm{HP,hot}}$.

Depending on the nominal thermal output, the investment costs $C_{\mathrm{HP,inv}}$ and, relative to those, the annual operational expenditures $C_{\mathrm{HP,op}}$ read as

$$C_{\mathrm{HP,inv}} = \dot{Q}_{\mathrm{HP,ref}} \cdot c_{\mathrm{HP}} \cdot \left(\frac{\dot{Q}_{\mathrm{HP,nom}}}{\dot{Q}_{\mathrm{HP,ref}}}\right)^{s_{\mathrm{HP}}}, \tag{A.34}$$

$$C_{\mathrm{HP,op}} = C_{\mathrm{HP,inv}} \cdot r_{\mathrm{HP,op}}. \tag{A.35}$$

The relative costs c_{HP} of 552.55 €/kW for a reference thermal output $\dot{Q}_{\mathrm{HP,ref}}$ of 210 kW and a scaling exponent s_{HP} of 0.912 are used to calculate the investment costs [76], and the operational expenditures are set relative to the investment costs with an operational rate $r_{\mathrm{HP,op}}$ of 1% [77].

Thermal energy storage

According to [42], the TES is modeled using a lumped capacitance approach, assuming a spatially averaged temperature over the entire storage material. The TES nominal energy content $E_{\mathrm{TES,nom}}$ is defined as

$$E_{\mathrm{TES,nom}} = m_{\mathrm{TES}} \cdot c_{\mathrm{p,TES}} \cdot (T_{\mathrm{TES,max}} - T_{\mathrm{TES,min}}). \tag{A.36}$$

which depends on the specific heat capacity of the storage material $c_{\mathrm{p,TES}}$, the storage material mass m_{TES} and the available temperature range. We use a constant specific heat capacity of 1.099 kJ/(kgK) [78] and a temperature range of 160–360 °C [45], which corresponds to a concrete-based TES that is commercially available and easily scalable owing to its containerized construction. In our model, the mass of the storage material scales the TES. Since a uniform temperature is assumed across the storage material, the change in the TES state can be modeled with the following energy balance

$$\begin{aligned}&\eta_{\mathrm{TES}} \cdot \dot{m}_{\mathrm{TES,ch}}(t_i) \cdot c_{\mathrm{p,oil}} \cdot (T_{\mathrm{TES,ch\text{-}in}}(t_i) - T_{\mathrm{TES,ch\text{-}out}}(t_i)) - \\ &\quad \dot{m}_{\mathrm{TES,dis}}(t_i) \cdot c_{\mathrm{p,oil}} \cdot (T_{\mathrm{TES,dis\text{-}out}}(t_i) - T_{\mathrm{TES,dis\text{-}in}}(t_i)) \\ &\quad = m_{\mathrm{TES}} \cdot c_{\mathrm{p,TES}} \cdot \frac{T_{\mathrm{TES}}(t_{i+1}) - T_{\mathrm{TES}}(t_i)}{\Delta t},\end{aligned} \tag{A.37}$$

where η_{TES} represents a round-trip efficiency for charge and discharge. The charging outlet temperature $T_{\mathrm{TES,ch\text{-}out}}$ and discharging outlet temperature $T_{\mathrm{TES,dis\text{-}out}}$ are modeled based on a heat transfer effectiveness model derived by [42]. Therefore, we assume that the storage mass is sufficiently large to set the heat capacity of the working fluid as the limiting factor for the heat transfer and reduce the dependency of the effectiveness on temperature only. With this model, the charging and discharging outlet temperature are given by

$$\begin{aligned}T_{\mathrm{TES,ch\text{-}out}}(t_i) = &T_{\mathrm{TES,ch\text{-}in}}(t_i) - \\ &\varepsilon_{\mathrm{TES,ch}} \cdot (T_{\mathrm{TES,ch\text{-}in}}(t_i) - T_{\mathrm{TES}}(t_i)),\end{aligned} \tag{A.38}$$

$$\begin{aligned}T_{\mathrm{TES,dis\text{-}out}}(t_i) = &T_{\mathrm{TES,dis\text{-}in}}(t_i) - \\ &\varepsilon_{\mathrm{TES,dis}} \cdot (T_{\mathrm{TES,dis\text{-}in}}(t_i) - T_{\mathrm{TES}}(t_i)).\end{aligned} \tag{A.39}$$

The charging $\varepsilon_{\mathrm{TES,ch}}$ and discharging $\varepsilon_{\mathrm{TES,dis}}$ effectiveness values are set to 0.9 according to [42]. Depending on the nominal energy content, the investment costs $C_{\mathrm{TES,inv}}$ and, relative to those, the annual operational expenditures $C_{\mathrm{TES,op}}$ are defined as

$$C_{\mathrm{TES,inv}} = E_{\mathrm{TES,ref}} \cdot c_{\mathrm{TES}} \cdot \left(\frac{E_{\mathrm{TES,nom}}}{E_{\mathrm{TES,ref}}} \right)^{s_{\mathrm{TES}}}, \tag{A.40}$$

$$C_{\mathrm{TES,op}} = C_{\mathrm{TES,inv}} \cdot r_{\mathrm{TES,op}}. \tag{A.41}$$

We calculate the investment costs based on [79], using a relative cost c_{TES} of 21.03 €/kWh for a reference energy content $E_{\mathrm{TES,ref}}$ of 1 000 000 kWh and a scaling exponent s_{TES} of 0.9. Operational expenditures are set relative to $C_{\mathrm{TES,inv}}$ using an assumed operational rate $r_{\mathrm{TES,op}}$ of 1.5%.

Heat exchanger

We apply the effectiveness-NTU method [46] to model the design and performance of the oil-to-air HX. Because PTC and HP can reach temperatures significantly higher than the required DR inlet temperature of 200 °C, the HX is designed to achieve a nominal coarseness $\Delta T_{\mathrm{HX,nom}}$ of 20 °C at a moderate oil flow rate $\dot{m}_{\mathrm{HX,nom}}$ of 15 kg/s. Assuming a counterflow design and an overall heat transfer coefficient U_{HX} of 20 W/(m^2 K) [80] for oil to air heat transfer, this corresponds to a nominal effectiveness $\varepsilon_{\mathrm{HX,nom}}$ of 0.9, number of transfer units NTU_{HX} of 3.33 and heat transfer area A_{HX} of 2500 m^2. Depending on this heat transfer area A_{HX}, the investment costs $C_{\mathrm{HX,inv}}$ and, in relation to this, the annual operational expenditures $C_{\mathrm{HX,op}}$ are defined as

$$C_{\mathrm{HX,inv}} = A_{\mathrm{HX,ref}} \cdot c_{\mathrm{HX}} \cdot \left(\frac{A_{\mathrm{HX}}}{A_{\mathrm{HX,ref}}} \right)^{s_{\mathrm{HX}}}, \tag{A.42}$$

$$C_{\mathrm{HX,op}} = C_{\mathrm{HX,inv}} \cdot r_{\mathrm{HX,op}}. \tag{A.43}$$

The relative costs c_{HX} of 385.26 €/m^2 for a reference heat transfer area $A_{\mathrm{HX,ref}}$ of 200 m^2 are used to calculate the investment costs [81] together with a scaling exponent s_{HX} of 0.59 [82]. Operational expenditures are set relative to the investment costs, assuming a rate of $r_{\mathrm{HX,op}}$ of 1.5%.

To estimate the HX performance, the energy balance

$$\begin{aligned}&\dot{m}_{\mathrm{HX,oil}}(t_i) \cdot c_{\mathrm{p,oil}} \cdot (T_{\mathrm{HX,oil\text{-}in}}(t_i) - T_{\mathrm{HX,oil\text{-}out}}(t_i)) = \\ &\dot{m}_{\mathrm{HX,air}}(t_i) \cdot c_{\mathrm{p,air}} \cdot \left(T_{\mathrm{HX,air\text{-}out}}(t_i) - T_{\mathrm{HX,air\text{-}in}}(t_i)\right)\end{aligned} \tag{A.44}$$

must hold, with the mass flow rate $\dot{m}_{\mathrm{HX,oil/air}}$, the specific heat capacity $c_{\mathrm{p,oil/air}}$, and the inlet $T_{\mathrm{HX,oil/air\text{-}in}}$ as well as outlet $T_{\mathrm{HX,oil/air\text{-}out}}$ temperatures of the respective oil and air sides.

In addition, the definition of the effectiveness $\varepsilon_{\mathrm{HX}}$ of a counterflow layout is exploited to relate the inlet and outlet temperatures to the HX design. Knowing that the air flow is always the cold flow and always has the minimum heat transfer rate, while the oil flow is always the hot flow and has the maximum heat transfer rate, we can define the heat transfer ratio R_{HX} and the effectiveness $\varepsilon_{\mathrm{HX}}$ as follows

$$R_{\mathrm{HX}} = \frac{\dot{m}_{\mathrm{HX,air}} \cdot c_{\mathrm{p,air}}}{\dot{m}_{\mathrm{HX,oil}} \cdot c_{\mathrm{p,oil}}}, \tag{A.45}$$

$$\varepsilon_{\mathrm{HX}} = \frac{1 - \exp\left(-NTU_{\mathrm{HX}} \cdot (1 - R_{\mathrm{HX}})\right)}{1 - R_{\mathrm{HX}} \cdot \exp\left(-NTU_{\mathrm{HX}} \cdot (1 - R_{\mathrm{HX}})\right)}. \tag{A.46}$$

This means that the oil inlet temperature $T_{\mathrm{HX,oil\text{-}in}}$ can be calculated depending only on the effectiveness $\varepsilon_{\mathrm{HX}}$ and the air-side temperatures $T_{\mathrm{HX,air\text{-}in}}$ and $T_{\mathrm{HX,air\text{-}out}}$ using

$$\begin{aligned}&T_{\mathrm{HX,air\text{-}out}}(t_i) - T_{\mathrm{HX,air\text{-}in}}(t_i) = \\ &\varepsilon_{\mathrm{HX}} \cdot (T_{\mathrm{HX,oil\text{-}in}}(t_i) - T_{\mathrm{HX,air\text{-}in}}(t_i)).\end{aligned} \tag{A.47}$$

Electricity grid

For the EG we consider only operating expenditures. The EG prices shown in Section 2.5 are the market prices. For the calculation of the operational expenditures in (A.6) we calculate the variable price $c_{\mathrm{EG,var}}$ as a sum of the market prices c_{EG} and a constant surcharge $c_{\mathrm{EG,add}}$ for grid operation, taxes and levies

$$c_{\mathrm{EG,var}}(t_i) = c_{\mathrm{EG}}(t_i) + c_{\mathrm{EG,add}}. \tag{A.48}$$

In addition, for the calculation of the fixed operational expenditures in (A.7) we consider a fixed power price $c_{\mathrm{EG,fix}}$ relative to the peak rated power $P_{\mathrm{EG,nom}}$ drawn from the grid, leading to the fixed operating expenditures of the EG $C_{\mathrm{EG,fix}}$:

$$C_{\mathrm{EG,fix}} = P_{\mathrm{EG,nom}} \cdot c_{\mathrm{EG,fix}} \tag{A.49}$$

$P_{\mathrm{EG,nom}}$ also functions as an upper bound for the power drawn from the grid $P_{\mathrm{EG}}(t_i)$ in each time point t_i.

A.3. System constraints

This section provides an example of how the interconnections between the components are modeled by adding additional system constraints to the component models using configuration (a). The configuration is shown in more detail in Fig. A.10.

Starting with the electric supply, (A.14) and (A.16) define the PV and BESS power flows, respectively. In addition, we assume the

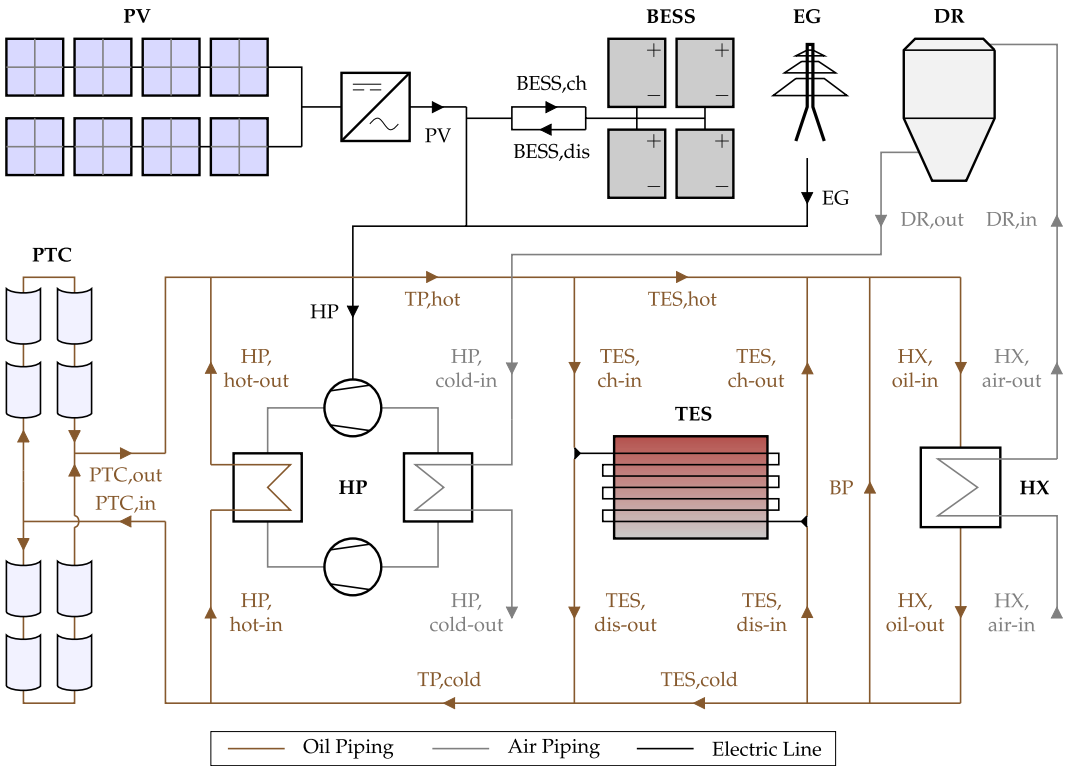

Fig. A.10. Schematic representation of SHS configuration (a) including photovoltaics (PV), battery energy storage (BESS), electricity grid (EG), parabolic trough collectors (PTC), high-temperature heat pump (HP), thermal energy storage (TES) and heat exchanger (HX) to supply the dryer (DR), with detailed flow notation.

following complementarity condition to prevent simultaneous charge and discharge of the BESS

$$P_{\mathrm{BESS,ch}}(t_i) \cdot P_{\mathrm{BESS,dis}}(t_i) = 0. \tag{A.50}$$

The power flow that supplies the HP can be represented as the sum of PV, BESS and EG power

$$P_{\mathrm{HP}}(t_i) = P_{\mathrm{PV}}(t_i) + P_{\mathrm{BESS,dis}}(t_i) - P_{\mathrm{BESS,ch}}(t_i) + P_{\mathrm{EG}}(t_i). \tag{A.51}$$

We set $P_{\mathrm{EG}} \geq 0$ as the disabled grid feed-in. To connect the air flow from the HX to the DR and to the HP cold side, the following conditions must hold

$$\dot{m}_{\mathrm{HX,air}}(t_i) = \dot{m}_{\mathrm{HP,cold}}(t_i) = \dot{m}_{\mathrm{DR}}, \tag{A.52}$$

$$T_{\mathrm{HX,air\text{-}in}}(t_i) = T_{\mathrm{amb}}(t_i), \tag{A.53}$$

$$T_{\mathrm{HX,air\text{-}out}}(t_i) = T_{\mathrm{DR,in}}, \tag{A.54}$$

$$T_{\mathrm{HP,cold\text{-}in}}(t_i) = T_{\mathrm{DR,out}}, \tag{A.55}$$

considering that $\dot{m}_{\mathrm{DR}}$, $T_{\mathrm{DR,in}}$ and $T_{\mathrm{DR,out}}$ are constant, according to the underlying use case. The cold-side outlet temperature of HP is defined by (A.32).

To describe the oil cycle, we begin the description at the HX oil outlet and define the connections until the cycle is closed at the HX oil inlet. The mass flows and temperatures for the TES cold side are given by

$$\dot{m}_{\mathrm{TES,cold}}(t_i) = \dot{m}_{\mathrm{HX,oil\text{-}out}}(t_i) - \dot{m}_{\mathrm{BP}}(t_i) - \dot{m}_{\mathrm{TES,dis}}(t_i), \tag{A.56}$$

$$T_{\mathrm{BP}}(t_i) = T_{\mathrm{TES,dis\text{-}in}}(t_i) = T_{\mathrm{TES,cold}}(t_i) = T_{\mathrm{HX,oil\text{-}out}}(t_i). \tag{A.57}$$

Using mass and energy balances, the TP cold side yields

$$\dot{m}_{\mathrm{TP,cold}}(t_i) = \dot{m}_{\mathrm{TES,dis}}(t_i) + \dot{m}_{\mathrm{TES,cold}}(t_i), \tag{A.58}$$

$$\dot{m}_{\mathrm{TP,cold}}(t_i) \cdot T_{\mathrm{TP,cold}}(t_i) = \dot{m}_{\mathrm{TES,dis}}(t_i) \cdot T_{\mathrm{TES,dis\text{-}out}}(t_i) + \dot{m}_{\mathrm{TES,cold}}(t_i) \cdot T_{\mathrm{TES,cold}}(t_i), \tag{A.59}$$

where the TES discharge outlet temperature is determined using (A.39). The inlet temperatures for the TPs are equal to those of the TP cold side temperature and the mass flows are connected via a mass balance

$$\dot{m}_{\mathrm{TP,cold}}(t_i) = \dot{m}_{\mathrm{PTC}}(t_i) + \dot{m}_{\mathrm{HP,hot}}(t_i), \tag{A.60}$$

$$T_{\mathrm{PTC.in}}(t_i) = T_{\mathrm{HP,hot\text{-}in}}(t_i) = T_{\mathrm{TP,cold}}(t_i). \tag{A.61}$$

The PTC and HP outlet temperatures are given by (A.24) and (A.30), respectively, whereas the HP outlet heat flow is restricted by (A.31). The TP hot side is connected to the separate producers using the mass and energy balance

$$\dot{m}_{\mathrm{TP,hot}}(t_i) = \dot{m}_{\mathrm{PTC}}(t_i) + \dot{m}_{\mathrm{HP,hot}}(t_i), \tag{A.62}$$

$$\dot{m}_{\mathrm{TP,hot}}(t_i) \cdot T_{\mathrm{TP,hot}}(t_i) = \dot{m}_{\mathrm{PTC}}(t_i) \cdot T_{\mathrm{PTC,out}}(t_i) + \dot{m}_{\mathrm{HP,hot}}(t_i) \cdot T_{\mathrm{HP,hot\text{-}out}}(t_i), \tag{A.63}$$

with the assumption of constant specific heat capacities. Analogously, we define a mass balance for the TES hot side and set the corresponding temperatures to the TP hot temperature

$$\dot{m}_{\mathrm{TES,hot}}(t_i) = \dot{m}_{\mathrm{TES,ch}}(t_i) - \dot{m}_{\mathrm{TP,hot}}(t_i), \tag{A.64}$$

$$T_{\mathrm{TES,ch\text{-}in}}(t_i) = T_{\mathrm{TES,hot}}(t_i) = T_{\mathrm{TP,hot}}(t_i). \tag{A.65}$$

The new TES temperature at time point t_{i+1} and TES charge outlet temperature are calculated according to (A.37) and (A.38). To guarantee that the TES is never charged and discharged at the same time, another complementarity condition is added

$$\dot{m}_{\mathrm{TES,ch}}(t_i) \cdot \dot{m}_{\mathrm{TES,dis}}(t_i) = 0. \tag{A.66}$$

Finally, the HX oil inlet is determined by means of mass and energy balance via the TES hot side as well as the BP with

$$\dot{m}_{\mathrm{HX,oil}}(t_i) = \dot{m}_{\mathrm{TES,hot}}(t_i) + \dot{m}_{\mathrm{TES,ch}}(t_i) + \dot{m}_{\mathrm{BP}}(t_i) \tag{A.67}$$

$$\dot{m}_{\mathrm{HX,oil}}(t_i) \cdot T_{\mathrm{HX,oil\text{-}in}}(t_i) = \dot{m}_{\mathrm{TES,hot}}(t_i) \cdot T_{\mathrm{TES,hot}}(t_i)$$

Table B.2
Table of system parameters used.

Variable	Value	Unit	Source
Δt	3600	s	–
N_t	8760	–	–
d_{proj}	5	%	[69]
N_{proj}	25	a	[69]
$r_{ind,th}$	0.3	–	–
$T_{amb,nom}$	15	°C	–

$$+ \dot{m}_{TES,ch}(t_i) \cdot T_{TES,ch\text{-}out}(t_i)$$
$$+ \dot{m}_{BP}(t_i) \cdot T_{BP}(t_i). \quad (A.68)$$

The oil and air cycles are connected via the HX definitions (A.44) and (A.47), completing the set of equations that define the operation of SHS configuration (a).

A.4. Reference system

This section contains the equations and boundary conditions used to calculate the TAC and AOE for a reference solution using a fossil gas burner instead of the SHS. To this end, we set a nominal GB capacity $\dot{Q}_{GB,nom}$ of 3.1 MW to cover the peak demand. The investment costs $C_{GB,inv}$ are calculated following [83] with the nominal capacity $\dot{Q}_{GB,nom}$, the reference size $\dot{Q}_{GB,ref}$ of 20 MW, the corresponding relative costs c_{GB} of 136.42 €/kW and cost exponent s_{GB} of 0.83:

$$C_{GB,inv} = \dot{Q}_{GB,ref} \cdot c_{GB} \cdot \left(\frac{\dot{Q}_{GB,nom}}{\dot{Q}_{GB,ref}} \right)^{s_{GB}}. \quad (A.69)$$

We use a constant efficiency η_{GB} of 88% [84] with regard to the condensed calorific value to calculate the necessary annual gas amount E_{GB}:

$$\sum_{i=1}^{N_t} \frac{\Delta t \cdot \dot{m}_{HX,air}(t_i) \cdot c_{p,air} \cdot \left(T_{HX,air\text{-}out}(t_i) - T_{HX,air\text{-}in}(t_i) \right)}{\eta_{GB}}$$
$$= E_{GB}. \quad (A.70)$$

Thus, we can calculate the operational expenditures for the GB using a fixed value relative to the investment costs with a rate of $r_{GB,op}$ of 3% [83] and a variable value depending on a constant average gas price for the year 2023 in Germany $c_{GB,var}$ of 84 €/MWh [85], referred to the condensed calorific value:

$$C_{GB,op} = C_{GB,inv} \cdot r_{GB,op} + E_{GB} \cdot c_{GB,var}. \quad (A.71)$$

Then we can define the $CAPEX$ for the reference fossil burner system as

$$CAPEX = (1 + r_{ind,th}) \cdot (C_{GB,inv} + C_{HX,inv}), \quad (A.72)$$

and the $OPEX$ as

$$OPEX = C_{GB,op} + C_{HX,op}. \quad (A.73)$$

Based on the latter equations, the TAC of the GB can be calculated using (A.1)–(A.3).

The AOE for the GB can be calculated using the global warming potential of gas gwp_{GB}, which is 181 kg/MWh for Germany [86], again referred to the condensed calorific value:

$$AOE = E_{GB} \cdot gwp_{GB} \quad (A.74)$$

Appendix B. Model parameters

This section provides a full set of all parameters used in this work, listed in Tables B.2–B.13.

Table B.3
Table of fluid parameters used.

Variable	Value	Unit	Source
$\dot{m}_{oil,max}$	45	kg/s	–
$c_{p,oil}$	2.1344	kJ/(kg K)	[87] @ 220 °C
$T_{oil,min}$	50	°C	[87]
$T_{oil,max}$	400	°C	[87]
$c_{p,air}$	1.01	kJ/(kg K)	[88] @ 100 °C
$T_{air,min}$	−20	°C	–
$T_{air,max}$	200	°C	–

Table B.4
Table of EG parameters used.

Variable	Value	Unit	Source
$P_{EG,max}$	[0, 6000]	kW	–
$c_{EG,add}$	33.94	€/MWh	[89]
$c_{EG,fix}$	199.61	€/(kW a)	[89]

Table B.5
Table of PV parameters used.

Variable	Value	Unit	Source
A_{PV}	[0, 30 000]	m^2	–
$I_{PV,nom}$	1000	W/m^2	–
$\eta_{PV,nom}$	0.212	–	[68]
$\alpha_{PV,1}$	0.06408	–	[68]
$\alpha_{PV,2}$	−0.0035	–	[68]
$\alpha_{PV,3}$	0.0275	K m^2/W	[68]
$T_{PV,nom}$	42	°C	[68]
$\eta_{PV,inver}$	0.95	–	[37]
$\theta_{PV,\ tilt}$	32	°	[71]
$R_{PV,dc\text{-}ac}$	1.3	–	[35]
c_{PV}	872.75	€/kW_{DC}	[69]
$P_{PV,ref}$	100 000	kW_{DC}	[69]
s_{PV}	0.91	–	[69]
$r_{PV,op}$	0.025	–	[70]

Table B.6
Table of BESS parameters used.

Variable	Value	Unit	Source
$E_{BESS,nom}$	[0, 20 000]	kWh	–
$P_{BESS,nom}$	[0, 3000]	kW	–
DoD	0.8	–	[38]
η_{BESS}	0.86	–	[38]
N_{BESS}	10	a	[38]
$c_{BESS,es}$	320.22	€/kWh	[70]
$h_{BESS,ref}$	10	h	[70]
$s_{BESS,es}$	0.9	–	[70]
$c_{BESS,ps}$	297.35	€/kW	[70]
$h_{BESS,ref}$	10	h	[70]
$s_{BESS,ps}$	0.974	–	[70]
$r_{BESS,op}$	0.025	–	[73]

Appendix C. Algorithm validation

In this section, we elaborate on the clustering method and the single-shot IPOPT approach with a well-chosen starting point.

C.1. Clustering

To evaluate the clustering approach in terms of solution quality, configuration (a) with PTC and HP in parallel and TES in series is also optimized without clustering the input data. This means that the system operation is optimized over an entire year by solving 365 optimization problems over 48 h using the rolling-horizon approach presented in Section 2.6.2 for each design point. Therefore, the circular conditions only apply at the beginning of the first and the end of the last day of the year. Fig. C.11 shows the optimization results of both the optimization with clustered input data (marked as circles) and with annual input

Table B.7
Table of FPC parameters used.

Variable	Value	Unit	Source
A_{FPC}	[0, 30 000]	m^2	–
$I_{FPC,nom}$	1000	W/m^2	–
$\eta_{FPC,nom}$	0.6	–	Calculated
$\eta_{FPC,opt}$	0.715	–	[39]
$\alpha_{FPC,1}$	0.97	–	[39]
$\alpha_{FPC,2}$	0.95	–	[39]
$\beta_{FPC,0}$	1.1	–	[39]
$\beta_{FPC,1}$	3.31	$W/(m^2\ K)$	[39]
$\beta_{FPC,2}$	0.011	$W/(m^2\ K^2)$	[39]
$\beta_{FPC,3}$	0	$W/(m^2\ K^3)$	[39]
$\beta_{FPC,4}$	0	$W/(m^2\ K^4)$	[39]
$T_{FPC,out-max}$	230	°C	[39]
c_{FPC}	449.28	€/m^2	[90]
$A_{FPC,ref}$	157 000	m^2	[90]
s_{FPC}	0.75	–	[90]
$r_{FPC,op}$	0.02	–	[90]

Table B.8
Table of PTC parameters used.

Variable	Value	Unit	Source
A_{PTC}	[0, 30 000]	m^2	–
$I_{PTC,nom}$	800	W/m^2	–
$\eta_{PTC,nom}$	0.7	–	Calculated
$\eta_{PTC,opt}$	0.75	–	[40]
$\alpha_{PTC,1}$	5.25e−4	1/°	[40]
$\alpha_{PTC,2}$	2.86e−5	$(1/°)^2$	[40]
$\beta_{PTC,0}$	1.1	–	[40]
$\beta_{PTC,1}$	0.3298	$W/(m^2\ K)$	[40]
$\beta_{PTC,2}$	0	$W/(m^2\ K^2)$	[40]
$\beta_{PTC,3}$	0	$W/(m^2\ K^3)$	[40]
$\beta_{PTC,4}$	1.356e−9	$W/(m^2\ K^4)$	[40]
$T_{PTC,out-max}$	400	°C	[40]
c_{PTC}	251.42	€/m^2	[91]
$A_{PTC,ref}$	987 920	m^2	[91]
s_{PTC}	0.9	–	[29]
$r_{PTC,op}$	0.015	–	[92]

Table B.9
Table of HP parameters used.

Variable	Value	Unit	Source
$\dot{Q}_{HP,nom}$	[0, 6000]	kW	–
η_{HP}	0.6	–	[75]
$T_{HP,hot-min}$	90	°C	[42]
$T_{HP,hot-max}$	250	°C	[42]
$T_{HP,cold-min}$	−20	°C	[42]
$T_{HP,cold-max}$	80	°C	[42]
c_{HP}	552.55	€/kW_{th}	[76]
$\dot{Q}_{HP,ref}$	210	kW	[76]
s_{HP}	0.912	–	[76]
$r_{HP,op}$	0.01	–	[77]

Table B.10
Table of TES parameters used.

Variable	Value	Unit	Source
m_{TES}	[0, 1000]	t	–
$c_{p,TES}$	1.099	kJ/(kgK)	[78] @ 250 °C
$T_{TES,min}$	160	°C	[45]
$T_{TES,max}$	360	°C	[45]
$\epsilon_{TES,ch}$	0.9	–	[42]
$\epsilon_{TES,dis}$	0.9	–	[42]
η_{TES}	0.95	–	[93]
c_{TES}	21.03	€/kWh	[79]
$E_{TES,ref}$	1 000 000	kWh	[79]
s_{TES}	0.9	–	Assumption
$r_{TES,op}$	0.015	–	Assumption

data (marked as crosses) for all three sites. It is obvious that the overall deviation is relatively small, especially for Hamburg and Würzburg, and

Table B.11
Table of HX parameters used.

Variable	Value	Unit	Source
$\Delta T_{HX,nom}$	20	°C	–
$\dot{m}_{HX,oil-nom}$	15	kg/s	–
$\epsilon_{HX,nom}$	0.9	–	Calculated
NTU_{HX}	3.33	–	Calculated
A_{HX}	2500	m^2	calculated
U_{HX}	0.02	$kW/(m^2\ K)$	[80]
c_{HX}	385.26	€/m^2	[81]
$A_{HX,ref}$	200	m^2	[81]
s_{HX}	0.59	–	[82]
$r_{HX,op}$	0.015	–	Assumption

Table B.12
Table of DR parameters used.

Variable	Value	Unit	Source
$T_{DR,in}$	200	°C	[28]
$T_{DR,out}$	80	°C	[28]
$\dot{m}_{DR}$	14.85	kg/s	[28]

Table B.13
Table of GB parameters used.

Variable	Value	Unit	Source
$\dot{Q}_{GB,nom}$	3100	MW	–
η_{GB}	0.88	–	[84]
c_{GB}	136.42	€/kW	[83]
$\dot{Q}_{GB,ref}$	20 000	kW	[83]
s_{GB}	0.83	–	[83]
$r_{GB,op}$	0.03	–	[83]
$c_{GB,var}$	84	€/MWh	[85]
gwp_{GB}	181	kg/MWh	[86]

that the deviation increases towards the minimal AOE values, where the design variables are close to their upper bounds and the solar resource is more dominant for all sites.

C.2. Single-shot approach

To run IPOPT using a single-shot approach, knowledge about the system is used to generate well-chosen starting points that are only partially random. To do so, we create static starting points with a value that is constant over the whole 48 h horizon for each variable. The static values for each variable are determined using system knowledge:

- For all operational variables that need initial values, in particular the TES concrete temperature and the BESS state of charge, we use these initial values for the starting point.
- For the HX oil inlet temperature, we set a nominal value depending on the known HX air outlet temperature and the nominal temperature difference over the HX.
- For all other temperatures, we use the maximum or minimum possible value depending on the position in the system, e.g. for the PTC inlet and outlet temperature, the minimum oil temperature and maximum PTC outlet temperature, respectively.
- Zero values are used for the curtailment factors of PV and STC, meaning no curtailment is assumed.
- All mass and power flows are set to a single randomly generated value, except the EG power, which is set to zero.

If infeasible solutions occur during operational optimization, we repeat the process of generating the starting point and running IPOPT until a feasible solution is obtained. However, if no feasible solution can be obtained in ten iterations, we declare the operating problem and the corresponding design point to be infeasible. This means that the design is not suitable to supply the heat demand.

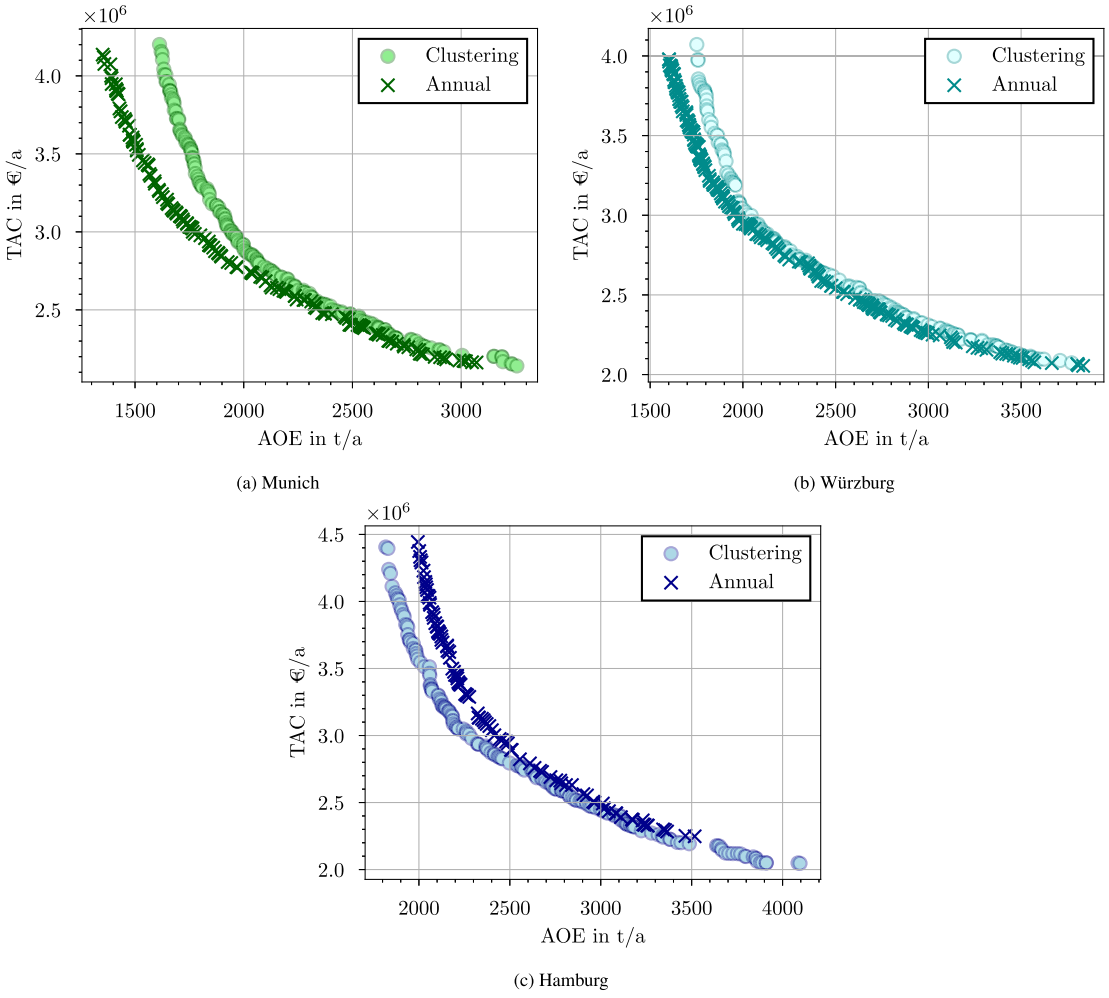

Fig. C.11. Pareto-optimal TAC over AOE calculated with and without clustering of the time series input data for the sites (a) Munich, (b) Würzburg and (c) Hamburg.

To validate the proposed single-shot approach in terms of solution quality, we use the optimal design points obtained for configuration (a) and evaluate the KPIs using the clustered input data with a rolling horizon, but run IPOPT with $N_s = 10$ random starting points. Fig. C.12 shows the optimal design points with respect to TAC and AOE for the sites Hamburg, Würzburg and Munich, which we determined using the same design points with the single-shot approach (marked as cross) and the multi-start approach with 10 randomly generated starting points (marked as circles). Remarkably, the single-shot approach leads to almost the same Pareto-optimal designs as the multi-start approach for the application considered.

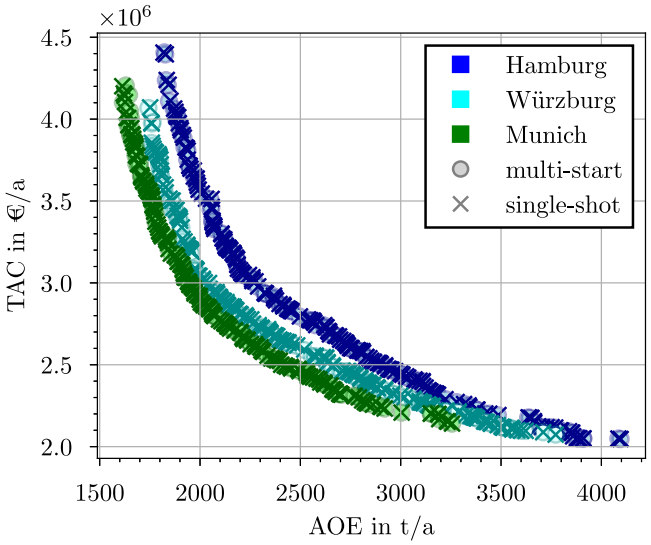

Fig. C.12. Pareto-optimal TAC over AOE calculated with single-shot approach using a well-chosen starting point and with multi-start approach using 10 randomly generated starting points.

Appendix D. Additional results

This section presents additional design and operational results for the SHS configurations (b) with PTC and HP in parallel and TES in series and (c) with PTC and HP in series and TES in series at the Würzburg site.

Fig. D.13 shows the optimal component capacities and the corresponding Pareto-optimal TAC over AOE for configuration (b), while Fig. D.14 illustrates the optimization results for configuration (c). The component capacities of the design corresponding to the optimal operating strategy shown in Fig. D.15 with a cost-competitive TAC of 2.48 Mio. €/a for SHS configuration (b) are as follows: $P_{\mathrm{EG,max}} = 1.61\,\mathrm{MW}$, $P_{\mathrm{PV,dc\text{-}nom}} = 5.66\,\mathrm{MW}$, $E_{\mathrm{BESS,nom}} = 4.48\,\mathrm{MWh}$, $P_{\mathrm{BESS,nom}} = 0.78\,\mathrm{MW}$, $\dot{Q}_{\mathrm{HP,nom}} = 3.31\,\mathrm{MW}$, $\dot{Q}_{\mathrm{PTC,nom}} = 0.86\,\mathrm{MW}$ and $E_{\mathrm{TES,nom}} =$

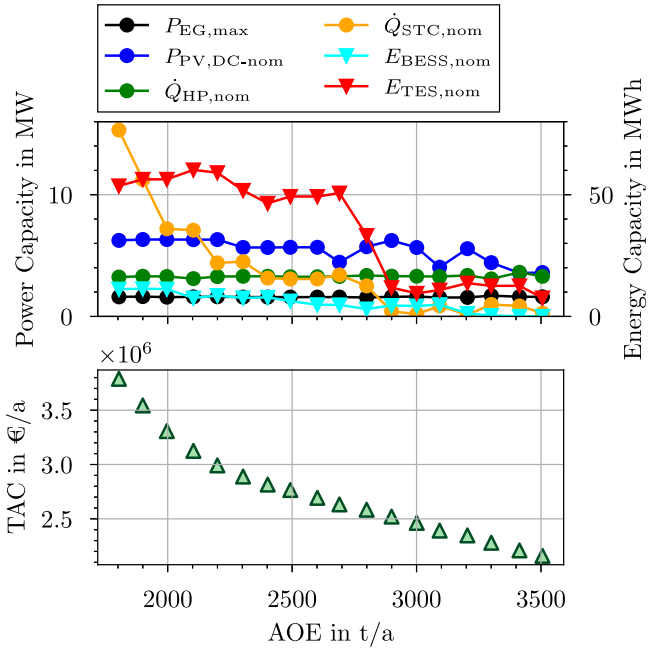

Fig. D.13. Optimal component capacities and corresponding Pareto-optimal TAC over AOE for configuration (b) with PTC and HP in parallel and TES in series at site Würzburg.

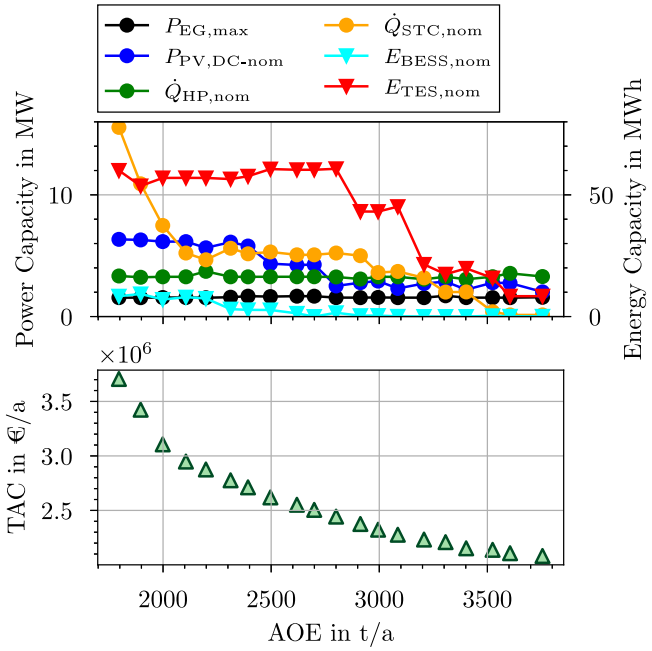

Fig. D.14. Optimal component capacities and corresponding Pareto-optimal TAC over AOE for configuration (c) with PTC and HP in series and TES in series at site Würzburg.

10.83 MWh. Analogously, the component capacities of the design corresponding to the optimal operating strategy presented in Fig. D.16 with a cost-competitive TAC of 2.48 Mio. €/a for SHS configuration (c) are given as follows: $P_{EG,max} = 1.56$ MW, $P_{PV,dc\text{-}nom} = 3.63$ MW, $E_{BESS,nom} = 0.36$ MWh, $P_{BESS,nom} = 2.81$ MWh, $\dot{Q}_{HP,nom} = 3.64$ MW, $\dot{Q}_{PTC,nom} = 5.31$ MW, $E_{TES,nom} = 56.92$ MWh.

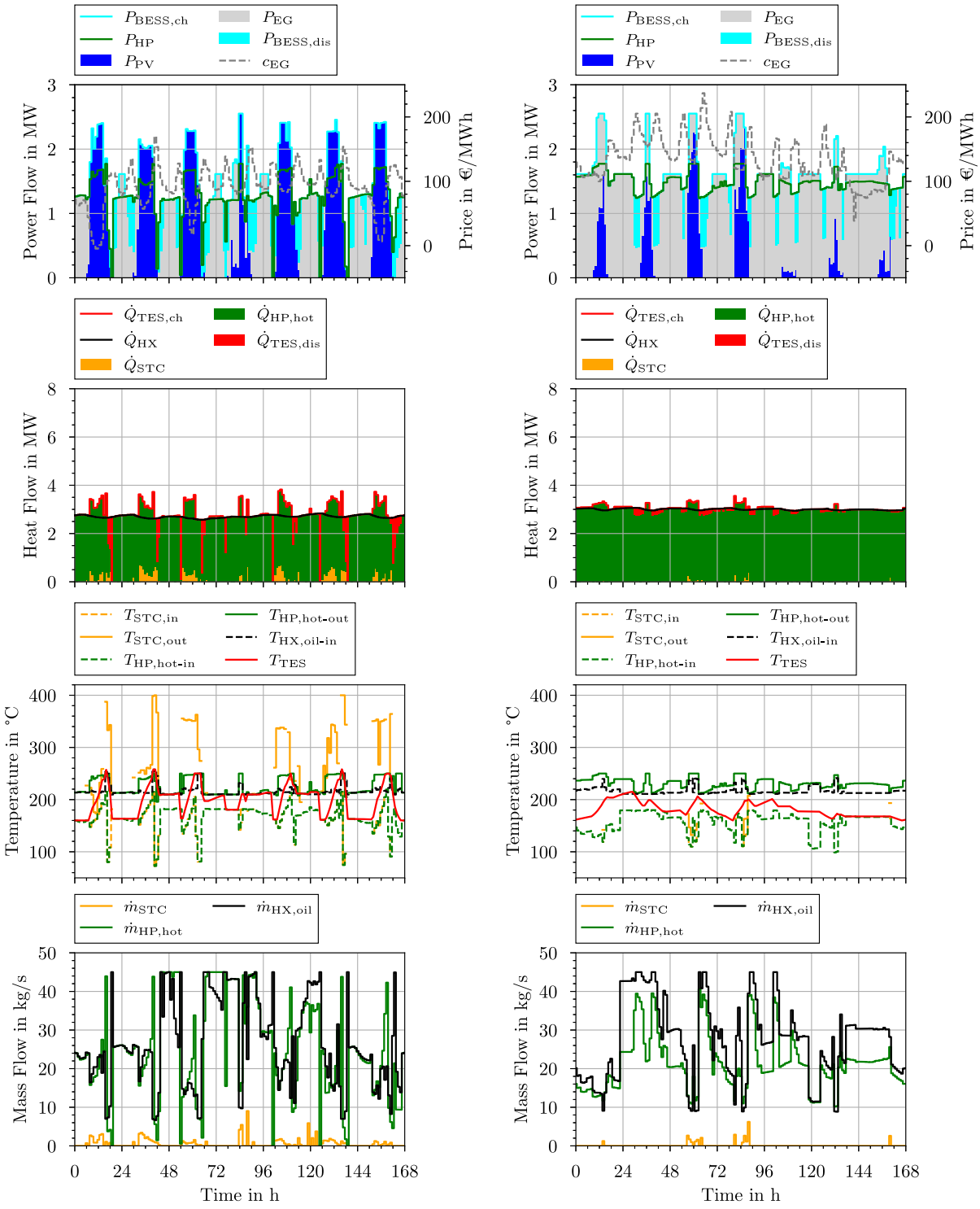

Fig. D.15. Optimal operating strategy of SHS configuration (b) with PTC and HP in parallel and TES in parallel with an optimal design point at TAC of 2.48 Mio. €/a at site Würzburg for a typical summer week (left) and a typical winter week (right).

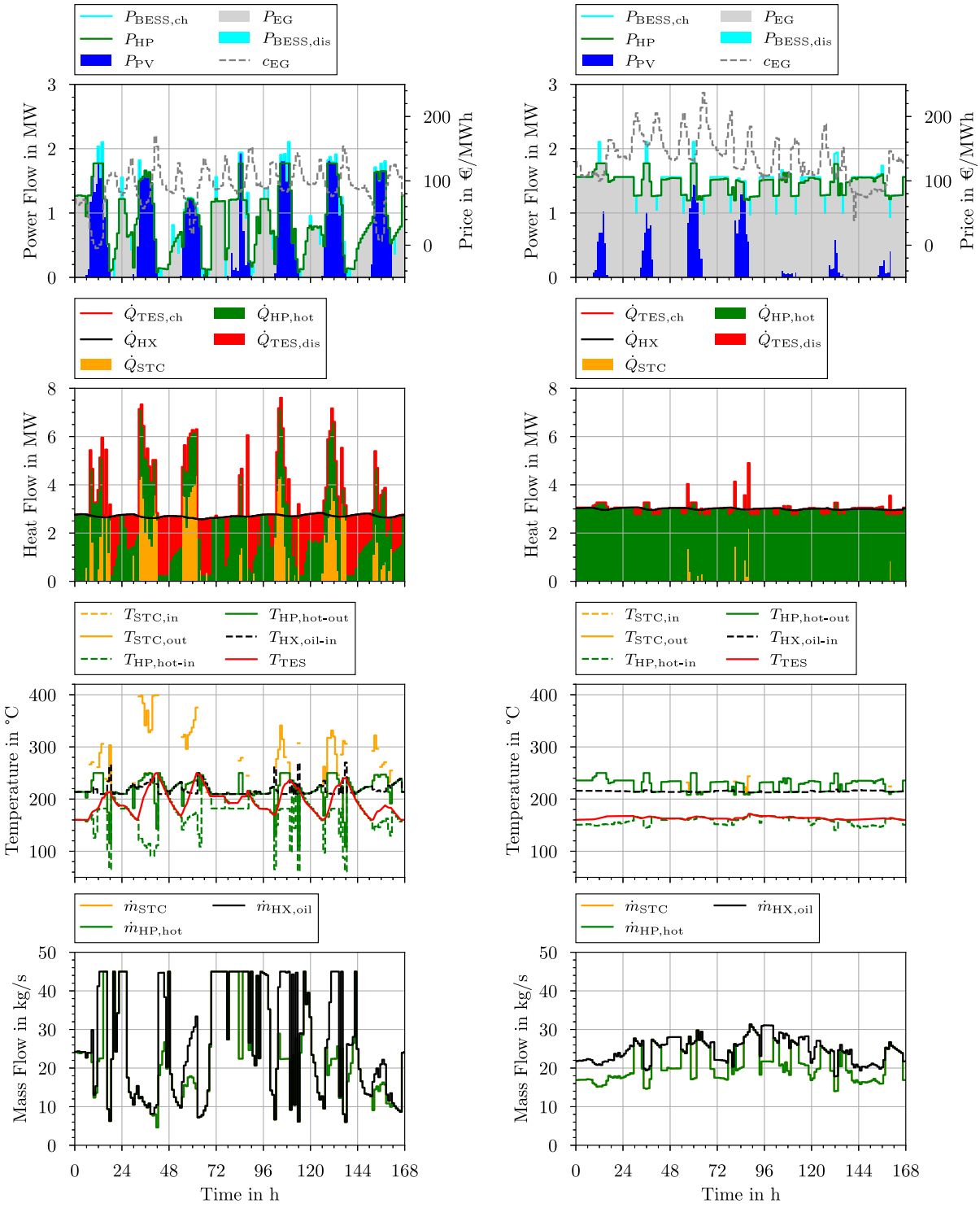

Fig. D.16. Optimal operating strategy of SHS configuration (c) with PTC and HP in series and TES in series with an optimal design point at TAC of 2.48 Mio. €/a at site Würzburg for a typical summer week (left) and a typical winter week (right).

Data availability

Data will be made available on request.

References

[1] 2050 long-term strategy - European commission - climate action. 2025, URL https://climate.ec.europa.eu/eu-action/climate-strategies-targets/2050-long-term-strategy_en. [Accessed 04 February 2025].

[2] International Energy Agency (IEA). Renewables 2023 - analysis and forecast to 2028. 2024, URL https://iea.blob.core.windows.net/assets/96d66a8b-d502-476b-ba94-54ffda84cf72/Renewables_2023.pdf.

[3] Bube S, Voß S, Bullerdiek N, Kaltschmitt M. Power-to-chemicals: Defossilization of the chemical industry via PtX. In: Powerfuels: status and prospects. Cham: Springer Nature Switzerland; 2025, p. 941–74. http://dx.doi.org/10.1007/978-3-031-62411-7_32.

[4] IN4climateNRW. Prozesswärme für eine klimaneutrale industrie - impulspapier der initiative IN4climate.nrw. 2022, Düsseldorf.

[5] Von Thadden Del Valle C, Frey G, Van Beek M, Budt M. Technologies for defossilisation of process heat. In: 37th international conference on efficiency,

cost, optimization, simulation and environmental impact of energy systems (ECOS 2024). 2024, http://dx.doi.org/10.52202/077185-0027.
[6] Lu Z, Yao Y, Liu G, Ma W, Gong Y. Thermodynamic and economic analysis of a high temperature cascade heat pump system for steam generation. Processes 2022;10(9). http://dx.doi.org/10.3390/pr10091862, URL https://www.mdpi.com/2227-9717/10/9/1862.
[7] Paya J, Cazorla-Marin A, Arpagaus C, Corrales Ciganda JL, Hassan AH. Low-pressure steam generation with concentrating solar energy and different heat upgrade technologies: Potential in the European industry. Sustainability 2024;16(5). http://dx.doi.org/10.3390/su16051733, URL https://www.mdpi.com/2071-1050/16/5/1733.
[8] Wolf M, Pröll T. A comparative study of sustainable industrial heat supply based on economic and thermodynamic factors. Die Bodenkult: J Land Manag Food Environ 2017;68(3):145–56. http://dx.doi.org/10.1515/boku-2017-0013.
[9] Magni C, Peeters R, Quoilin S, Arteconi A. Assessing the Flexibility Potential of Industrial Heat–Electricity Sector Coupling through High-Temperature Heat Pumps: The Case Study of Belgium. Energies 2024;17(2):541. http://dx.doi.org/10.3390/en17020541.
[10] Bever P-M, Bless F, Arpagaus C, Bertsch SS. High-temperature heat pumps for industrial use. Chem Ing Tech 2024;96(8):1071–84. http://dx.doi.org/10.1002/cite.202300241, URL https://onlinelibrary.wiley.com/doi/abs/10.1002/cite.202300241 arXiv:https://onlinelibrary.wiley.com/doi/pdf/10.1002/cite.202300241.
[11] Ciambellotti A, Frate GF, Baccioli A, Desideri U. High-temperature heat pumps for electrification and cost-effective decarbonization in the tissue paper industry. Energies 2024;17(17). http://dx.doi.org/10.3390/en17174335, URL https://www.mdpi.com/1996-1073/17/17/4335.
[12] Kumar L, Ahmed J, El Haj Assad M, Hasanuzzaman M. Prospects and challenges of solar thermal for process heating: A comprehensive review. Energies 2022;15(22). http://dx.doi.org/10.3390/en15228501, URL https://www.mdpi.com/1996-1073/15/22/8501.
[13] Häberle A, Krüger D. Chapter 18 - concentrating solar technologies for industrial process heat. In: Lovegrove K, Stein W, editors. Concentrating solar power technology (second edition). Woodhead publishing series in energy, second ed.. Woodhead Publishing; 2021, p. 659–75. http://dx.doi.org/10.1016/B978-0-12-819970-1.00011-6, URL https://www.sciencedirect.com/science/article/pii/B9780128199701000116.
[14] 'Gus' Nathan G, Lee L, Ingenhoven P, Tian Z, Sun Z, Chinnici A, Jafarian M, Ashman P, Potter D, Saw W. Pathways to the use of concentrated solar heat for high temperature industrial processes. Sol Compass 2023;5:100036. http://dx.doi.org/10.1016/j.solcom.2023.100036, URL https://www.sciencedirect.com/science/article/pii/S2772940023000048.
[15] Ahmed J, Kumar L, Abbasi AF, El Haj Assad M. Energy, exergy, environmental and economic analysis (4e) of a solar thermal system for process heating in jamshoro, Pakistan. Energies 2022;15(22). http://dx.doi.org/10.3390/en15228617, URL https://www.mdpi.com/1996-1073/15/22/8617.
[16] Rozon F, Koke J, McGregor C, Owen M. Techno-economic analyses of solar thermal process heat integration at South African beverage producers. Sol Compass 2023;8:100063. http://dx.doi.org/10.1016/j.solcom.2023.100063, URL https://www.sciencedirect.com/science/article/pii/S2772940023000310.
[17] Krüger DR, Fischer S, Nitz P, Inigo Labairu J. Chancen für den einsatz konzentrierender kollektoren in mitteleuropa. In: 31. symposium solarthermie und innovative wärmesysteme 2021. 2021, p. 1–14, URL https://elib.dlr.de/145751/.
[18] Ravi Kumar K, Krishna Chaitanya N, Sendhil Kumar N. Solar thermal energy technologies and its applications for process heating and power generation – a review. J Clean Prod 2021;282:125296. http://dx.doi.org/10.1016/j.jclepro.2020.125296, URL https://www.sciencedirect.com/science/article/pii/S0959652620353415.
[19] Saini P, Ghasemi M, Arpagaus C, Bless F, Bertsch S, Zhang X. Techno-economic comparative analysis of solar thermal collectors and high-temperature heat pumps for industrial steam generation. Energy Convers Manage 2023;277:116623. http://dx.doi.org/10.1016/j.enconman.2022.116623, URL https://www.sciencedirect.com/science/article/pii/S0196890422014017.
[20] Lazzarin R. Heat pumps and solar energy: A review with some insights in the future. Int J Refrig 2020;116:146–60. http://dx.doi.org/10.1016/j.ijrefrig.2020.03.031, URL https://www.sciencedirect.com/science/article/pii/S0140700720301468.
[21] Perrella S, Bisegna F, Bevilacqua P, Cirone D, Bruno R. Solar-assisted heat pump with electric and thermal storage: The role of appropriate control strategies for the exploitation of the solar source. Buildings 2024;14(1). http://dx.doi.org/10.3390/buildings14010296.
[22] Díaz-de León C, Baltazar J-C, Martínez-Rodríguez G. Assessment of a heat pump assisted with solar thermal energy for an Industrial batch process. Chem Eng Trans 2022;94:319–24. http://dx.doi.org/10.3303/CET2294053, URL https://www.cetjournal.it/index.php/cet/article/view/CET2294053.
[23] Martínez-Rodríguez G, Baltazar J-C, Fuentes-Silva AL. Heat and electric power production using heat pumps assisted with solar thermal energy for industrial applications. Energy 2023;282:128379. http://dx.doi.org/10.1016/j.energy.2023.128379, URL https://www.sciencedirect.com/science/article/pii/S0360544223017735.
[24] Lee G-R, Lim B-J, Cho S-H, Farooq M, Tanaka H, Park C-D. Performance and economic analysis of solar-heat pump system for process steam supply in industrial sector. Energy Convers Manage 2025;328:119596. http://dx.doi.org/10.1016/j.enconman.2025.119596, URL https://www.sciencedirect.com/science/article/pii/S0196890425001190.
[25] Grubbauer A, Fluch J, Brunner C, Ramschak T, Wilk V, Fleckl T. Renewable and highly efficient energy systems through innovative combination of solar thermal and heat pump systems. Chem Eng Trans 2018;70:745–50. http://dx.doi.org/10.3303/CET1870125, URL https://www.cetjournal.it/index.php/cet/article/view/CET1870125.
[26] Jesper M, Pag F, Vajen K, Jordan U. Hybrid solar thermal and heat pump systems in industry: Model based development of globally applicable design guidelines. Sol Energy Adv 2023;3:100034. http://dx.doi.org/10.1016/j.seja.2023.100034, URL https://www.sciencedirect.com/science/article/pii/S2667113123000025.
[27] Rosales-Pérez JF, Villarruel-Jaramillo A, Romero-Ramos JA, Pérez-García M, Cardemil JM, Escobar R. Hybrid system of photovoltaic and solar thermal technologies for industrial process heat. Energies 2023;16(5). http://dx.doi.org/10.3390/en16052220, URL https://www.mdpi.com/1996-1073/16/5/2220.
[28] O'Leary E. Energy Audit Summary Report CIT Audit no. 59 – IRL03. Tech. rep., energyXperts.NET, Cork Institute of Technology; 2024.
[29] Hirsch T, Dersch J, Fluri T, García-Barberena J, Giuliano S, Hustig-Diethelm F, Meyer R, Schmidt N, Seitz M, Yildiz E. Guideline for Bankable STE Yield Assessment. Tech. rep., SolarPACES; 2017, URL https://www.solarpaces.org/guideline-for-bankable-ste-yield-assessment/.
[30] Chemical Engineering. Chemical engineering plant cost index. 2024, URL https://www.chemengonline.com/site/plant-cost-index/. [Accessed 22 September 2024].
[31] Liu P, Pistikopoulos EN, Li Z. An energy systems engineering approach to the optimal design of energy systems in commercial buildings. Energy Policy 2010;38(8):4224–31. http://dx.doi.org/10.1016/j.enpol.2010.03.051.
[32] Maroufmashat A, Sattari S, Roshandel R, Fowler M, Elkamel A. Multi-objective optimization for design and operation of distributed energy systems through the multi-energy hub network approach. Ind Eng Chem Res 2016;55(33):8950–66. http://dx.doi.org/10.1021/acs.iecr.6b01264.
[33] Gabrielli P, Gazzani M, Martelli E, Mazzotti M. Optimal design of multi-energy systems with seasonal storage. Appl Energy 2018;219:408–24. http://dx.doi.org/10.1016/j.apenergy.2017.07.142.
[34] Philipps S, Warmuth W. Photovoltaics Report. Tech. rep., Fraunhofer ISE; 2024, URL https://www.ise.fraunhofer.de/de/veroeffentlichungen/studien/photovoltaics-report.html.
[35] Kaewnukultorn T, Sepúlveda-Mora SB, Hegedus S. The impacts of DC/AC ratio, battery dispatch, and degradation on financial evaluation of bifacial pv+bess systems. Renew Energy 2024;121402. http://dx.doi.org/10.1016/j.renene.2024.121402, URL https://www.sciencedirect.com/science/article/pii/S0960148124014708.
[36] DLR Solar Research. Greenius manual. 2024, URL https://www.dlr.de/de/sf/forschung-und-transfer/forschungsdienstleistungen/simulation-und-wirtschaftlichkeitsbewertung/copy_of_greenius/greenius-support. [Accessed 11 November 2024].
[37] King DL, Gonzalez S, Galbraith GM, Boyson WE. Performance Model for Grid-Connected Photovoltaic Inverters. Tech. Rep. SAND2007-5036, Sandia National Laboratories; 2007, URL https://energy.sandia.gov/wp-content/gallery/uploads/Performance-Model-for-Grid-Connected-Photovoltaic-Inverters.pdf.
[38] Mongird K, Viswanathan V, Alam J, Vartanian C, Sprenkle V. 2020 Grid Energy Storage Technology Cost and Performance Assessment. Tech. Rep. DOE/PA-0204, U.S. Department of Energy; 2020, URL https://www.energy.gov/energy-storage-grand-challenge/articles/2020-grid-energy-storage-technology-cost-and-performance.
[39] Solar Keymark Database. Solar keymark certificate annex for DIMAS SA energy+evo. 2024, URL https://www.duurzaamloket.nl/DBF/PDF_Downloads/DS_305.pdf. [Accessed 20 September 2024].
[40] SCHOTT Solar CSP. SCHOTT PTR 70 brochure. 2024, URL https://pdf.directindustry.com/pdf/schott-glas/schott-ptr70-brochure/22716-557455-_3.html. [Accessed 20 September 2024].
[41] Oehler J, Gollasch J, Tran AP, Nicke E. Part Load Capability of a High Temperature Heat Pump with Reversed Brayton Cycle. In: International Energy Agency, editor. 13th IEA heat pump conference. 2021, p. 1806–17.
[42] Walden JV, Bähr M, Glade A, Gollasch J, Tran AP, Lorenz T. Nonlinear operational optimization of an industrial power-to-heat system with a high temperature heat pump, a thermal energy storage and wind energy. Appl Energy 2023;344:121247. http://dx.doi.org/10.1016/j.apenergy.2023.121247.
[43] Schlosser F, Jesper M, Vogelsang J, Walmsley T, Arpagaus C, Hesselbach J. Large-scale heat pumps: Applications, performance, economic feasibility and industrial integration. Renew Sustain Energy Rev 2020;133:110219. http://dx.doi.org/10.1016/j.rser.2020.110219, URL https://www.sciencedirect.com/science/article/pii/S1364032120305086.
[44] Ding Y. In: Thermal energy storage: Materials, devices, systems and applications, vol. 29, Royal Society of Chemistry; 2021.
[45] ENERGYNEST. Die energynest ThermalBattery™. 2024, URL https://energy-nest.com/de/thermal-battery/. [Accessed 20 September 2024].

[46] Bergman T, DeWitt D, Incropera F, Lavine A. In: Fundamentals of Heat and Mass Transfer, vol. 997, John Wiley & Sons; 2011, p. 722–7.

[47] PVGISCOM. Photovoltaic geographical information system. 2024, URL https://pvgis.com/. [Accessed 23 September 2024].

[48] Energiewende A. Agorameter modellversion 3.0. 2023, URL https://www.agora-energiewende.de/daten-tools/agorameter/. [Accessed 23 September 2024].

[49] Mavrotas G. Effective implementation of the epsilon-constraint method in multi-objective mathematical programming problems. Appl Math Comput 2009;213(2):455–65. http://dx.doi.org/10.1016/j.amc.2009.03.037, URL https://www.sciencedirect.com/science/article/pii/S0096300309002574.

[50] Hernández-Romero IM, Nápoles-Rivera F, Flores-Tlacuahuac A, Fuentes-Cortés LF. Optimal design of the ocean thermal energy conversion systems involving weather and energy demand variations. Chem Eng Process - Process Intensif 2020;157:108114. http://dx.doi.org/10.1016/j.cep.2020.108114.

[51] Guo L, Liu W, Cai J, Hong B, Wang C. A two-stage optimal planning and design method for combined cooling, heat and power microgrid system. Energy Convers Manage 2013;74:433–45. http://dx.doi.org/10.1016/j.enconman.2013.06.051.

[52] Evins R. Multi-level optimization of building design, energy system sizing and operation. Energy 2015;90:1775–89. http://dx.doi.org/10.1016/j.energy.2015.07.007.

[53] Zhang J, Li K-J, Wang M, Lee W-J, Gao H. A bi-level program for the planning of an islanded microgrid including CAES. In: 2015 IEEE industry applications society annual meeting. 2015, p. 1–8. http://dx.doi.org/10.1109/IAS.2015.7356783.

[54] Schmeling L, Schönfeldt P, Klement P, Vorspel L, Hanke B, von Maydell K, Agert C. A generalised optimal design methodology for distributed energy systems. Renew Energy 2022;200:1223–39. http://dx.doi.org/10.1016/j.renene.2022.10.029.

[55] Deb K, Pratap A, Agarwal S, Meyarivan T. A fast and elitist multiobjective genetic algorithm: NSGA-II. IEEE Trans Evol Comput 2002;6(2):182–97. http://dx.doi.org/10.1109/4235.996017.

[56] Wang R, Xiong J, fan He M, Gao L, Wang L. Multi-objective optimal design of hybrid renewable energy system under multiple scenarios. Renew Energy 2020;151:226–37. http://dx.doi.org/10.1016/j.renene.2019.11.015, URL https://www.sciencedirect.com/science/article/pii/S0960148119316969.

[57] Zhu X, Gui P, Zhang X, Han Z, Li Y. Multi-objective optimization of a hybrid energy system integrated with solar-wind-PEMFC and energy storage. J Energy Storage 2023;72:108562. http://dx.doi.org/10.1016/j.est.2023.108562, URL https://www.sciencedirect.com/science/article/pii/S2352152X2301959X.

[58] Cheraghi R, Hossein Jahangir M. Multi-objective optimization of a hybrid renewable energy system supplying a residential building using NSGA-II and MOPSO algorithms. Energy Convers Manage 2023;294:117515. http://dx.doi.org/10.1016/j.enconman.2023.117515, URL https://www.sciencedirect.com/science/article/pii/S0196890423008610.

[59] Mukoni E, Garner KS. Multi-objective non-dominated sorting genetic algorithm optimization for optimal hybrid (wind and grid)-hydrogen energy system modelling. Energies 2022;15(19). http://dx.doi.org/10.3390/en15197079, URL https://www.mdpi.com/1996-1073/15/19/7079.

[60] Wächter A, Biegler LT. On the implementation of an interior-point filter line-search algorithm for large-scale nonlinear programming. Math Program 2006;106:25–57. http://dx.doi.org/10.1007/s10107-004-0559-y.

[61] Hoffmann M, Kotzur L, Stolten D, Robinius M. A review on time series aggregation methods for energy system models. Energies 2020;13(3). http://dx.doi.org/10.3390/en13030641, URL https://www.mdpi.com/1996-1073/13/3/641.

[62] Peri D, Tinti F. A multistart gradient-based algorithm with surrogate model for global optimization. Commun Appl Ind Math 2012;3. URL https://api.semanticscholar.org/CorpusID:55575316.

[63] Ugray Z, Lasdon L, Plummer J, Glover F, Kelly J, Marti R. Scatter Search and Local Nlp Solvers: A Multistart Framework for Global Optimization. INFORMS J Comput 2006. http://dx.doi.org/10.2139/ssrn.886559, http://leeds-faculty.colorado.edu/glover/article-SSMultistart-ugraylasdon.pdf.

[64] György A, Levente K. Efficient Multi-Start Strategies for Local Search Algorithms. J Artificial Intelligence Res 2009. http://dx.doi.org/10.1613/jair.3313, URL https://jair.org/index.php/jair/article/download/10716/25604.

[65] Kotzur L, Markewitz P, Robinius M, Stolten D. Impact of different time series aggregation methods on optimal energy system design. Renew Energy 2018;117:474–87. http://dx.doi.org/10.1016/j.renene.2017.10.017, URL https://www.sciencedirect.com/science/article/pii/S0960148117309783.

[66] Blank J, Deb K. Pymoo: Multi-objective optimization in python. IEEE Access 2020;8:89497–509.

[67] Hart WE, Watson J-P, Woodruff DL. Pyomo: modeling and solving mathematical programs in python. Math Program Comput 2011;3(3):219–60.

[68] CanadianSolar. HiKu5 mono technical information sheet. 2022, URL https://cdn.enfsolar.com/z/pp/acc60dbda3e4ed35/5fe2bced1c3d5.pdf. [Accessed 21 September 2024].

[69] IRENA. Renewable power generation costs in 2022. 2023, URL https://www.irena.org/-/media/Files/IRENA/Agency/Publication/2023/Aug/IRENA_Renewable_power_generation_costs_in_2022.pdf.

[70] NREL. Electricity annual technology baseline. 2023, URL https://atb.nrel.gov/electricity/2023/data. [Accessed 22 September 2024].

[71] Jacobson MZ, Jadhav V. World estimates of PV optimal tilt angles and ratios of sunlight incident upon tilted and tracked PV panels relative to horizontal panels. Sol Energy 2018;169:55–66. http://dx.doi.org/10.1016/j.solener.2018.04.030, URL https://www.sciencedirect.com/science/article/pii/S0038092X1830375X.

[72] Loutzenhiser P, Manz H, Felsmann C, Strachan P, Frank T, Maxwell G. Empirical validation of models to compute solar irradiance on inclined surfaces for building energy simulation. Sol Energy 2007;81(2):254–67. http://dx.doi.org/10.1016/j.solener.2006.03.009, URL https://www.sciencedirect.com/science/article/pii/S0038092X06000879.

[73] Ramasamy V, Zuboy J, O'Shaughnessy E, Feldman D, Desai J, Woodhouse M, Basore P, Margolis R. U.S. Solar Photovoltaic System and Energy Storage Cost Benchmarks, With Minimum Sustainable Price Analysis: Q1 2022. Tech. rep., National Renewable Energy Laboratory; 2022, URL https://www.ise.fraunhofer.de/de/veroeffentlichungen/studien/photovoltaics-report.html.

[74] ISO/FDIS9806:2017(E). Solar energy — Solar thermal collectors — Test methods. 2017.

[75] Arpagaus C, Bless F, Uhlmann M, Schiffmann J, Bertsch SS. High temperature heat pumps: Market overview, state of the art, research status, refrigerants, and application potentials. Energy 2018;152:985–1010.

[76] Schlosser F. Integration von Wärmepumpen zur Dekarbonisierung der industriellen Wärmeversorgung. kassel University Press; 2021, http://dx.doi.org/10.17170/kobra-202103023389.

[77] Walden JV, Wellig B, Stathopoulos P. Heat pump integration in non-continuous industrial processes by dynamic pinch analysis targeting. Appl Energy 2023;352:121933. http://dx.doi.org/10.1016/j.apenergy.2023.121933, URL https://www.sciencedirect.com/science/article/pii/S0306261923012977.

[78] Hoivik N, Greiner C, Barragan J, Iniesta AC, Skeie G, al Bergan P, Blanco-Rodriguez P, Calvet N. Long-term performance results of concrete-based modular thermal energy storage system. J Energy Storage 2019;24:100735. http://dx.doi.org/10.1016/j.est.2019.04.009, URL https://www.sciencedirect.com/science/article/pii/S2352152X18306480.

[79] RECHARGE. Why a low-cost thermal battery could become the swiss army knife of emission reductions. 2020, URL https://www.rechargenews.com/transition/why-a-low-cost-thermal-battery-could-become-the-swiss-army-knife-of-emissions-reductions/2-1-853168. [Accessed 22 September 2024].

[80] ENGINEERINGpage. TYPICAL overall HEAT TRANSFER coefficients (u - VALUES). 2024, URL http://www.engineeringpage.com/technology/thermal/transfer.html. [Accessed 22 September 2024].

[81] Taal M, Bulatov I, Klemes J, Stehlik P. Cost estimation and energy price forecasts for economic evaluation of retrofit projects. Appl Therm Eng 2003;23(14):1819–35. http://dx.doi.org/10.1016/S1359-4311(03)00136-4, Process Integration, Modelling and Optimisation for Energy Saving and Pollution Reduction. URL https://www.sciencedirect.com/science/article/pii/S1359431103001364.

[82] Spang B, Roetzel W. C6 costs and economy of heat exchangers. In: VDI heat atlas. Berlin, Heidelberg: Springer Berlin Heidelberg; 2010, p. 115–8. http://dx.doi.org/10.1007/978-3-540-77877-6_9.

[83] Albrecht FG, König DH, Baucks N, Dietrich R-U. A standardized methodology for the techno-economic evaluation of alternative fuels – a case study. Fuel – Sci Technol Fuel Energy 2017;194:511–26, URL https://elib.dlr.de/109190/.

[84] Applied heat thermomat oil heaters. 2025, URL https://appliedheat.co.za/products/thermomat-vo-direct-edible-oil-heaters/. [Accessed 04 february 2025].

[85] Natural gas prices for non-households in Germany. 2025, URL https://www-genesis.destatis.de. [Accessed 04 February 2025].

[86] CO2 cost allocation: heating value vs. calorific value. 2025, URL https://www.brunata-metrona.de/infocenter/newsroom/aktuelle-meldungen/co2-kostenaufteilung-heizwert-vs-brennwert/. [Accessed 04 February 2025].

[87] Dow Chemical Company. Dowterm^{TM}a technical data sheet. 2024, URL https://www.dow.com/en-us/document-viewer.html?randomVar=1368364724352739056&docPath=/content/dam/dcc/documents/176/176-01463-01-dowtherm-a-tds.pdf. [Accessed 20 September 2024].

[88] The Engineering ToolBox. Dry air - thermodynamic and physical properties. 2005, URL https://www.engineeringtoolbox.com/dry-air-properties-d_973.html. [Accessed 20 September 2024-09-20].

[89] Duesseldorf N. Netzentgelte strom und weitere entgeltbestandteile. 2023, URL https://www.netz-duesseldorf.de/media/mam-upload/2023-12-20–preisblatt-nne-strom-2024.pdf. [Accessed 21 September 2024].

[90] Quiñones G, Felbol C, Valenzuela C, Cardemil JM, Escobar RA. Analyzing the potential for solar thermal energy utilization in the Chilean copper mining industry. Sol Energy 2020;197:292–310. http://dx.doi.org/10.1016/j.solener.2020.01.009, URL https://www.sciencedirect.com/science/article/pii/S0038092X20300116.

[91] Dersch J, Dieckmann S, Hennecke K, Pitz-Paal R, Taylor M, Ralon P. LCOE reduction potential of parabolic trough and solar tower technology in G20 countries until 2030. AIP Conf Proc 2020;2303(1):120002. http://dx.doi.org/10.1063/5.0028883.

[92] Iñigo-Labairu J, Dersch J, Schomaker L. Integration of CSP and PV power plants: Investigations about synergies by close coupling. Energies 2022;15(19). http://dx.doi.org/10.3390/en15197103, URL https://www.mdpi.com/1996-1073/15/19/7103.

[93] Hoivik N, Greiner C, Tirado EB, Barragan J, Bergan Pa, Skeie G, Blanco P, Calvet N. Demonstration of EnergyNest thermal energy storage (TES) technology. AIP Conf Proc 2017;1850(1):080011. http://dx.doi.org/10.1063/1.4984432.